Holographic Storage Dynamics, Phase Conjugation, and Nonlinear Optics in Photorefractive Materials

Thesis by

Sergei S. Orlov

In Partial Fulfillment of the Requirements

for the Degree of

Doctor of Philosophy

California Institute of Technology

Pasadena, California

1996

(Submitted May 23, 1996)

To my parents and brother

Acknowledgments

First, I would like to thank my thesis advisor, Prof. Amnon Yariv, for the guidance and support he has given me over the years of my work in his group. It is both a remarkable experience and a privilege to work in his Laboratory.

I also would like to thank Prof. Demetri Psaltis for giving me a wonderful opportunity to work in his group in my first graduate year here at Caltech. Special thanks also go to Prof. Mordechai Segev for his most enthusiastic support and encouragement. Thanks are also extended to the researchers I had a pleasure to collaborate with, including Doruk Engin, Drs. George Rakuljic, Ratnakar Neurgaonkar, George Valley, Yong Qiao, and Victor Leyva. Helpful discussions with Prof. Bruno Crosignani, Prof. Aharon Agranat, Prof. George Rossman, Dr. Marvin Klein, Dr. David Pepper, Dr. John Hong, and Dr. Mark Garrett are also gratefully acknowledged.

I wish to thank all the remarkable individuals with whom I had a pleasure to interact and work with, including Gilad Almogy, Kevin Cooper, Danny Eliyahu, Jing Feng, Ali Ghaffari, Rudolf Hoffmeister, John Ianelli, Anthony Kewitsch, John Kitching, Roger Koumans, Reginald Lee, William Marshall, Matthew McAdams, Jana Mercado, John O'Brien, Volnei Pedroni, Dan Provenzano, Joseph Rosen, Akira Saito, Boaz Salik, Ali Shakouri, Xiao-lin Tong, Yuanjian Xu, Min Zhang, George Barbastathis, Geoffrey Burr, Jean-Jacques Drolet, Michael Levene, Roopa Ramamoorthi, and Kirill Shcheglov. Over the past few years some of them also became my friends.

Finally, I would like to acknowledge the researchers with whom I started my work in the field of photorefractive nonlinear optics, including Drs. Nikolai Bogodaev, Ljudmila Ivleva, Nikolai Polozkov, and Yuri S. Kuzminov of General Physics Institute and Dr. Alexei Zozulya of Lebedev Physical Institute of Russian Academy of Sciences.

First and foremost I would like to thank my brother Vladimir and my parents, Irina and Stanislav Orlov, for their support, care, and encouragement.

Abstract

This thesis explores the application of photorefractive materials in two distinct areas: the holographic data storage and the dynamic nonlinear optical interactions. First, we have established that partial ferroelectric domain reversal in certain ferroelectric materials can be used to permanently fix the dynamic holographic gratings, and analyzed the interaction between the fixed and the dynamic components of a hologram. A comprehensive analysis of the storage temporal dynamics in photorefractive materials is further developed for the case of thermal ionic fixing. An experimental study of holographic storage dynamics in photorefractive lithium niobate revealed new features related to the ionic conductivity in this and similar materials. We established and developed techniques for long-lifetime and high-efficiency hologram fixing in the holographic data storage applications. We further analyze theoretically the impact of the recording response properties of different storage media (including photorefractive materials and photopolymers) and optical detection noise on the ultimate storage capacity of holographic memories.

Second, the transverse properties of the photorefractive double phase conjugate mirror (DPCM) have been studied. We have established that the DPCM exhibits a sharp conjugation fidelity gain threshold which increases with image resolution, while the reflectivity is a smoothly varying function of nonlinear gain. The conjugation fidelity was found to degrade dramatically for unequal intensities ratio. The DPCM exhibits critical slowing down in the vicinity of the oscillation threshold. A two-dimensional coupled-

modes perturbation analysis of the DPCM is introduced and its basic predictions are in a good qualitative agreement with the results of the experimental study.

Finally, we analyze the nonlinear optical second harmonic generation in materials with strong photorefractivity. In the presence of strong self-phase modulation the phase matching conditions are modified and we found that in some cases this leads to a unique effect, namely, the nonlinear self-phase matching of optical nonlinear interaction. Strong photorefractive response manifests itself in two characteristic and very apparent manners; a large change in the conversion efficiency and self-defocusing of the generated second harmonic beam. We introduced a two-dimensional model of photorefractive effect and found its predictions to be in a good qualitative agreement with the observed transverse dynamics.

Table of Contents

Chapter One

Introduction to Photorefractive Nonlinear Optics and Applications

1.1 Introduction

Photorefractive effect is defined as a nonlinear change of the index of refraction of the medium in the presence of light. Most photorefractive materials are electrooptic crystals in which refractive indices are changed by photoinduced space charge fields via the electrooptic effect. The possibility of obtaining high optical nonlinearities at milliwatt power levels makes these materials particularly attractive for applications in dynamic holography, phase conjugation, and holographic data storage.

The photorefractive effect has been discovered in a large variety of electrooptic materials including $LiNbO_3$ [1, 2], $LiTaO_3$, $BaTiO_3$ [3], $KNbO_3$ [4], $Ba_{1-x}Sr_xNb_2O_6$ [5], $Bi_{12}SiO_{20}$ and $Bi_{12}GeO_{20}$ [6], GaAs, InP [7] and other compound semiconductors, and, therefore, can be considered as a general property of electrooptic materials. Depending on the band gap of the material and the energy levels of the donor and acceptor levels of the

impurity ions involved, the photorefractive effect may be induced by ultraviolet, visible or infrared radiation.

Since the discovery of the photorefractive effect, a great deal of effort has been devoted to identifying the microscopic details of the mechanism in order to optimize materials for either memory or nonlinear optical applications [8]. These studies have also led to the discovery of new effects in photorefractive materials, including the bulk photovoltaic effect [9] and holographic light-induced scattering ("beam fanning") [10]. At present, it is understood that the photorefractive nonlinearity is produced due to the photoexcitation of mobile carriers from donor impurities, their diffusion and drift due to internal and externally applied electric field and photovoltaic current, subsequent retrapping of carriers on ionized donors, and, finally, the buildup of internal space charge field. The index perturbation is then produced by linear or biased quadratic electrooptic effects. A comprehensive model of photorefraction in electrooptic crystals was first proposed by Kukhtarev [11] and, later, expanded to incorporate both hole and electron conductivity [12], shallow traps [13], polarization variations [14], and ionic transport [15].

The possibility of using photorefractive materials as a storage media in holographic memory systems was first proposed by Chen et al. [2]. The holographic data storage uses the concept of storing data in the form of multiplexed holographic gratings distributed throughout the volume of the recording media [16, 17] and recorded with different references. The independent retrieval of each of the stored pages of data is allowed due to the Bragg selectivity provided by the volumetric interaction [18]. The random access is based on the optical parameters, such as the wavelength of light, incidence angle of the reference, or its spatial distribution. The dynamic response makes photorefractive materials suitable for both read-write (because holograms are optically "erasable"), and read-only

storage (if the gratings are quasi-permanently fixed [19]). For certain applications this versatility makes these materials a more attractive media compared to, e.g., photopolymers (read-write access is not possible), Ge-doped glass (only UV response is realized), or photographic emulsion (wet development is necessary). Holographic approach to storing large volumes of information is attractive due to its highly parallel access to the data, short access time, and very large theoretical diffraction-limited storage capacity of $\sim V/\lambda^3$ bits in a volume V.

Attempts at exploiting this potential have been made in early 70-s [20, 21], however, the major progress has not been achieved until recently [22-25], been triggered both by the advances in the growth and preparation of photorefractive holographic materials and associated device technologies (e.g., liquid crystal spatial light modulators and detector arrays), and by the inventions of new multiplexing techniques [26, 27]. Still many issues associated with material properties, their understanding and control, are of great importance. These include the dynamic range, photosensitivity, as well as permanent fixing of holograms for nonvolatile storage, and also efficiency and storage dynamics of fixed holograms (i.e., the lifetime of holographic memory).

Chapters 3, 4, and 5 of this thesis are devoted to the material research for holographic data storage application with particular emphasis on the fixing of stored holograms and their temporal dynamics and stability. Two distinctly different approaches have been exploited. One (Chapter 3) uses the variation in spontaneous ferroelectric polarization correlated with the electric field of the hologram, the other involves ionic transport at elevated temperature to create an ionic pattern mimicking the initial trapped electrons' distribution. The first (electrical fixing) approach leads to relatively low fixing efficiencies, but can be used sequentially, and, therefore, largely defeats the erasure during the

recording of multiplexed holograms [28]. The other approach (Chapter 4) gives very high fixing/developing efficiency with long lifetime, although all holograms can be fixed only after the complete exposure. We established and developed techniques for long-lifetime and high-efficiency hologram fixing in lithium niobate (as long as 2 to 10-15 years of projected lifetime can be realized [29]).

Other applications of volume holograms (fixed or dynamic) in photorefractive crystals include holographic interconnects, optical associative memory, and optical neural networks [30-32]. The ability of semiconductor photorefractive crystals (e.g., GaAs, InP) to convert efficiently a vibrating speckled interference pattern into a high frequency ac electric signal (via photo-electro-motive force effect [33]) led recently to a development of all-optical detection system for ultrasonic waves in metals and similar materials [34, 35]. Strong optical nonlinearity of photorefractive crystals can also lead to self-trapping of optical beams in the volume of photorefractive crystal, which was observed recently [36].

Another unique application to photorefractive materials is the dynamic holography, which involves the interaction of an incident light beam with its own diffracted beam inside the recording medium [18]. This causes the continuous recording of new gratings which amplitudes are nonuniform throughout the thickness of the material. The phase shift between the interference pattern and the recorded grating leads to a dynamic energy redistribution between the two recording beams [37]. The refractive index change induced by the radiation gives rise to a phase and intensity redistribution of the interference field and this, in turn, is reflected in the spatial distribution of the refractive index changes. This determines the complicated dynamic nature of self-diffraction, including transient effects and the establishment of a self-consistent stationary state, yielding considerable differences

between dynamic gratings and the static gratings. The beam coupling effect via the dynamic hologram can be useful for coherent light amplification of weak light beams.

Optical phase conjugation of cw laser radiation can be realized via nonlinear four-wave mixing in photorefractive materials. In the simplest case which involves the wave mixing between a signal and two counterpropagating pumps, the phase conjugate replica is generated due to the continuous, real-time readout by one of the pumps of the grating recorded due to the interference between the other pump and the signal. This scheme is completely analogous to the one of classical holography, but here the recording and reconstruction take place simultaneously. If the interaction volume is placed in some kind of an optical cavity or resonator which provides the feedback of the conjugated signal back into the nonlinear medium (this can be also, e.g., the internal reflections off the faces of the crystal) a nonlinear oscillation can buildup. The first photorefractive oscillator [38, 39] involved a photorefractive $BaTiO_3$ crystal externally pumped with a pair of counterpropagating laser beams. This resulted in the buildup of the oscillation in the form of another pair of mutually conjugate beams in an external cavity. In the self-pumped phase conjugation both pump beams originate from a portion of the same input signal, and, therefore, no external beams are necessary. The phase conjugation with simultaneous amplification of weak input signal is impossible with such schemes, however. A large number of self-pumped and externally pumped photorefractive oscillators have been developed [38-44]. One of the most interesting interactions is the double phase conjugate mirror (DPCM) [44] in which two mutually incoherent input beams create phase conjugate replicas of each other. Its importance is due to the fact that this basic interaction is involved in building more sophisticated schemes of phase conjugation in photorefractive (e.g., total internal reflection mirror [41] which includes two interconnected DPCMs). The quality of phase conjugation by such devices was demonstrated by focusing complicated images into

the crystals and observing the faithfulness of reproduction when the image-bearing input and output beams passed through a phase aberrator.

One of the applications of phase conjugation is the restoration of distorted optical beams to their original state after a double pass through abberating medium [45-47]. Others involve, to mention a few, image processing (edge enhancement, feature extraction, subtraction) [48, 49], optical novelty filters [50], multimode-to-singlemode fiber couplers [51], phase conjugate interferometry [52], and phase locking of laser diode arrays [53]. The properties of the photorefractive oscillators related to transverse structure of the conjugated beams are of particular importance to understanding the regimes and basic limitations of such devices. Chapter 6 is devoted to studies of the transverse effects in the photorefractive nonlinear oscillators. We investigate how the quality (fidelity) of phase conjugation depends on the optical parameters of the beams (such as image resolution and intensities ratio) and the nonlinear holographic gain of the medium. The results of the experimental study are analyzed using a multiple plane wave two-dimensional model.

1.2 Outline of the Thesis

In Chapter 2 the band transport theory of the photorefractive mechanism is presented. This is used to derive the coupled-wave equations of two-wave mixing and four-wave mixing in photorefractive materials. The fundamental concepts of holographic data storage and holographic fixing are reviewed.

The hologram fixing using ferroelectric microdomain patterns is presented in Chapter 3. Fixing is achieved via applying a short electric field pulse after a short-term, low optical intensity recording of each hologram at room temperature. The dynamic screening of fixed polarization and ionic holograms is analyzed theoretically and confirmed experimentally.

Storage dynamics and hologram fixing via thermally assisted ionic transport is analyzed in Chapter 4. Holographic gratings which are based on charge redistribution inevitably decay due to ionic and electronic conduction. A comprehensive model for storage dynamics in photorefractive materials is presented and relevant decay rates and transient hologram field expressions are derived. Storage dynamics and ionic fixing are studied experimentally in Fe-doped lithium niobate. Substantial reduction of hydrogen ion impurity density is shown to increase the available storage lifetime dramatically (from 3 to 10÷15 years at room temperature). The residual ionic conductivity is due to the species other than hydrogen (most likely, due to lithium self-interstitials) and has activation energy of 1.4 eV.

Chapter 5 reviews the effect of finite material dynamic range and noise in optical detection on the ultimate storage capacity of holographic memory for media with different recording mechanisms. Photorefractive as well as photochemical materials are considered. For the bulk volumetric storage in photorefractives and photopolymers the dominant factor limiting the storage capacity is the dynamic range and detection noise. The origin of these limitation is shown to lie in the erasure during multiplexed recording for photorefractive media *without fixing* and dc-saturation for photochemical materials.

Photorefractive double phase conjugation is the topic of Chapter 6. The experimental study demonstrates that the conjugation fidelity exhibits a sharp threshold, while conjugate reflectivity remains a smoothly varying function of the nonlinear gain. Gain threshold value increases with increasing image resolution. The conjugation fidelity degrades dramatically for unbalanced process. A two-dimensional coupled-modes perturbation analysis of the DPCM is presented and its predictions are compared with the experiments.

Chapter 7 considers optical second harmonic generation in the materials with photorefractive response. In the presence of strong photorefractive nonlinearity the phase

matching conditions for the frequency conversion process are (locally) modified, and in some cases, this gives rise to a new effect, namely, the nonlinear self-phase matching (of initially non-phase matched interaction). The latter process is studied experimentally in photovoltaic lithium niobate. The nonlinear self-phase matching of optical second harmonic generation manifests itself in a large change in the conversion efficiency and a strong spatial self-phase modulation (self-defocusing) of generated second harmonic. A two-dimensional model of photorefractive/photovoltaic response has been developed. The transverse structure of the index perturbation in the material and the spatial structure of the second harmonic beam are simulated numerically.

References for Chapter One

[1] A. Ashkin, G. D. Boyd, J. M. Dziedzic, R. G. Smith, A. A. Ballmann, H. J. Levinstein, and K. Nassau, Appl. Phys. Lett. **9**, 72 (1966).

[2] F. S. Chen, J. T. LaMacchia, and D. B. Frazer, Appl. Phys. Lett. **13**, 223 (1968).

[3] R. L. Townsend and J. T. LaMacchia, J. Appl. Phys. **41**, 5188 (1970).

[4] P. Gunter, U. Fluckiger, J. P. Huignard, and F. Micheron, Ferroelectrics **13**, 297 (1976).

[5] J. B. Thaxter, Appl. Phys. Lett. **15**, 210 (1969).

[6] M. Peltier and F. Micheron, J. Appl. Phys. **48**, 3683 (1977).

[7] A. M. Glass, A. M. Johnson, D. H. Olson, W. Simpson, and A. A. Ballmann, Appl. Phys. Lett. **44**, 948 (1984).

[8] A. M. Glass, Opt. Eng. **17**, 470 (1978).

[9] A. M. Glass, D. von der Linde, and T. J. Negran, Appl. Phys. Lett. **25**, 233 (1974).

[10] V. V. Voronov, I. R. Dorosh, Yu. S. Kuzminov, and N. V. Tkachenko, Sov. J. Quantum Electron. **10**, 1346 (1980).

[11] N. V. Kukhtarev, Sov. Tech. Phys. Lett. **2**, 438 (1976).

[12] G. C. Valley, J. Appl. Phys. **59**, 3363 (1986).

[13] P. Tayebati and D. Mahgerefteh, J. Opt. Soc. Am. B **8**, 1053 (1991).

[14] S. S. Orlov, D. Psaltis, and R. R. Neurgaonkar, Appl. Phys. Lett. **63**, 2466 (1993).

[15] A. Yariv, S. S. Orlov, G. A. Rakuljic, and V. Leyva, Opt. Lett. **20**, 1334 (1995).

[16] E. N. Leith, A. Kozma, J. Upatneiks, J. Marks, and N. Massey, Appl. Opt. **5**, 1303 (1966).

[17] J. P. VanHeerden, Appl. Opt. **2**, 393 (1963).

[18] H. Kogelnik, Bell. Syst. Tech. J. **48**, 2909 (1969).

[19] see, for example, D. L. Staebler and J. J. Amodei, Ferroelectrics **3**, 107 (1972).

[20] E. G. Ramberg, RCA Review **33**, 5 (1972).

[21] L. d'Auria, J. P. Huignard, C. Slezak, and E. Spitz, Appl. Opt. **13**, 808 (1974).

[22] F. H. Mok, M. C. Tackitt, and H. M. Stoll, Opt. Lett. **16**, 605 (1992).

[23] J. F. Heanue, M. C. Bashaw, and L. Hesselink, Science **265**, 749 (1994).

[24] J. H. Hong, I. McMichael, T. Y. Chang, W. Christian, and E. G. Paek, Opt. Eng. **34**, 2193 (1995).

[25] D. Psaltis and F. Mok, Sci. Am. **273**, 70 (1995).

[26] G. A. Rakuljic, V. Leyva, and A. Yariv, Opt. Lett. **17**, 1471 (1992).

[27] D. Psaltis, M. Levene, A. Pu, G. Barbastathis, and K. Curtis, Opt. Lett. **20**, 782 (1995).

[28] J. Ma, T. Chang, J. Hong, R. R. Neurgaonkar, G. Barbastathis, and D. Psaltis, "Electrical fixing of 1000 angle-multiplexed holograms in SBN:75," to appear in IEEE'96 Nonlinear Optics, Fundamentals and Applications, Maui, Hawaii (1996).

[29] S. S. Orlov and A. Yariv, "Long-lifetime hologram fixing and ionic conductivity of lithium niobate," to appear in Conference on Laser and Electro-Optics'96.

[30] N. H. Farhat, D. Psaltis, A. Prada, and E. Paek, Appl. Opt. **24**, 1469 (1985).

[31] D. Psaltis and N. H. Farhat, Opt. Lett. **10**, 98 (1985).

[32] B. H. Soffer, G. J. Dunning, Y. Owechko, and E. Marom, Opt. Lett. **11**, 118 (1986).

[33] I. A. Sokolov and S. I. Stepanov, Electron. Lett. **26**, 1275 (1990).

[34] I. A. Sokolov, S. I. Stepanov, and G. S. Trofimov, Sov. Phys. Acoust. **37**, 519 (1991).

[35] P. V. Mitchell, S. W. McCahon, M. B. Klein, T. R. O'Meara, G. J. Dunning, and D. M. Pepper, in Conference on Lasers and Electro-Optics'95, postdeadline paper CPD37, Baltimore, MD (1995).

[36] G. C. Duree, J. L. Shultz, G. J. Salamo, M. Segev, A. Yariv, B. Crosignani, P. DiPorto, E. J. Sharp, and R. R. Neurgaonkar, Phys. Rev. Lett. **71**, 533 (1993).

[37] N. V. Kukhtarev, V. B. Markov, S. G. Odulov, M. S. Soskin, and V. L. Vinetskii, Ferroelectrics **22**, 949 (1979).

[38] J. O. White, M. Cronin-Golomb, B. Fischer, and A. Yariv, Appl. Phys. Lett. **40**, 450 (1982).

[39] J. Feinberg and R. W. Hellwarth, Opt. Lett. **5**, 519 (1980).

[40] M. Cronin-Golomb, B. Fischer, J. O. White, and A. Yariv, IEEE J. Quantum Electron. **QE-20**, 12 (1984).

[41] J. Feinberg, Opt. Lett. **7**, 486 (1982).

[42] R. A. McFarlane and D. G. Steel, Opt. Lett. **8**, 208 (1983).

[43] S.-K. Kwong, M. Cronin-Golomb, B. Fischer, and A. Yariv, IEEE J. Quantum Electron. **QE-22**, 1508 (1986).

[44] S. Weiss, S. Sternklar, and B. Fischer, Opt. Lett. **12**, 114 (1987).

[45] A. Yariv, IEEE J. Qunatum Electron **QE-14**, 650 (1978).

[46] R. W. Hellwarth, J. Opt. Soc. Am. **67**, 1 (1977).

[47] B. Ya. Zel'dovich, N. F. Pilipetsky, and V. V. Shkunov, *Principles of Phase Conjugation*, (Springer-Verlag, Heidelberg 1985).

[48] S. K. Kwong, G. A. Rakuljic, and A. Yariv, Appl. Phys. Lett. **48**, 201 (1986).

[49] R. J. Anderson, E. J. Sharp, G. L. Sharp, G. L. Wood, W. W. Clark, Q. Vuong, G. J. Salamo, and R. R. Neurgaonkar, Opt. Lett. **18**, 986 (1993).

[50] D. Z. Anderson, D. M. Lininger, and J. Feinberg, Opt. Lett. **12**, 123 (19870.

[51] A. Chiou, P. Yeh, C. Yang, and C. Gu, Opt. Lett. **20**, 1125 (1995).

[52] J. Feinberg, Opt. Lett. **8**, 569 (1983).

[53] S. Sternklar, S. Weiss, M. Segev, and B. Fischer, Opt. Lett. **11**, 528 (1986).

Chapter Two

Photorefractive Effect and Photorefractive Nonlinear Optics

2.1 Introduction

Photorefractive effect is generally defined as a light-induced change of the index of refraction of the material. In the field of photorefractive nonlinear optics, however, this term refers to a much narrower class of phenomena, namely, the change in the index of refraction in electrooptic crystals via redistribution of optically excited carriers and buildup of internal space charge fields. Photorefractive phenomenon was first discovered in $LiNbO_3$ by Ashkin *et al.* and classified as "optical damage" [1]. Later developments in the field, described in Chapter 1 of this thesis, led to a better understanding of the underlying physics and chemistry of the effect. According to now adopted band transport model of photorefractivity [2] the photorefractive index change is produced due to the migration of photoexcited carriers, their trapping on the impurity sites and buildup of spatially varying internal space charge field. The microscopic mechanism of migration includes diffusion, drift, and asymmetric excitation (photovoltaic current). The resulting index variation is produced via electrooptic effect.

2.2 Band transport theory

The mechanism of carrier redistribution and index change is described quantitatively by the band transport model first proposed by Kukhtarev [2]. The material is assumed to have extrinsic or intrinsic impurities N_d (donors), some of them being ionized due to the acceptor levels N_a (Figure 2.1). In the simplest case only non-ionized donors are photoactive. In order to obtain the lowest Fourier component of the space charge field, we consider a sinusoidal optical interference pattern in the volume of the photorefractive material (Figure 2.2):

$$I(x) = I_0 + I_1 \cdot e^{ik_g x} + c.c. \quad . \qquad 2.1$$

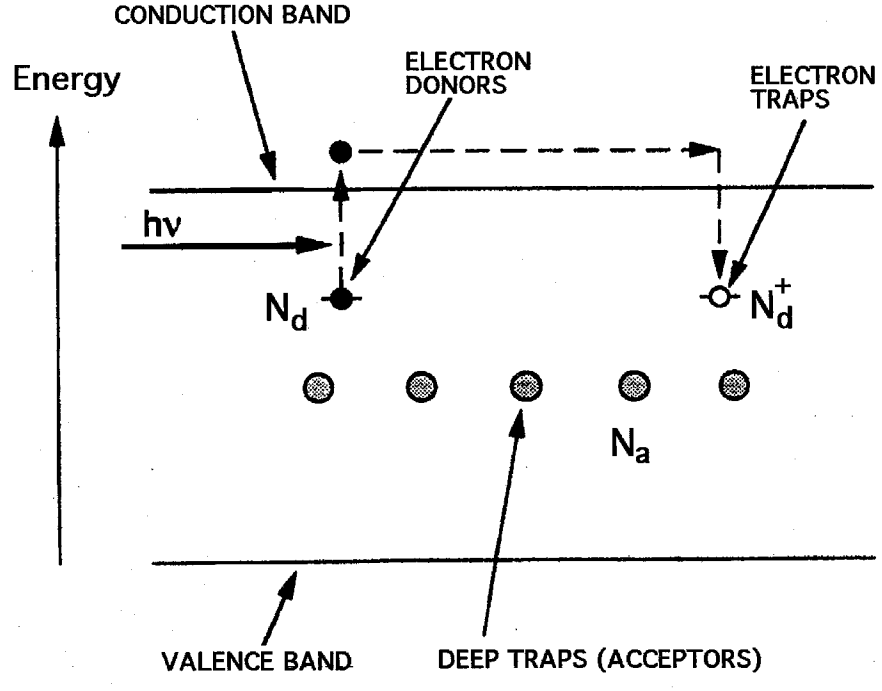

Figure 2.1. Photorefractive band transport model with one photorefractive donor species N_d. Charge compensation condition implies $N_d^+ \cong N_a$ (in the dark).

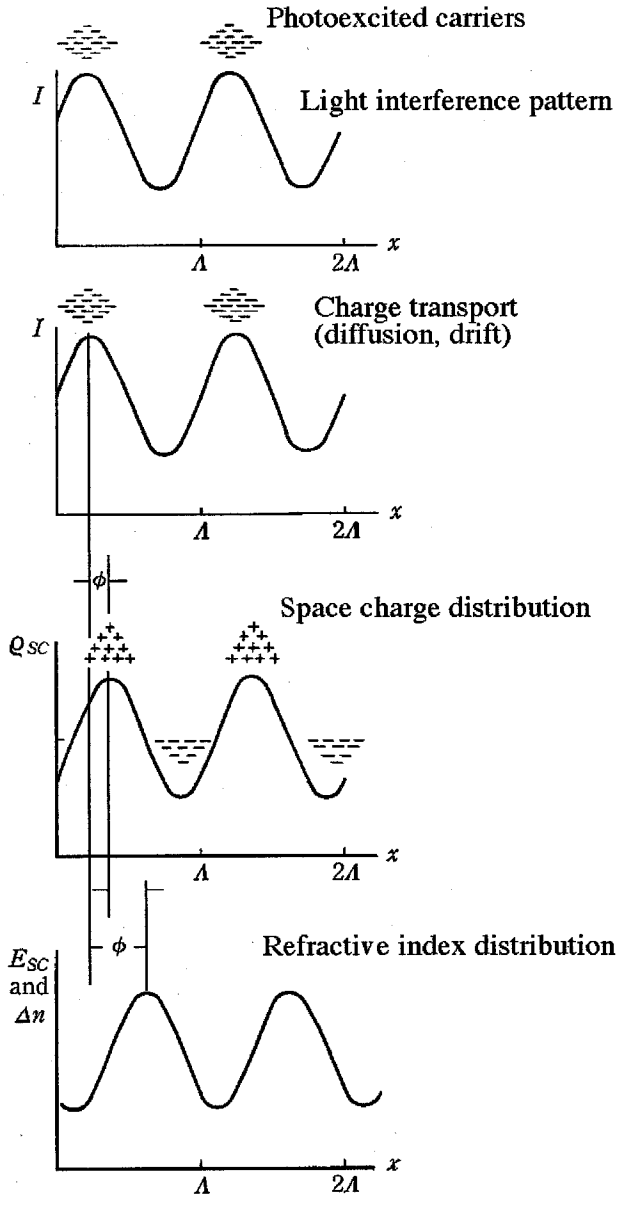

Figure 2.2. Photorefractive mechanism. Two coherent light beams forms interference pattern. Mobile carriers are excited where the intensity is large, migrate to the regions of low intensity, and are trapped by ionized donors. The resulting space charge field induces the refractive index variation through electrooptic effect. ϕ is the phase shift between the interference pattern and the index grating.

The donors are not mobile (same holds for acceptors) and the change in their density is due to the redistribution of electrons. The rate equation for the density of ionized donors in the presence of optical excitation is given by

$$\frac{\partial N_d^+(x,t)}{\partial t} = (\sigma/h\nu I(x) + \beta)(N_d - N_d^+) - \gamma_e N_d^+ n_e , \qquad 2.2$$

where the first term describes photo- and thermal ionization of the neutral donors which density is $N_d - N_d^+$ and the second term represents the recombination of conduction band electrons n_e on ionized donor traps.

Electrons diffuse, drift due to the internal and externally applied electric fields and photovoltaic effect, and create a spatially nonuniform current given by

$$j_e(x,t) = \kappa\, \sigma/h\nu\, I(x)\,(N_d - N_d^+) + \frac{\mu k_b T}{e}\cdot\frac{\partial n_e}{\partial x} + e\mu n_e E_x , \qquad 2.3$$

where the first, second, and third terms represent photovoltaic current, carrier diffusion, and drift, respectively. The rate equation for the density of mobile carriers in the conduction band is

$$\frac{\partial n_e(x,t)}{\partial t} = (\sigma/h\nu\, I(x) + \beta)\,(N_d - N_d^+) - \gamma_e n_e N_d^+ + \frac{1}{e}\frac{\partial j_e}{\partial x} . \qquad 2.4$$

Redistribution of electrons between traps gives rise to an internal, spatially varying space charge field E_{sc}, which is related to the ionized donors density and density of mobile electrons via the Gauss law:

$$\frac{\partial E_{sc}(x,t)}{\partial x} = \frac{e}{\varepsilon\varepsilon_0}\left(N_d^+ - n_e - N_a\right), \qquad 2.5$$

where we already assumed initial charge neutrality of the crystal. The nonlinear coupled equations 2.2-2.5 represent the photorefractive band transport theory. An exact analytic solution of this system of equation can be obtained in the small signal regime ($I_1/I_0 << 1$) by linearization. The amplitude of the fundamental Fourier component E_{sc_1} with spatial periodicity k_g is found to be

$$E_{sc_1} = i\,\frac{E_q(E_d - iE_{p.v.}N_a/N_d)}{E_d + E_q - iE_{p.v.}N_a/N_d}\,\frac{I_1}{I_0}, \qquad 2.6$$

for the short circuited case with photovoltaic effect and no applied field, and

$$E_{sc_1} = i\,\frac{E_q(E_d + iE_0)}{E_d + E_q + iE_0}\,\frac{I_1}{I_0}, \qquad 2.7$$

for the case with no photovoltaic effect (e.g., SBN) and when the crystal is effectively short-circuited by illumination extending from electrode to another (if $E_0 \neq 0$; otherwise the result 2.7 applies regardless the spatial extend of the uniform illumination). The characteristic parameters are defined as follows:

Characteristic photovoltaic field:

$$E_{p.v.} \equiv \frac{\kappa\gamma_e N_a}{e\mu_e}. \qquad 2.8$$

The limiting space charge field:

$$E_q \equiv \frac{eN_a(N_d - N_a)}{\varepsilon\varepsilon_0 k_g N_d}. \qquad 2.9$$

The diffusion field:

$$E_d \equiv \frac{k_g k_b T}{e}. \qquad 2.10$$

The internal space charge field as given by equations 2.6 2.7 creates a periodic variation n_1 in the index of refraction via electrooptic effect. The magnitude of the index perturbation largely depends on the orientation of the crystal, the internal space charge field direction, and electrooptic coefficients of the material. The general formula of electrooptic effect [3] is

$$\Delta\left(\frac{1}{n^2}\right)_{ij} = r_{ijk}E_k. \qquad 2.11$$

Then the fundamental spatial harmonic amplitude of index variation due to internal space charge field E_{sc_1} is given by

$$n_1 = -\frac{r_{eff}n^3}{2}\cdot E_{sc_1}, \qquad 2.12$$

where r_{eff} is the effective electrooptic coefficient.

2.3 Diffraction from fixed volume gratings

The diffraction efficiency η of a refractive index grating which is uniform throughout the volume of the medium of length L is given by Kogelnik's formula [4]:

$$\eta = \sin^2\left(\frac{\pi n_1 L}{\lambda \cos\theta}\right), \qquad 2.13$$

where n_1 is the amplitude of the sinusoidal index perturbation $\delta n(x)$, i.e.,

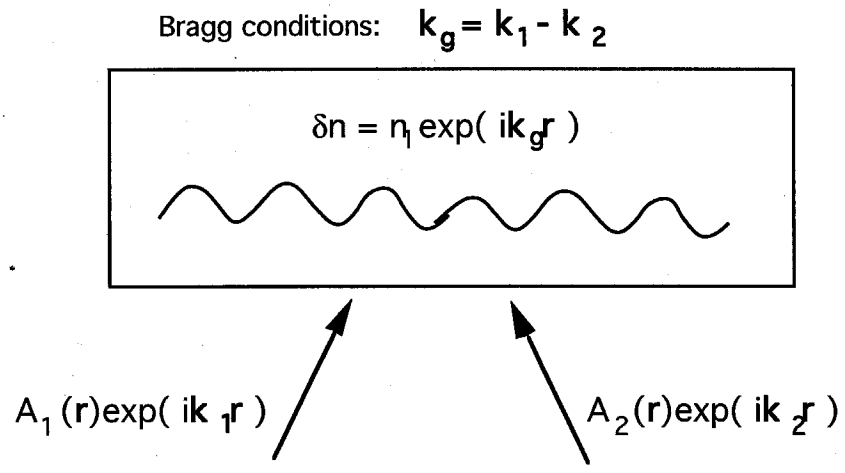

Figure 2.3. Reconstruction of a fixed grating and Bragg conditions.

$$\delta n(x) = \frac{n_1}{2} e^{-i(\mathbf{k_g}\cdot\mathbf{r}+\phi)} + \frac{n_1}{2} e^{i(\mathbf{k_g}\cdot\mathbf{r}+\phi)}, \qquad 2.14$$

and it is assumed that the incident wave is completely phase matched with the index grating (Figure 2.3). If the optical field consists of two plane wave components $A_1(z)$ and $A_2(z)$ whose wavevectors are $\mathbf{k_1}$ and $\mathbf{k_2}$, the phase matching condition is

$$\mathbf{k_1} - \mathbf{k_2} = \mathbf{k_g}. \qquad 2.15$$

If only one of the Bragg matched components is incident on the medium (i.e., $A_2(0) = 0$), the diffraction efficiency defines the intensity of the diffracted signal, i.e.,

$$\eta \equiv \frac{I_2(L)}{I_1(0)}. \qquad 2.16$$

The volumetric interaction provides selectivity, i.e., the diffraction efficiency decreases dramatically as the Bragg-condition 2.15 is violated. For a transmission grating this dependence is given by

$$\eta(\Delta k) \cong \eta(0)\cdot \mathrm{sinc}^2(\Delta kL/2), \qquad 2.17$$

where $\Delta k = |\mathbf{k_1} - \mathbf{k_2} - \mathbf{k_g}|$.

2.4 Introduction to holographic data storage

Holographic data storage [5] exploits the selectivity provided by the volumetric interaction to store multiplexed holograms which can be retrieved independently (Figure 2.4). Multiple holograms can be recorded in a material by changing either the reference beam angle [6], the recording wavelength [7], or by phase coding the reference beam [8]. The basic principle of holographic storage is as follows (Figure 2.5). During the recording stage the index perturbation δn_i is created in the material due to the interference between the signal, information carrying beam S_i and its reference beam R_i. δn_i can be written as

$$\delta n_i \approx \left(R_i^* S_i + R_i S_i^* \right). \qquad 2.18$$

The total index perturbation δn is a sum over the index perturbations due to individual multiplexed holograms:

$$\delta n \approx \Sigma_{i=1}^{N} \left(R_i^* S_i + R_i S_i^* \right). \qquad 2.19$$

The retrieval of a page i is achieved by shining the corresponding reference signal R_i into the medium with recorded index variation 2.19. The interaction of the optical wave R_i with δn gives rise to a polarization wave P_i:

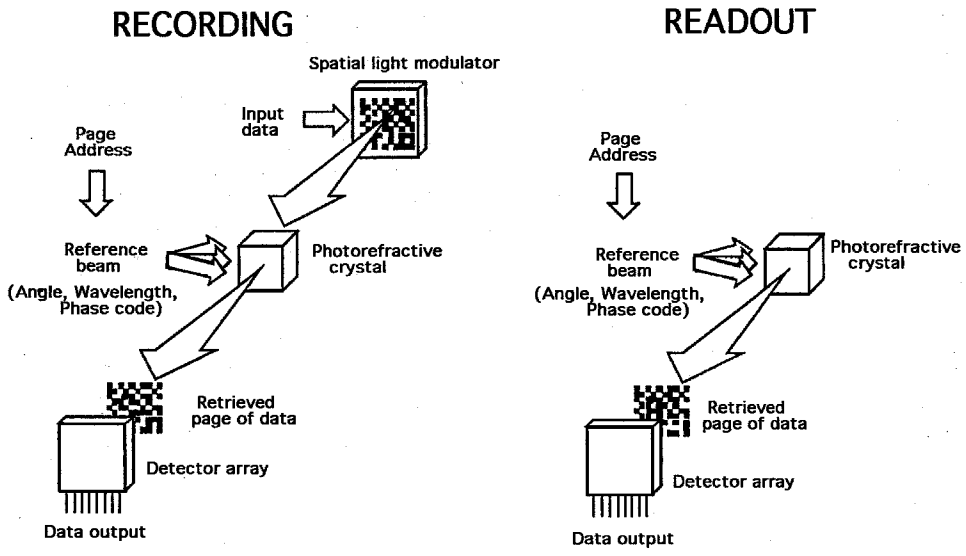

Figure 2.4. Simplified diagram of a holographic data storage system.

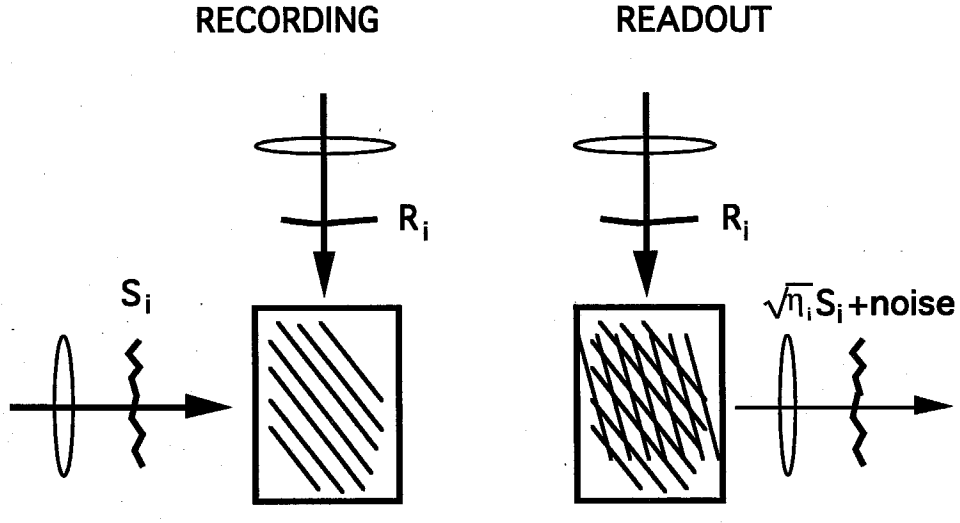

Figure 2.5. Basic principle of holographic storage, multiplexing, and retrieval of stored data.

$$P_i + c.c. \propto \delta n \cdot R_i + c.c. \propto S_i \cdot \left|R_i^2\right| + \sum_{j=1}^{j\neq i} \left(R_j^* S_j + R_j S_j^* \right) \cdot R_i + c.c. . \qquad 2.20$$

The first term corresponds to reconstruction of the initial information page S_i, while the second term (the sum) represents the non-phase matched contributions, i.e., cross-talk. The amplitude of the reconstructed wave is then obtained by integrating 2.20 throughout the volume of the crystal. Bragg-selectivity (equation 2.17) provided by volume interaction leads to preferential growth of the phase matched component (i.e., stored information) compared to the cross-talk. Cross-talk and its limitations on the signal-to-noise ratio and storage capacity have been studied extensively. Comprehensive discussions of various sources of cross-talk in different multiplexing schemes may be found in references [9-12]. Other limitations on storage capacity arise from the noise in optical detection and finite dynamic range of the media. These are discussed in Chapter 5 and references therein.

2.5 Hologram fixing in photorefractive materials

Photorefractive index gratings decay upon continuous readout (or under uniform illumination) due to the same mechanism which is responsible for their creation - electronic transport. Hologram fixing techniques involve reproduction of the original electronic pattern into the form in which the species responsible for the formation of the hologram are not optically inactive. Two of such techniques involve thermally assisted ionic compensation and spontaneous polarization modulation.

Complete fixing of holograms can be achieved by transforming the electronic space charge pattern into an optically inactive quasi-permanent ionic charge pattern. For the first time this has been demonstrated in $LiNbO_3$ [13]. The ionic conductivity obeys the Arrhenius-type dependence on the temperature T:

$$\sigma_i = en_i\mu_o\exp(-E_a/k_bT). \qquad 2.21$$

At elevated temperature (T > ~70°C in lithium niobate) the ionic conductivity prevails over the dark electronic conductivity and the ionic motion relaxes the electronic space charge. When the crystal is cooled back to room temperature and illuminated, the electronic grating is partially erased, leaving behind the ionic charge field which now represents an ionic fixed hologram (Figure 2.6). The ionic hologram is quasi-stabilized due to partial compensation by electronic grating. The shelf lifetime of the fixed grating depends largely on the ionic impurity contents (n_i in equation 2.21) and degree of electronic compensation. The lifetimes of uncompensated ionic gratings can range from a few months (in as-grown $LiNbO_3$) to 2-3 years in dehydrated lithium niobate. Strongly compensated gratings with low reconstruction efficiency may possess a lifetime of 10 years and more (see Chapter 4, discussions and references therein).

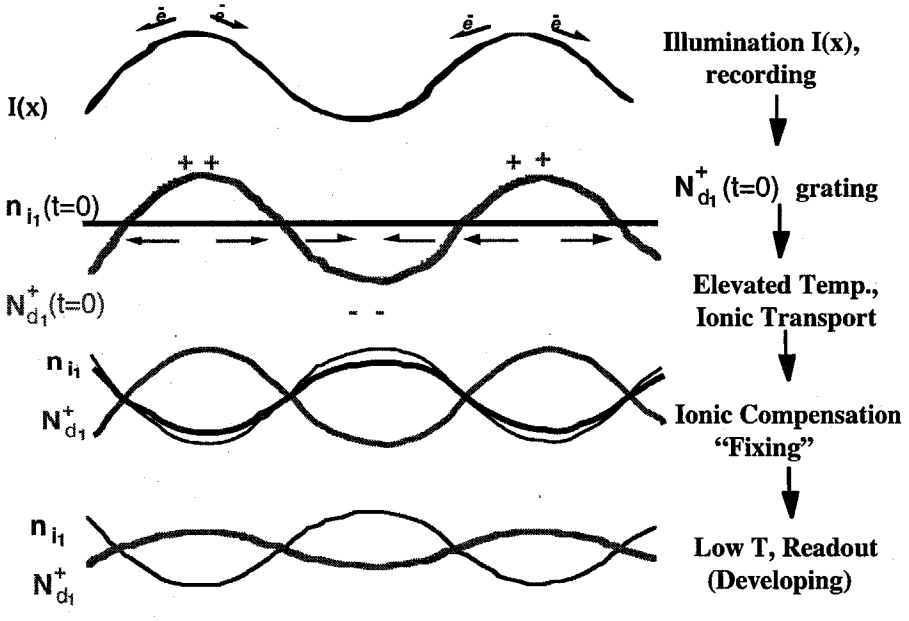

Figure 2.6. Mechanism of hologram fixing via thermally assisted ionic drift.

Fixing of photoinduced grating can also be achieved by means of partial polarization reversal in regions of high depoling space charge fields. This was accomplished both in ferroelectrics with "diffused" phase transition, such as $Sr_{0.75}Ba_{0.25}Nb_2O_6$ [15], and in "classical" ferroelectrics with sharp phase transition point, such as $BaTiO_3$ [14]. Typical fixing scheme involves application of an external depoling field below the coersive field for bulk ferroelectric switching (Figure 2.7). The microscopic mechanisms responsible for polarization switching [16, 17] include antiparallel microdomain nucleation and their subsequent lateral and sidewise expansion. The domain nucleation probability p(x), which is given by [16]

$$p(x) \propto \exp(-\alpha/E(x)), \qquad 2.22$$

is maximal in the regions of large depoling fields ($E(x) = E_{sc}(x) + E_0$; α in equation 2.22 is a temperature dependent parameter). The antiparallel domain nucleation can be largely enhanced by externally applied voltage E_0 which negatively biases the internal space charge (Figure 2.6). The nucleated microdomains typically have spike-shape form oriented along the *c*-axis, because such geometry decreases the depolarization energy [17]. The nucleation is followed by domain growth. The latter leads both to stronger compensation of the electronic space charge and to partial depoling of the crystal as a whole. The microdomains formation is correlated with the spatial profile of the internal space charge field through both the nucleation probability (equation 2.22) and the growth rate, which depends on the local field amplitude [16]. Spatial variation of the spontaneous polarization P_s is, therefore, also correlated with the space charge field $E_{sc}(x)$. The first fundamental Fourier harmonic P_{s1} of the perturbed spontaneous polarization represents the fixed polarization hologram. The magnitude of the space charge variation ρ_1 of the polarization grating is given by $\rho_1 = -\nabla P_{s1}$. The correlated portion of the polarization variation is quite small, typically of the order of 10^{-3} to 10^{-4} compared to the total P_s. Upon reconstruction the P_{s1} grating is

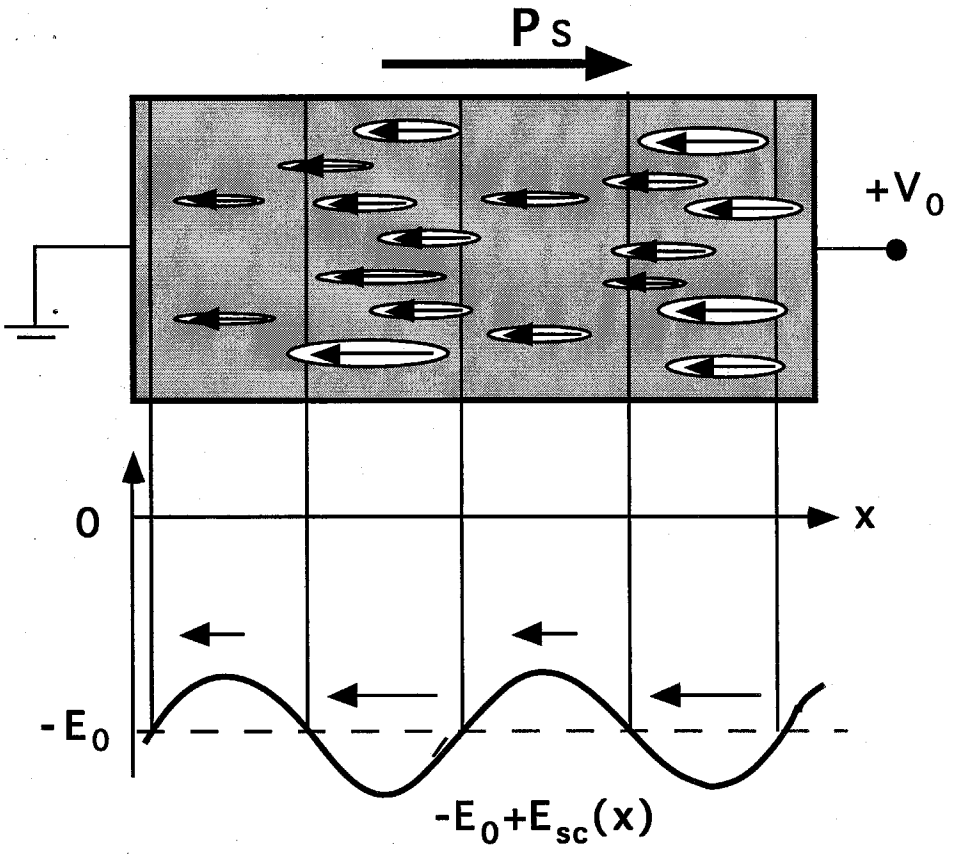

Figure 2.7. Ferroelectric domain fixing schematic. Antiparallel microdomains are nucleated most intensely in the regions of most negative electric field. They continue to grow leading both to a partial compensation of the hologram space charge and to depoling of the crystal (reduction of effective electrooptic coefficient). External depoling electric field can be applied (during or after the recording) in order to enhance microdomain nucleation and growth. Microdomains distribution spatially correlated with space charge field constitutes the fixed polarization hologram.

compensated by dynamic photorefractive space charge. The ferroelectric domain fixing is discussed in more detail in Chapter 3.

2.6 Wave-mixing and coupled waves theory

Photorefractive mechanism allows dynamic interaction of the incident light beam with its own diffracted component and the induced refractive index pattern inside the volume of the recording medium [4]. The refractive index change gives rise to a phase and intensity redistribution of the interference pattern of interacting waves, this, in turn, is reflected in the spatial profile of the index variation. In this section we review the basic results of two-beam coupling caused by a phase between the light interference pattern and the index grating in photorefractive crystals (equation 2.12). The optical electric field of two plane waves interacting within the volume of photorefractive material (Figure 2.8) can be written as

$$E_j = A_j(\mathbf{r}) \exp\left(i(\mathbf{k}_j \cdot \mathbf{r} - \omega t)\right) + \text{c.c.}, \quad j = 1, 2 \qquad 2.23$$

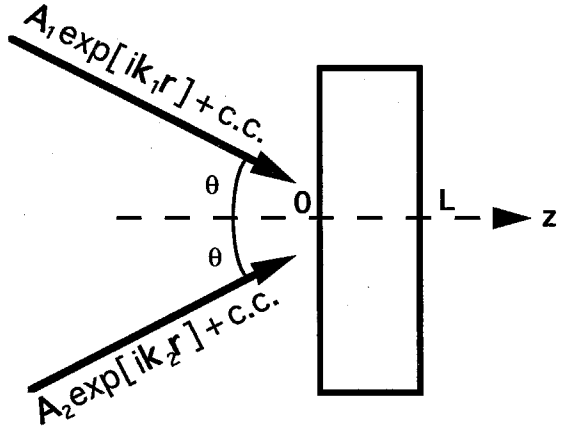

Figure 2.8. A schematic diagram of two-wave mixing in photorefractive materials.

The two coherent beams write an interference pattern which gives rise to a refractive index perturbation due to photorefractive effect:

$$\delta n = n_1 \frac{A_1 A_2^*}{I_0} \exp\left(- i(\mathbf{k}_1 - \mathbf{k}_2)\cdot\mathbf{r}\right) + n_1^* \frac{A_1^* A_2}{I_0} \exp\left(i(\mathbf{k}_1 - \mathbf{k}_2)\cdot\mathbf{r}\right), \qquad 2.24$$

where $I_0 = I_1 + I_2$ is the total intensity, and the index grating amplitude is given by equations 2.12, 2.6, and 2.7 (with term I_1/I_0 omitted in 2.6 and 2.7). Substituting the index variation into the scalar wave equation and invoking the slowly varying amplitude approximation one arrives to the following coupled waves equations [3]:

$$\frac{dA_1}{ds} = - \frac{\gamma}{I_0} \left(A_1 A_2^*\right) A_2 - \frac{\alpha}{2} A_1, \qquad 2.25$$

$$\frac{dA_2}{ds} = \frac{\gamma^*}{I_0} \left(A_1^* A_2\right) A_1 - \frac{\alpha}{2} A_2, \qquad 2.26$$

where $s = z/\cos\theta$ and coupling constant γ is given by

$$\gamma = \frac{i\omega n_1}{2c}. \qquad 2.27$$

For the case of two incident beams the boundary conditions can be written as

$$A_1(z=0) = \sqrt{I_1} \exp\left(i\varphi_1(z=0)\right), \qquad 2.28$$

$$A_1(z=0) = \sqrt{I_1} \exp\left(i\varphi_1(z=0)\right). \qquad 2.29$$

The solution of the coupled waves equations 2.25 and 2.26 is then given by [3]

$$I_1(s) = \frac{I_0(0) \exp(- \alpha s)}{1 + (I_2(0) / I_1(0)) \exp(\Gamma s)}, \qquad 2.30$$

$$I_2(s) = \frac{I_0(0)\exp(-\alpha s)}{1 + (I_1(0)/I_2(0))\exp(-\Gamma s)}, \qquad 2.31$$

$$\varphi_1(s) = \varphi_1(0) - \Gamma' s + \frac{\Gamma'}{\Gamma}\ln\left[\frac{1 + (I_1(0)/I_2(0))}{1 + (I_1(0)/I_2(0))\exp(\Gamma s)}\right], \qquad 2.32$$

$$\varphi_2(s) = \varphi_2(0) - \Gamma' s + \frac{\Gamma'}{\Gamma}\ln\left[\frac{1 + (I_2(0)/I_1(0))}{1 + (I_2(0)/I_1(0))\exp(\Gamma s)}\right], \qquad 2.33$$

where $\Gamma = 2\mathrm{Re}[\gamma]$ and $\Gamma' = \mathrm{Im}[\gamma]$. Equations 2.30 and 2,31 describe the coherent holographic amplification (gain), while equations 2.32 and 2.33 describe phase coupling between interacting waves. Optical gain without phase coupling is realized when the coupling constant γ is purely real. This is the case when the index variation is $\pi/2$ phase shifted with respect to the interference pattern (i.e., pure diffusion response without externally applied field or photovoltaic effect). Phase coupling leads to the, so called, "hologram bending" in, e.g., lithium niobate crystals where the photorefractive response is primarily due to the photovoltaic effect and corresponding phase shift between the index change and the interference pattern is close to zero.

2.7 Introduction to four-wave mixing and phase conjugation

The phase conjugate replica of a monochromatic field is a field of the same frequency, whose wavefronts take the same shape throughout space, but propagate in the opposite direction at every point [3]. A wave traveling in the positive z direction can be written as

$$E(\mathbf{r},t) = A(\mathbf{r})\exp(i(kz - \omega t)). \qquad 2.34$$

The phase conjugate field is obtained by taking a complex conjugate of the spatial part in equation 2.34:

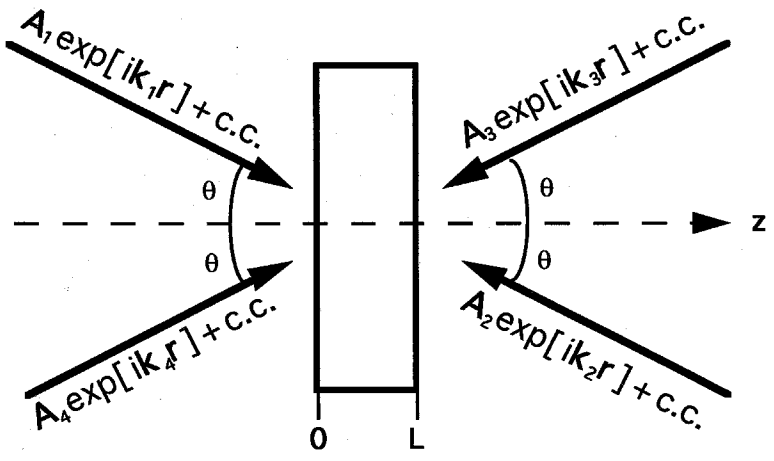

Figure 2.9. A schematic diagram of four-wave mixing in photorefractive materials.

$$E_{PC}(\mathbf{r},t) = A^{*}(\mathbf{r})\exp(i(kz + \omega t)). \qquad 2.35$$

Four-wave mixing (Figure 2.9) is a process of interaction of four optical waves in nonlinear medium. In the simplest case it involves two counterpropagating pump beams and an input signal beam. The result of four-wave mixing interaction is the buildup of the fourth beam - the phase conjugate replica of the signal - due to the diffraction of one of the pumps off the grating recorded between the signal and the other pump.

The electric field amplitudes of the beams in Figure 2.9 are given by the expressions, similar to the ones for the two-wave mixing case:

$$E_j(\mathbf{r},t) = A_j(\mathbf{r})\exp(i(\mathbf{k}_j\cdot\mathbf{r} - \omega t)) + \text{c.c.}, \quad j = 1, \ldots, 4 \qquad 2.36$$

For the most general case there are four different possible sets of index gratings [18] whose grating vectors are given by:

$$\mathbf{k}_I = \mathbf{k}_4 - \mathbf{k}_1 = \mathbf{k}_2 - \mathbf{k}_3 , \qquad 2.37$$

$$\mathbf{k}_{II} = \mathbf{k}_1 - \mathbf{k}_3 = \mathbf{k}_4 - \mathbf{k}_2 , \qquad 2.38$$

$$\mathbf{k}_{III} = \mathbf{k}_1 - \mathbf{k}_2 , \qquad 2.39$$

$$\mathbf{k}_{IV} = \mathbf{k}_4 - \mathbf{k}_3 . \qquad 2.40$$

The photoinduced photorefractive index variation is given by a superposition of these four gratings ($I_0 = \Sigma I_j$):

$$\delta n = \frac{n_I}{2}\frac{A_1^* A_4 + A_2 A_3^*}{I_0} \exp(i\mathbf{k}_I \cdot \mathbf{r}) + \frac{n_{II}}{2}\frac{A_1 A_3^* + A_2^* A_4}{I_0} \exp(i\mathbf{k}_{II} \cdot \mathbf{r}) + \frac{n_{III}}{2}\frac{A_1 A_2^*}{I_0} \exp(i\mathbf{k}_{III} \cdot \mathbf{r}) + \frac{n_{IV}}{2}\frac{A_3^* A_4}{I_0} \exp(i\mathbf{k}_{IV} \cdot \mathbf{r}) + \text{c.c.} . \qquad 2.41$$

The general expression for the coupled waves equation in four-wave mixing problem can be obtained by substituting 2.41 and 2.36 into the scalar wave equation [18]. A complete analytic solution for general case is not presently available. Note also that gratings $\mathbf{k}_{II}$, $\mathbf{k}_{III}$, and $\mathbf{k}_{IV}$ are the reflection gratings (in the conditions of Figure 2.9), while $\mathbf{k}_I$ is a transmission grating. The predominance of one grating is common in most experimental situations due to the directions, polarizations, crystal orientation, and coherence relationships of the four beams. For the most typical case when the transmission grating $\mathbf{k}_I$ dominates the coupled waves equations for the slowly varying amplitude A_j of the four interacting waves can be written as [18]:

$$\cos\theta \frac{dA_1}{dz} = -i \frac{\pi n_I}{\lambda} \frac{A_1 A_4^* + A_2^* A_3}{I_0} A_4 - \frac{\alpha}{2} A_1 , \qquad 2.42$$

$$\cos\theta \frac{dA_2}{dz} = i \frac{\pi n_I}{\lambda} \frac{A_1^* A_4 + A_2 A_3^*}{I_0} A_3 + \frac{\alpha}{2} A_2 , \qquad 2.43$$

$$\cos\theta \frac{dA_3}{dz} = i \frac{\pi n_I}{\lambda} \frac{A_1 A_4^* + A_2^* A_3}{I_0} A_2 + \frac{\alpha}{2} A_3 , \qquad 2.44$$

$$\cos\theta \frac{dA_4}{dz} = - i \frac{\pi n_I}{\lambda} \frac{A_1^* A_4 + A_2 A_3^*}{I_0} A_1 - \frac{\alpha}{2} A_4 . \qquad 2.45$$

The solution of coupled-waves equations 2.42-2.45 and, e.g., oscillation threshold values, are determined by the boundary conditions, which are given by the corresponding geometry of the specific four-wave mixing configuration. The specific case of a double phase conjugate mirror, which has only two input beams (say A_2 and A_4, or A_1 and A_3) is considered in Chapter 6.

2.8 Summary

Photorefractive effect is produced by photoinduced redistribution of charges in the volume of the crystal and electrooptic effect. Quantitatively, the photorefractive effect is described by the band transport model which includes the rate equations for ionized donors and free conduction band electrons and Gauss law. Photorefractive holograms can be fixed using thermally assisted ionic transport or spontaneous ferroelectric polarization variation. Applications of fixed photorefractive gratings include the volumetric three-dimensional storage of information with theoretical diffraction limit of V/λ^3 bits in a volume V. Nonlinear wave-mixing via dynamic photorefractive gratings gives rise to coherent amplification and phase conjugation of optical beams.

References for Chapter Two

[1] A. Ashkin, G. D. Boyd, J. M. Dziedzic, R. G. Smith, A. A. Ballmann, H. J. Levinstein, and K. Nassau, Appl. Phys. Lett. **9**, 72 (1966).

[2] N. V. Kukhtarev, Sov. Tech. Phys. Lett. **2**, 438 (1976).

[3] A. Yariv, *Optical Electronics*, 3rd edition, (Holt, Rinehart, and Winston, New York, 1985).

[4] H. Kogelnik, Bell Syst. Tech. J. **48**, 2909 (1969).

[5] E. N. Leith, A. Kozma, J. Upatneiks, J. Marks, and N. Massey, Appl. Opt. **5**, 1303 (1966).

[6] L. d'Auria, J. P. Huignard, C. Slezak, and E. Spitz, Appl. Opt. **13**, 808 (1974).

[7] G. A. Rakuljic, V. Leyva, and A. Yariv, Opt. Lett. **17**, 1471 (1995).

[8] J. E. Ford, Y. Fainmann, and S. H. Lee, Opt. Lett. **15**, 1088 (1990).

[9] W. J. Burke and P. Sheng, J. Appl. Phys. **48**, 681 (1977).

[10] D. Psaltis, C. Gu, and D. Brady, in Proceedings of the SPIE, SPIE. (1988).

[11] A. Yariv, Opt. Lett. **18**, 652 (1993).

[12] K. Curtis and D. Psaltis, J. Opt. Soc. Am. A **10**, 2547 (1993).

[13] D. L. Staebler and J. J. Amodei, Ferroelectrics **3**, 107 (1972).

[14] F. Micheron and G. Bismuth, Appl. Phys. Lett. **20**, 79 (1972).

[15] F. Micheron and G. Bismuth, Appl. Phys. Lett. **23**, 71 (1973).

[16] A. G. Chynoweth, Phys. Rev. **102**, 705 (1956).

[17] R. Landauer, J. Appl. Phys. **28**, 227 (1957).

[18] M. Cronin-Golomb, B. Fischer, J. O. White, and A. Yariv, IEEE J. Quantum Electron. **QE-20**, 12 (1984).

Chapter Three

Electrical Ferroelectric Domain Fixing in Photorefractive Strontium - Barium Niobate

3.1 Introduction

Volume holograms recorded in photorefractive materials can find important applications in optical memories and optical computing systems. However, the photorefractive holograms are normally erased by the readout light. Nondestructive readout can be achieved by hologram fixing, and several fixing methods have been reported. Fixing of holograms via thermally activated ionic transport was demonstrated in $LiNbO_3$ [1], $Bi_{12}SiO_{20}$ [2], $KNbO_3$ [3], and $BaTiO_3$ [4], where a compensating ionic charge grating (which cannot be erased optically) is formed at an elevated crystal temperature. The hologram fixing has been demonstrated in $Sr_{0.75}Ba_{0.25}Nb_2O_6$ [5,6] (SBN:75) and $BaTiO_3$ [7] through the creation of a ferroelectric domain pattern by applying an external field at room temperature. Hologram fixing in SBN:75 was also achieved by cooling the exposed crystal through the ferroelectric phase transition [8], by prolonged high intensity recording [9,10], and with the use of screening of externally applied voltage [11]. Leyva *et al.* demonstrated hologram fixing in $KTa_{1-x}Nb_xO_3$ by cooling the exposed crystal under an

applied field through the ferroelectric phase transition [12]. In general, electrical fixing is preferable from the practical point of view because of its relative simplicity. Besides, it allows fast (< 1 second) fixing without a change in the temperature of the recording crystal, what is particularly important in highly multiplexed storage of high-bandwidth holograms [13].

3.2 Ferroelectric domain fixing in SBN:75

In this Section we report the results of our investigation on electrical fixing of photorefractive holograms recorded in SBN:75. We were able to reproduce some of the effects that Micheron and Bismuth reported in Ref. [5], but our observations are different in several important respects. In addition, we established two novel ways of electrically fixing holograms in SBN:75 that give improved performance and demonstrated that holograms of images can be fixed and faithfully reproduced.

The crystal sample used in the experiment was grown and poled at Rockwell International Science Center. It has dimensions of 6 mm × 6 mm × 6 mm, with its *c*-axis parallel to the edges. An external electric field can be applied along the *c*-axis, and it is called positive (negative) if its direction is the same as (the opposite of) that of the initial poling filed. In our experimental setup (Fig. 3.1), an ordinary-polarized plane wave from an argon laser ($\lambda = 488$ nm) is split into three beams, two of which are used for recording a grating in the crystal, with the third used as a non-Bragg-matched erasing beam. The grating vectors are approximately parallel to the c axis and the total recording intensity is 10 mW/cm^2. The diffraction efficiency η is monitored with a low-intensity, extraordinary-polarized He-Ne laser beam incident at the Bragg angle. The diffraction efficiency is calculated by subtracting the background noise level from the measured diffracted light and dividing the difference by the transmitted light power.

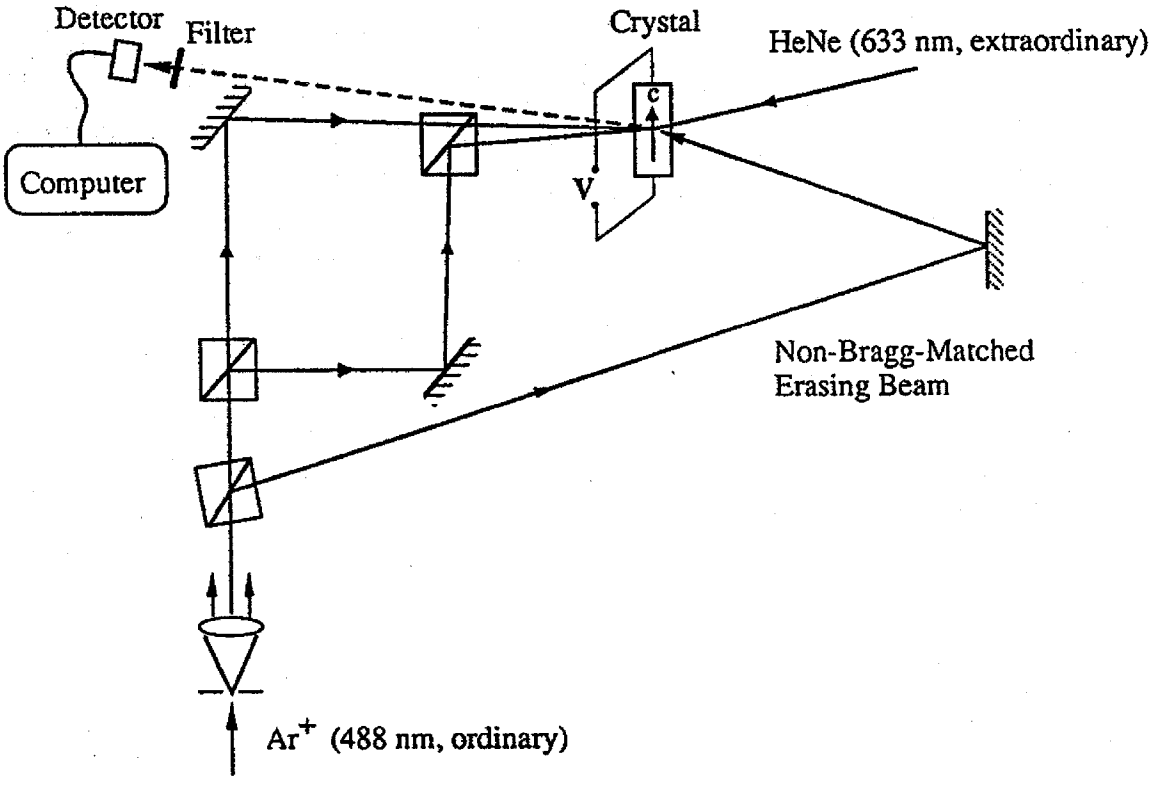

Figure 3.1. Optical setup.

In the first experiment, a holographic grating with a grating spacing Λ = 11.6 μm was recorded in the completely poled crystal without any applied field. After the diffraction efficiency η reached its saturation value (η = 11%), the recording beams were blocked, and a negative-voltage pulse with amplitude V = -1 kV and duration of t = 0.5 s was applied to the crystal, which caused η to fall rapidly. After the voltage was removed, η recovered a portion of its initial value before the pulse. Then the crystal was illuminated with the non-Bragg-matched erasing beam, and η decreased further until it reached a steady-state value of $\eta \approx 0.06\%$. This fixed grating could not be erased by the erasing

beam. Then the erasing beam was blocked, and a positive-voltage pulse, with amplitude V = +2 kV and duration of a few seconds, was applied to the crystal. During the positive-voltage pulse, $\eta = 1.8\%$, and after the pulse a grating with $\eta = 0.4\%$ was revealed. This revealed grating can be optically erased. The experimental results of recording, fixing, revealing, and erasing are shown in Fig. 3.2, where the diffracted signal is plotted as a function of time during the different stages of the experiment.

Comparing the results in Fig. 3.2 with Ref. 5, we see that we were able to achieve electrical fixing, but the fixed grating obtained in our experiment is much weaker than that in Ref. 5. Another important difference is our observation of a revealed grating on application of a strong positive voltage across the crystal at relatively large grating spacings.

We have found that in general the strengths of the fixed grating and the revealed grating can be greatly enhanced by applying a constant negative voltage during recording. With an applied voltage of V = -500 V, we recorded a grating with $\Lambda = 11.6\ \mu m$, using an exposure time of 50 s. Then the recording beams were blocked, the applied voltage was removed, and the grating was allowed to settle down to a steady level. Upon illumination of the crystal with the erasing beam, η decreased first and then rose back to a steady state,-indicating a fixed grating of $\eta = 0.8\%$. Finally, a positive-voltage pulse, the same as the one used in the previous experiment, was applied, which revealed a grating of $\eta = 0.5\%$. This experimental result is shown in Fig. 3.3.

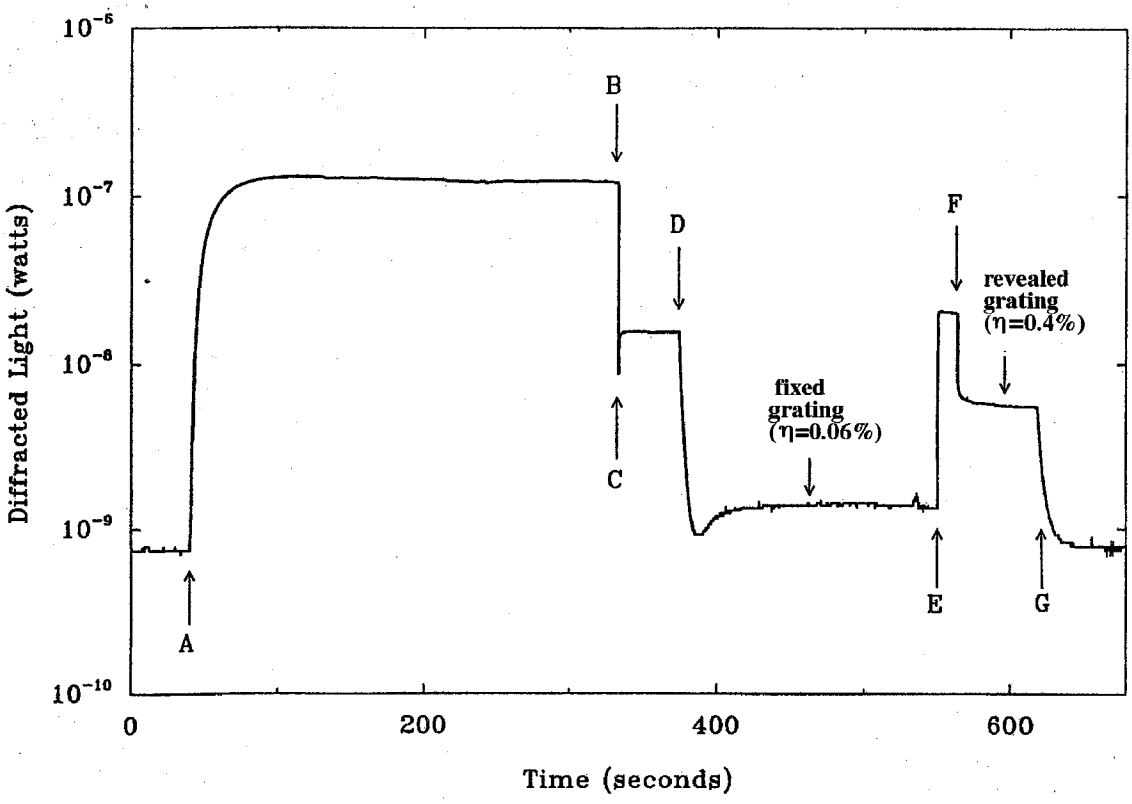

Figure 3.2. Diffracted light as a function of time for fixing with a negative-voltage pulse ($\Lambda = 11.6\ \mu m$). The transmitted light power in the absence of the grating is 1.1 μW. A, Hologram recording begins. B, Negative pulse is applied. C, End of negative pulse. D, Optical erasure begins. E, Erasing beam is blocked and positive voltage pulse is applied. F, End of positive pulse. G, Optical erasure begins.

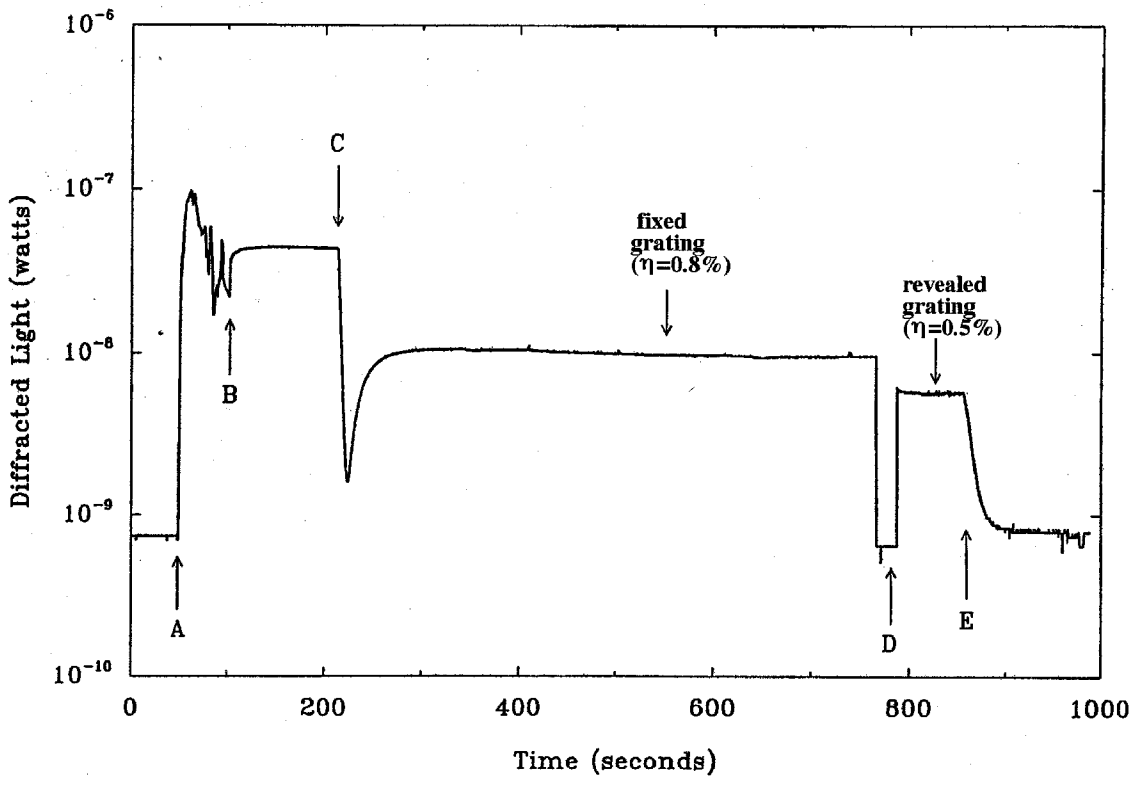

Figure 3.3. Diffracted light as a function of time for fixing with a constant negative voltage during recording (Λ = 11.6 μm). The transmitted light power in the absence of the grating is 1.1 μW. A, Hologram recording begins and negative voltage is applied. B, Negative voltage is removed and recording beams are blocked. C, Optical erasure begins. D, Positive-voltage pulse is applied (probe beam is blocked). E, Optical erasure begins.

The experiment described above was repeated for several different grating spacings, and the results are summarized in Fig. 3.4. Under our experimental conditions, the maximum diffraction efficiency of the fixed grating is found to be 0.8% at Λ = 11.6 μm. The revealed grating is observed only for relatively large Λ, and its strength increases drastically with Λ, achieving approximately 17% diffraction efficiency at Λ = 29 μm.

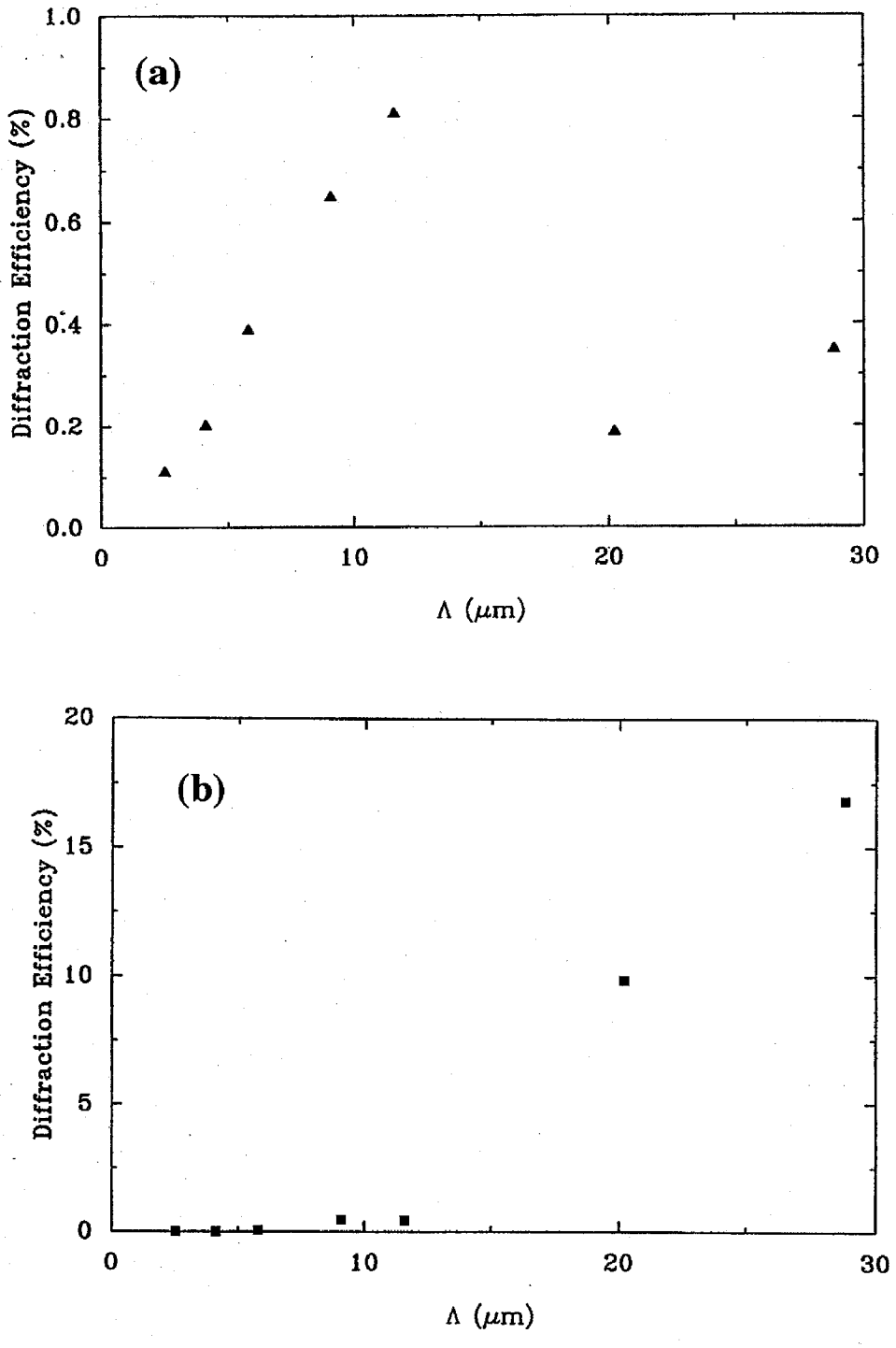

Figure 3.4. Diffraction efficiency as a function of grating spacing for (a) the fixed grating and (b) the revealed grating.

Finally, an image was recorded in the crystal as an image plane hologram, and Figure 3.5(a) shows the reconstruction of the initial hologram. Figure 3.5(b) shows the reconstruction of the fixed hologram. The fixed hologram did not show any sign of degradation under illumination with the non-Bragg-matched erasing beam for 2.5 hours.

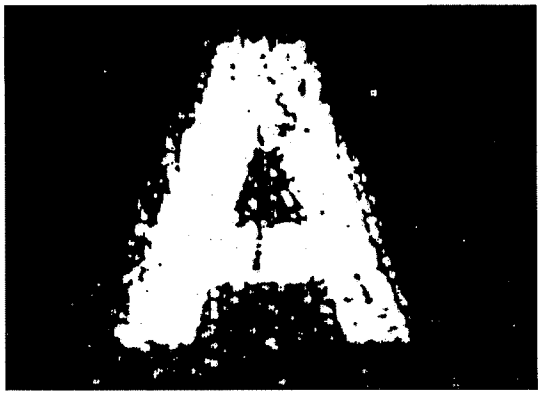

(a)

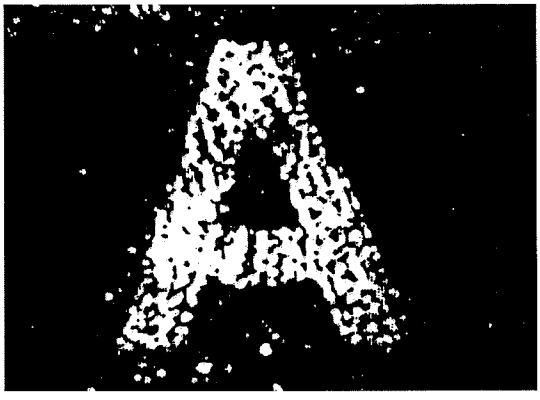

(b)

Figure 3.5. (a) Reconstruction of the recorded hologram and (b) reconstruction of the fixed hologram.

The fixing-and-revealing process that we described was not observed when a positive rather than a negative fixing voltage was applied. If we assume that the mechanism responsible for fixing involves compensating ions, then we have no obvious explanation for the asymmetry regarding the polarity of the fixing voltage. Similarly, if the mechanism involved two types of photorefractive species [14], the effect would not be sensitive to the polarity of the fixing voltage. The fact that the fixed grating can be electrically erased nearly instantaneously (less than 0.1 s) in the dark (i.e., without redistribution of charge carriers among the trap sites) also indicates that the effect does not involve two types of trap site that compensate for each other. Therefore we conclude that the mechanism responsible for this effect is the polarization grating formation suggested in [5].

Specifically, our observations can be explained as follows. With the aid of the negative external field, the electronic space-charge field established during the holographic recording causes a spatial modulation of the ferroelectric polarization. In the areas where the space-charge field is negative, the local polarization is modified (which corresponds to local depoling or possible repoling in the opposite direction). This causes the decrease of both the mean linear electrooptic coefficient and the amplitude of the space-charge field modulation. As a result, the amplitude of the refractive-index modulation decreases on application of a negative voltage pulse, causing the drop in the monitored diffraction efficiency. Under the illumination of the erasing beam, the electronic grating is erased further, until a balance between the polarization grating and the electronic grating is reached. The fixed grating observed is attributed to the polarization grating for which the electronic grating partially compensates. Finally, a strong positive voltage applied to the crystal erases the polarization grating (i.e., the ferroelectric domains are realigned), revealing the compensating electronic grating [15], which of course can be erased optically. The enhancement of the diffraction efficiency of the revealed grating during the positive

voltage pulse (see Fig. 2) is due to the nonlinear electrooptic effect in SBN:75 [16]. A physical model that describes the electronic compensation and revealing process will be introduce in the next section. The predicted dependence of the diffraction efficiencies on the grating spacing closely matches our experimental observations [15].

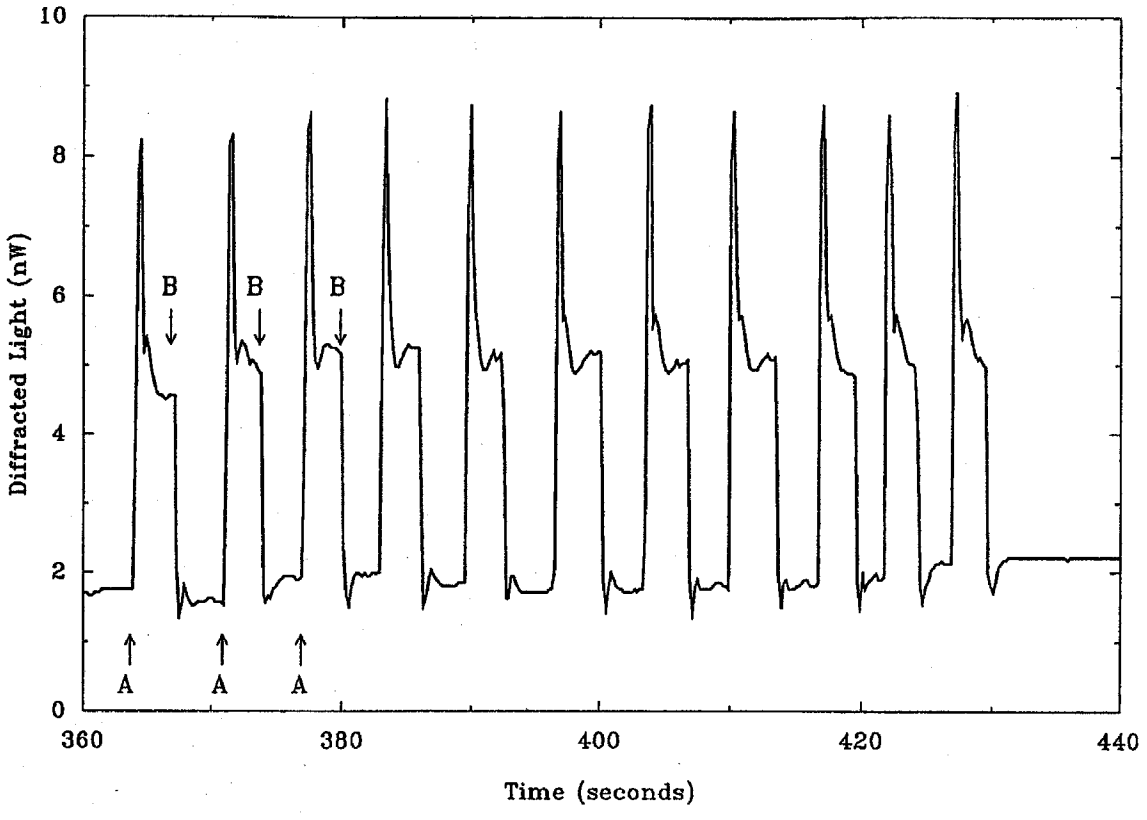

Figure 3.6. Cyclic fixing and revealing of the stored hologram ($\Lambda = 20.2\ \mu m$), with the erasing beam off during the entire process. A, Positive (revealing) pulse is applied with V = + 1 kV. B, Negative (fixing) pulse is applied, with V = - 1 kV.

The above experiments suggest two modes of hologram fixing in SBN:75 crystals: the fixed polarization grating and the revealed electronic grating. Although the revealing process is destructive to the polarization grating, it is possible to recreate this polarization grating by applying a negative-voltage pulse after the electronic grating is revealed. These revealing/fixing cycles were repeatedly performed (shown in Fig. 3.6), and the diffraction efficiency of the revealed grating (and thus the polarization grating) remained unchanged. A similar procedure was used successfully to record and high efficiency multiplexed holograms in SBN:75. In the multiple-cycle exposure technique [13] the entire exposure (i.e., recording of 1000 holograms) was divided into multiple cycles, and the electrical revealing and fixing pulses were applied at the end of each cycle. The individual diffraction efficiency of multiplexed fixed holograms was found to be much larger than that using a single-cycle exposure. First, the previously fixed holograms don't decay much during the recording of new holograms and, second, multiplexed holograms of larger diffraction efficiency can be fixed in a crystal, which was partially depoled by a prior fixing negative voltage pulse [17]. In general, the fixed holograms with smaller spatial period are less stable and are subject to stronger decay [18]. The equilibrium (or quasi-equilibrium with a long lifetime) value of fixed hologram efficiency is largely dictated by the microdomains thermodynamic stability and dynamics, as well as the degree of polarization of the crystal [17]. Studies [19] revealed the effect of the threshold and saturation in fixed HDE with respect to the fixing pulse amplitude. If the amplitude of the negative voltage pulse exceeds the coercive field of the sample, the fixed holograms are very weak due to the strong depolarization of the ferroelectric crystal. However, at the same time the strength of the revealed grating is almost equal to the magnitude of the initial electronic hologram.

3.3 Dynamic photorefractive compensation of fixed polarization and ionic holograms (theory)

In this section we introduce a model that describes the formation of a photorefractive grating in the presence of photorefractively inactive space-charge (e.g., ionic) or ferroelectric polarization modulation. In general, fixing methods demonstrated in different photorefractive crystals [1-12] create an optically unerasable charge or polarization distribution. The model predicts how the fixed grating affects the formation of the ordinary photorefractive grating and also leads to a spatially nonuniform mobile and trapped charge distributions even in the presence of a homogeneous illumination. The predictions of the model are further applied to the interpretation of the experimental results [6,15] on electrical fixing of holograms in $Sr_{0.75}Ba_{0.25}Nb_2O_6$.

The dynamic behavior of the photorefractive effect is described by the following set of nonlinear coupled equations [20]. We neglect the contribution of the photovoltaic effect and assume that only one type of carrier is involved:

$$\frac{\partial N_D^+}{\partial t} = (\alpha I_0+\beta)(N_D-N_D^+)-\gamma_e n_e N_D^+ , \qquad 3.1$$

$$j_e = e\mu n_e E + k_b T \mu \nabla n_e , \qquad 3.2$$

$$\frac{\partial n_e}{\partial t} = \frac{\partial N_D^+}{\partial t} + \frac{1}{e}\nabla j_e , \qquad 3.3$$

$$\nabla(P_s + \varepsilon\varepsilon_0 E) = e\left(N_D^+ - n_e - N_A + \frac{\rho_{fix}}{e}\right), \qquad 3.4$$

where N_D^+ is ionized donors concentration, n_e the free electron concentration, N_a the acceptor concentration, μ the carrier mobility, γ_e the recombination constant, P_s the

spontaneous polarization, and E the electric field. We consider a sinusoidal fixed charge distribution:

$$\rho_{fix} = \rho_{fix_1} \exp(iKx), \qquad 3.5$$

and spatially uniform light illumination I_0. Following the usual linearization procedure and assuming that $\rho_{fix} << eN_a$, the quantities N_D^+, n_e, E, and j_e can be approximated by a sinusoidal form: $F(x)=F_0 +F_1\exp(iKx)$. Assuming that P_s is uniform, the steady state solution of the Eqs. 3.1-3.4 for the space-charge field or and the ionized donors density modulation is given by

$$E_1 = \frac{\rho_{fix_1}}{iK\varepsilon\varepsilon_0} \frac{E_d - iE_0}{E_d + E_q - iE_0}, \qquad 3.6$$

$$N_{D_1}^+ = -\frac{\rho_{fix_1}}{e} \frac{E_q}{E_d + E_q - iE_0}, \qquad 3.7$$

where $E_d=Kk_bT/e$ - diffusion field, $E_q = N_E e/\varepsilon\varepsilon_0 K$ is the limiting space-charge field, and E_0 the externally applied field. The time constant with which the field E_1 is formed is equal to the conventional grating formation time constant with the same average intensity and spatial frequency, formed in the absence of the fixed grating [21]. This is because the fixed grating acts as an inhomogeneous term for the system of linearized Eqs. 3.1-3.4 replacing the sinusoidal intensity illumination; the coefficients of the set of linear equation remain unchanged, and hence the time constant is the same.

The total space-charge field [Eq. 3.6] may be decomposed into a sum of a field $\rho_{fix_1}/iK\varepsilon\varepsilon_0$ induced by fixed, nonphotorefractive charges and a compensating field E_1^{comp} formed by redistributed charge carriers described by $N_{D_1}^+$. Namely,

$$E_1^{comp} = \frac{eN_{D_1}^+}{iK\varepsilon\varepsilon_0} = -\frac{\rho_{fix_1}}{iK\varepsilon\varepsilon_0}\frac{E_q}{E_d + E_q - iE_0}. \qquad 3.8$$

Note that due to the finite dark conductivity, compensation of the fixed grating by dynamic electronic space-charge takes place even without any external illumination.

Our description so far assumed a fixed grating due to an ionic grating. Similar analysis may be applied to the case where the fixed grating is produced by a spatial variation of the ferroelectric spontaneous polarization. A spatial variation of spontaneous polarization is formally equivalent to a fixed space-charge [22] according to: $\rho_{ind} = -\nabla P_s$. Then, assuming a sinusoidal modulation of spontaneous polarization:

$$P_s = P_{s_0} + P_{s_1}\exp(iKx), \qquad 3.9$$

equation 3.4 takes the form

$$\frac{\partial E}{\partial x} = \frac{e}{\varepsilon\varepsilon_0}\left(N_D^+ - n_e - N_A - \frac{1}{e}\frac{\partial P_s}{\partial x}\right), \qquad 3.10$$

or, in linearized form, for the case $E_0=0$:

$$iKE_1 = \frac{e}{\varepsilon\varepsilon_0}\left(N_{D_1}^+ - n_{e_1} - \frac{iK}{e}P_{s_1}\right), \qquad 3.11$$

where ε is the mean value of dc dielectric constant. The value of the total space-charge field E_1 and of the compensating electronic component E_1^{comp} are given by

$$E_1 = -\frac{P_{s_1}}{\varepsilon\varepsilon_0}\frac{E_d}{E_d + E_q} = -\frac{P_{s_1}}{\varepsilon\varepsilon_0}\frac{1}{1 + (\Lambda/\Lambda_e)^2}, \qquad 3.12$$

$$E_1^{comp} = \frac{P_{s1}}{\varepsilon\varepsilon_0}\frac{E_q}{E_d + E_q} = \frac{P_{s1}}{\varepsilon\varepsilon_0}\frac{(\Lambda/\Lambda_e)^2}{1+(\Lambda/\Lambda_e)^2}, \qquad 3.13$$

where $\Lambda=2\pi/K$ is the grating spacing and $\Lambda_e = 2\pi\sqrt{\varepsilon\varepsilon_0 k_b T / e^2 N_E}$ is the Debye length.

The perturbation of the refractive index arises through the ordinary linear electrooptic effect due to the total space-charge field E_1. Even though it is more correct to describe the refractive index variation in terms of polarization rather than electric field [23], both approaches lead to the same result and, in this sense, are equivalent. The modulation in spontaneous polarization also causes spatial variations of the linear electrooptic coefficient and the dc dielectric constant. However, for the case of zero applied field considered here these terms contribute only to the higher spatial orders of the index of refraction variation. Therefore, they do not affect the fundamental K-space harmonic of the electric field that is responsible for the formation of the hologram.

In the case of fixing via ionic compensation the amplitude of the compensating electronic grating is difficult to measure independently, since the thermal erasure of the ionic grating also perturbs the electronic pattern. Electrical fixing that involves ferroelectric polarization, on the other hand, enables one to perform direct observations and measurements of the dynamic compensating grating, since the polarization pattern can be erased simply by applying a strong positive electric field along the direction of spontaneous polarization of the photorefractive crystal [5,6]. The latter process does not affect the compensating field E_1^{comp}, whose strength can then be determined by measuring the diffraction efficiency of the residual revealed hologram.

3.4 Dynamic photorefractive compensation of fixed polarization (domain) holograms in SBN:75 (experiment)

We studied experimentally the process of fixing and compensation of phase holograms in photorefractive $Sr_{0.75}Ba_{0.25}Nb_2O_6$. Electrical fixing was achieved by applying a negative voltage pulse along the crystal *c*-axis after recording a space-charge grating with two input beams. To avoid beam coupling during recording and reconstruction, the ordinarily polarized beams were used and the holographic diffraction efficiency (HDE) was monitored by an extraordinarily polarized low-power He-Ne laser beam Bragg matched to the initial hologram (Fig. 3.1). Low intensity (4 mW/cm^2) recording beams were used in order to avoid the photoassisted domain reversal during the recording stage [9,10] and the effects associated with the light-induced absorption in photorefractive SBN [24]. Low intensity recording also minimizes the heating of the sample by the writing beams and, therefore, reduces substantially the pyroelectric and thermal gratings [25] in the volume of the crystal. After each fixing experiment the crystal is poled by applying positive voltage (~5 kV/cm) along the *c*-axis for 20-30 minutes at room temperature. A typical cycle of recording, fixation, optical and electrical erasure is shown on Fig. 3.7. After the fixed hologram reaches steady state under illumination by a non-Bragg-matched erasing beam, a strong positive voltage pulse is applied erasing the polarization grating. The residual revealed hologram corresponds to the electronic compensating grating, which is measured by recording the power of light diffracted off it. Figure 3.8 shows the dependence of the steady-state values of the fixed HDE and the compensating revealed grating HDE on the grating spacing Λ. In agreement with the model proposed the amplitude of the electronic compensating grating [Eq. 3.13] dramatically increases with the grating spacing.

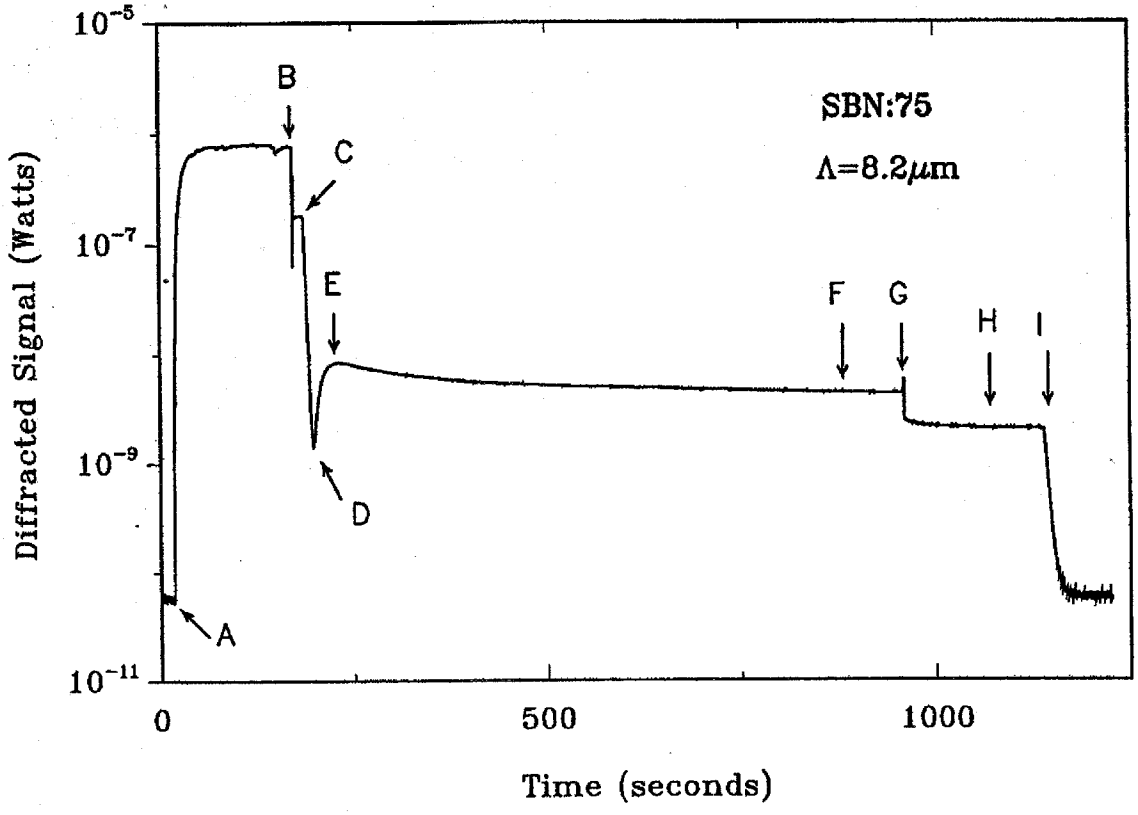

Figure 3.7. Diffracted signal as a function of time during the fixing experiment. Fixing pulse amplitude is -1650 V/cm and its duration 0.5 s. Total intensity of the recording beams is 4 mW/cm^2, λ=488 nm, intensities ratio m≈1. The transmitted probe light power without the grating is 2.3 μW. A: Recording begins. B: Writing beams are blocked and a negative voltage pulse is applied. C: Optical erasure with a non-Bragg-matched beam (I = 8 mW/cm^2) begins. D: The transient dip due to 180° phase shift between the polarization and the electronic gratings. E: Peak in HDE of the fixed grating; slow decay of fixed grating begins. F: Steady state of the fixed grating. G: Positive voltage pulse (E=4.2 kV/cm, duration 2 s) is applied (erasing beam is blocked). H: Revealed compensating grating. I: Optical erasure.

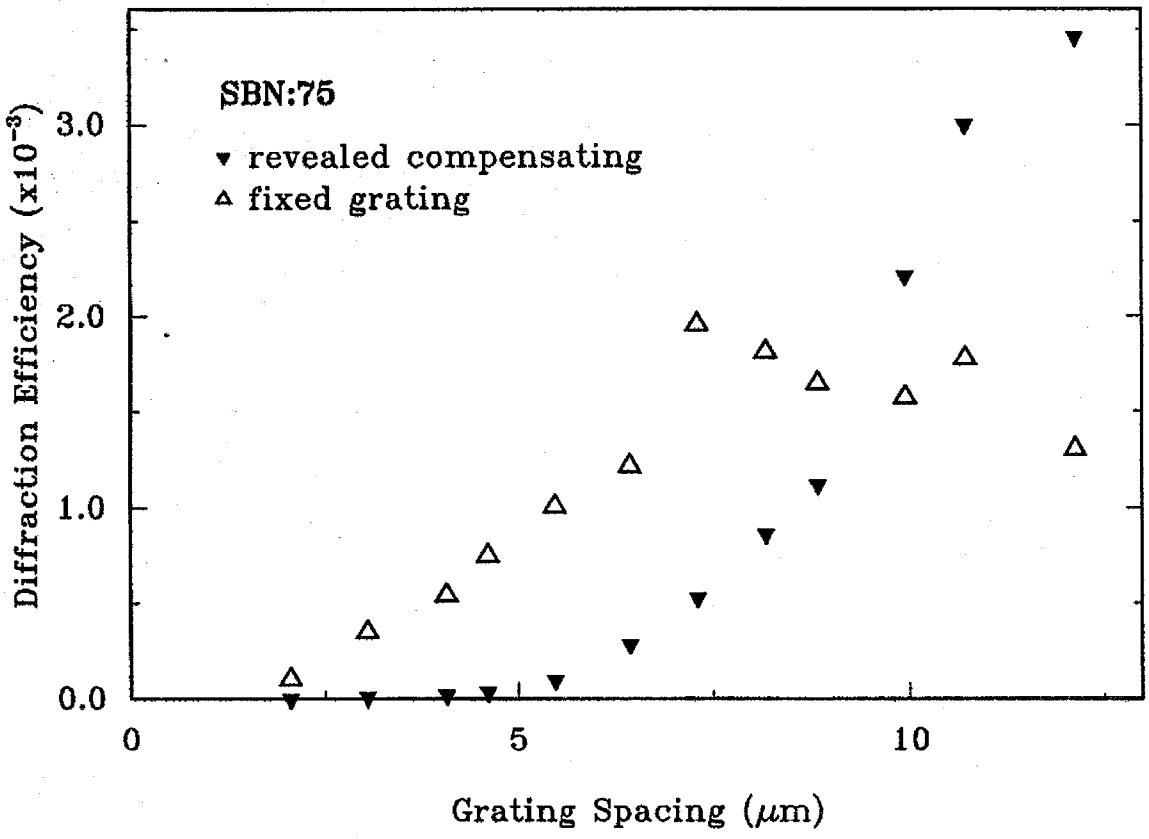

Figure 3.8. Diffraction efficiencies of fixed (steady state) and electrically revealed compensating gratings as a function of Λ. The same experimental parameters were used as in Figure 3.7.

Since in our experiments the effects associated with beam coupling (i.e., longitudinal change of the modulation index of the hologram, self-depletion, or self-enhancement) were carefully eliminated, the diffraction efficiency, in the limit of negligible absorption and small index variation, may be expressed as

$$\eta \equiv \left(\frac{\pi d|\Delta n_1|}{\lambda \cos\theta}\right)^2 \propto r_{eff}^2 E_1^2, \qquad 3.14$$

where d is the crystal thickness, θ is the Bragg angle inside the crystal, r_{eff} is the effective linear electrooptic coefficient, and E_1 is the internal space-charge field variation. Then, according to Eqs. 3.12 and 3.13, independent of the actual value of the polarization modulation, the ratio of HDEs of the fixed and compensating (or "revealed") gratings should obey the following relationship:

$$\ln\left(\frac{\eta^{comp}}{\eta^{fix}}\right) = 4\ln\left(\frac{\Lambda}{\Lambda_e}\right) + 2\ln\left(\frac{r_{eff}^{0}}{r_{eff}^{*}}\right), \qquad 3.15$$

where r_{eff}^{*} is the effective electrooptic coefficient of the partially depoled crystal after a negative depoling voltage is applied. The strong positive pulse that is applied to erase the polarization grating and to reveal the compensating grating also poles the crystal and, consequently, the electrooptic coefficient takes its original value r_{eff}^{0}. The experimental data shown in Figure 3.9 indicate a linear relationship between $\ln\left(\eta^{comp}/\eta^{fix}\right)$ and $\ln(\Lambda)$ with slope 4.2±0.2 which is in a good agreement with the value 4, predicted by the theory [Eq. 3.15]. We should point out that since we do not know the dependence of P_{s_1} with Λ, the fact that the ratio plotted in Fig. 3.9 is independent of P_{s_1} makes possible the comparison between theory and experiment. The ratio of the HDEs of the compensating and fixed gratings is the same for both an ionic or a polarization fixed grating. However, the fact that we could observe an optically erasable revealed compensation grating by electrically erasing the fixed grating strongly supports the hypothesis that the fixing was due to polarization switching in the $Sr_{0.75}Ba_{0.25}Nb_2O_6$ fixing experiment [5,6]. The maximum modulation depth of the spontaneous polarization, corresponding to the maximum fixed grating HDE, was evaluated to be equal to $\Delta P_s \cong 10^{-4}\ P_s$, where $P_s = 8.1\ \mu C/cm^2$ is the spontaneous polarization of the completely poled $Sr_{0.75}Ba_{0.25}Nb_2O_6$ crystal at room temperature [5]. This small modulation depth is responsible for the low HDE of the fixed holograms.

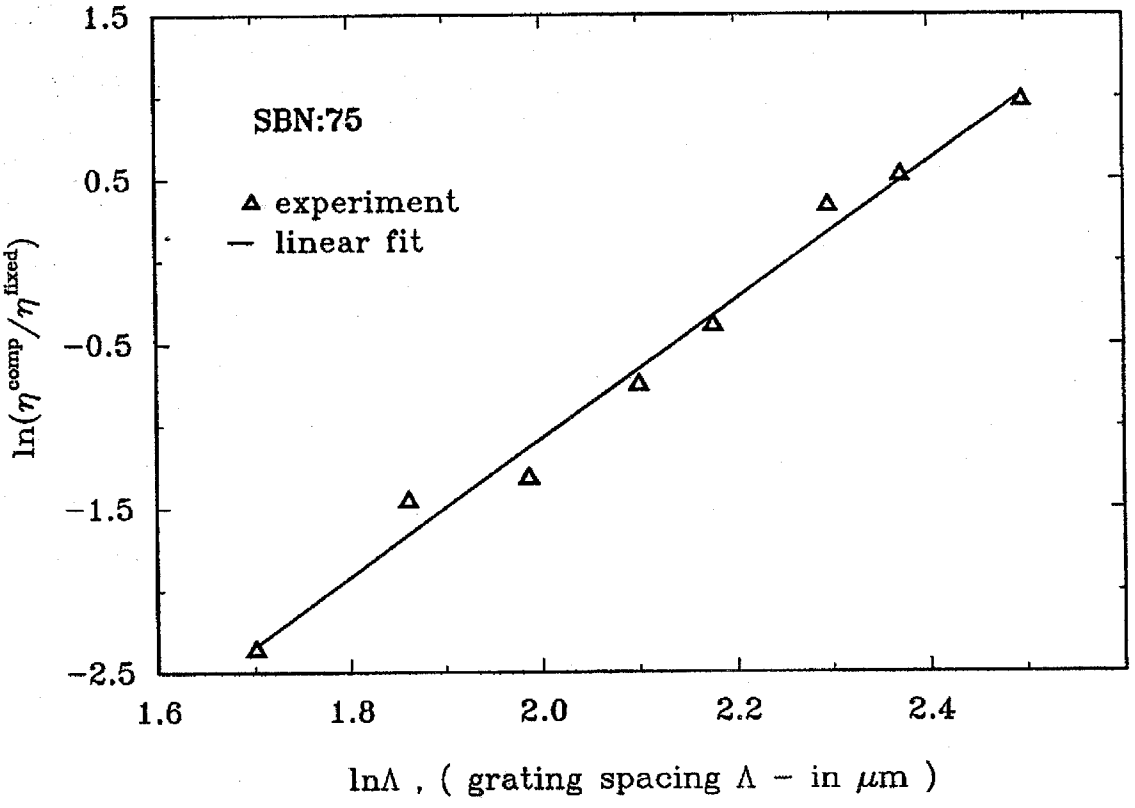

Figure 3.9. Log-log plot of the ratio of holographic diffraction efficiencies of the revealed compensating grating and the fixed grating vs. grating spacing. Points obtained for $\Lambda < 5.5$ μm are not included since the diffracted signal off the revealed holograms was less than the noise level. The linear fit has the slope 4.2±0.2 which is in a good agreement with the theoretically predicted value 4.0.

3.5 Summary

Photorefractive holograms stored in $Sr_{0.75}Ba_{0.25}Nb_2O_6$ are electrically fixed at room temperature. The fixed holograms can be read out directly or after a positive poling voltage pulse is applied that can dramatically enhance the diffraction efficiency. The latter process destroys the polarization component of the hologram, but it can be restored later via subsequent application of the negative electric field pulse. Single gratings as well as images are recorded, fixed, and faithfully reproduced.

Fixed polarization or ionic gratings are screening upon readout by dynamic photorefractive space charge of trapped electrons. The degree of electronic screening depends dramatically on the spatial frequency of the fixed hologram. We introduced a model for the formation of photorefractive grating in the presence of optically inactive, fixed charge, or polarization modulation. Application of this model to electrical fixing in $Sr_{0.75}Ba_{0.25}Nb_2O_6$ gives good agreement between experimental observations and theoretical predictions.

References for Chapter Three

[1] J. J. Amodei and D. L. Staebler, Appl. Phys. Lett. **18**, 540 (1971).

[2] L. Arizmendi, J. Appl. Phys. **65**, 423 (1989).

[3] G. Montemezzani and P. Gunter, J. Opt. Soc. Am. B **7**, 2323 (1990).

[4] D. Kirillov and J. Feinberg, Opt. Lett. **16**,1520 (1991).

[5] F. Micheron and G. Bismuth, Appl. Phys. Lett. **23**, 71 (1973).

[6] Y. Qiao, S. Orlov, D. Psaltis, and R. Neurgaonkar, Opt. Lett. **18**, 1004 (1993).

[7] F. Micheron and G. Bismuth, Appl. Phys. Lett. **20**, 79 (1972).

[8] F. Micheron and J. Trotier, Ferroelectrics **8**, 441 (1974).

[9] J. B. Thaxter and M. Kestigian, Appl. Opt. **13**, 913 (1974).

[10] A. Kewitsch, M. Segev, A. Yariv, and R. Neurgaonkar, Opt. Lett. **18**, 1262 (1993).

[11] M. Horowitz, A. Bekker, and B. Fischer, Appl. Phys. Lett. **62**, 2619 (1993).

[12] V. Leyva, A. Agranat, and A. Yariv, Opt. Lett. **16**, 554 (1991).

[13] J. Ma, T. Chang, J. Hong, R. Neurgaonkar, G. Barbastathis, and D. Psaltis, "Electrical fixing of 1000 angle-multiplexed holograms in SBN:75," in IEEE'96 Nonlinear Optics, Fundamentals and Applications, Maui, Hawaii (1996).

[14] G. S. Trofimov and S. I. Stepanov, Sov. Tech. Phys. Lett. **10**, 282 (1984).

[15] S. Orlov, D. Psaltis, and R. R. Neurgaonkar, "Dynamic electronic compensation of fixed gratings in photorefractive media," Appl. Phys. Lett. **63**, 2466 (1993).

[16] J. P. Wilde and L. Hesselink, Opt. Lett. **17**, 853 (1992).

[17] R. S. Cudney, J. Fousek, M. Zgonik, P. Günter, M. H. Garrett, and D. Rytz, Phys. Rev. Lett. **72**, 3883 (1994).

[18] S. Orlov, D. Psaltis, and R. Neurgaonkar, Appl. Phys. Lett. **64**, 824 (1994).

[19] Y. Qiao, S. Orlov, G. Barbastathis, and D. Psaltis, OSA Annual Meeting'93, in *Technical Digest* **16**, 78 (1993)

[20] N. Kukhtarev, V. Markov, S. Odoulov, M. Soskin, and V. Vinetskii, Ferroelectrics **22**, 949 (1979).

[21] G. C. Valley and J. F. Lam, in *Photorefractive Materials and Their Applications I*, edited by P. Gunter and J. P. Huignard (Springer, Berlin, 1988), Chap. 3.

[22] L. D. Landau and E. M. Lifshitz, *Electrodynamics of Continuous Media* (Addison-Wesley, Reading, MA, 1960), Chap. 2.

[23] W. D. Johnston, Jr., J. Appl. Phys. **41**, 3279 (1970).

[24] S. Orlov, M. Segev, A. Yariv, and R. Neurgaonkar, Opt. Lett. **19**, 578 (1994).

[25] K. Buse, J. Opt. Soc. Am. B **10**, 1266 (1993).

Chapter Four

Holographic Storage Dynamics in Lithium Niobate: Theory and Experiment

4.1 Introduction

Holographic data storage in photorefractive crystals is a topic of intense current interest [1-3]. It is driven by the prospects of the large storage capacity $\sim V/\lambda^3$ bits in a volume V. Two of the important concerns in this field involve the lifetimes of fixed and developed holograms and their strength. The volume phase holograms in photorefractive materials are produced by the redistribution of photoexcited carriers (e.g., electrons) in the presence of light. To avoid fast erasure of the holograms upon readout several techniques have been developed in the past [4 - 7]. In general the efficient ionic fixing is based on the great disparity between the dark electronic conductivity at elevated temperatures and the ionic conductivity. At elevated temperature the ionic conductivity is dominant and ions readily compensate the holographic electric field pattern created by photoexcited electrons by mimicking their spatial distribution. At low temperature the ionic conductivity is very low enabling the quasi-permanent storage of the ionic replica of the initial electronic hologram.

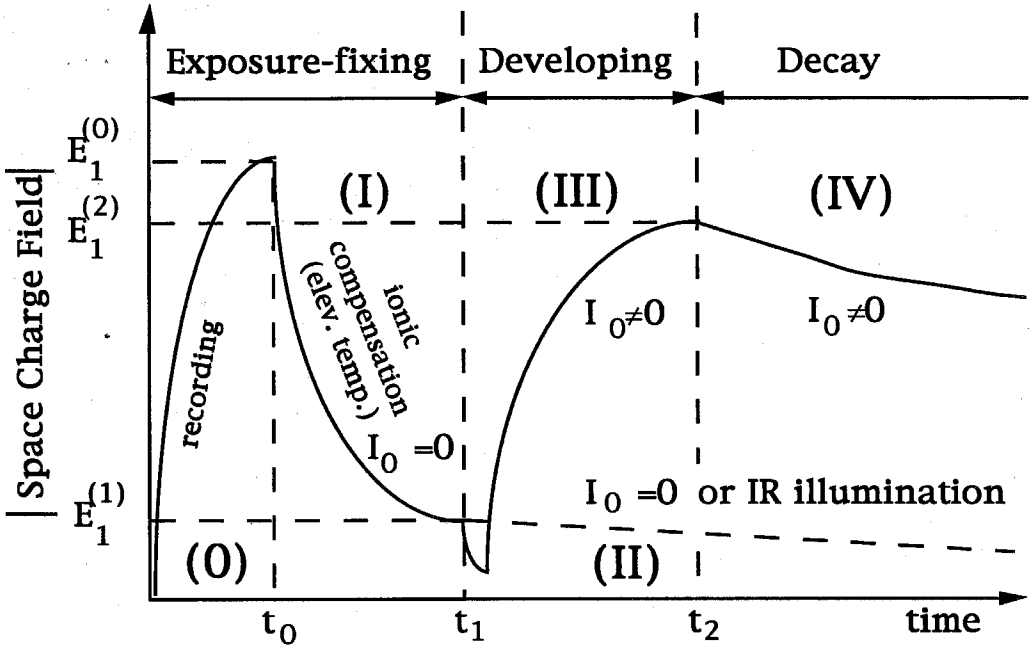

Figure 4.1. A typical life history of a hologram in photorefractive materials.

The residual ionic conductivity at low temperature thus determines the lifetime of the *fixed* hologram.

A typical history of a hologram is sketched in Figure 4.1. In phase I an electronic grating, previously recorded, is heated up to cause ionic transport. This leads to a compensated grating which is represented by the net space charge field amplitude) $E_1^{(1)}$. In phase II the grating is left in the dark or is exposed to infrared light which is not photoactive. This stage corresponds to a slow dark decay of both the electronic grating and the ionic compensating grating which adiabatically follows the former. In many applications, however, the hologram is exposed to a "reading" light as in phase III. This light causes a partial redistribution of the trapped electrons culminating in a quasi-stable

field $E_1^{(2)}$. This field will proceed to decay to zero under illumination due to ionic transport (phase IV).

The problem of grating dynamics has been considered extensively [8-14]. What differentiates our work is the fact that, by taking advantage of the great disparity between the transport time constants which are involved in typical crystals, especially $LiNbO_3$, we are able to obtain simple analytic expressions [9] for the time dependent field in each of the above defined phases under realistic scenarios.

4.2 Two-species conduction formulation

In the model we consider both the conduction of the optically excited electrons and the ionic transport, as well as the thermally activated dark electronic conductivity. Free conduction band electrons can be excited optically or thermally from a single-donor level, while ionic species are subject to drift due to the internal space charge fields and diffusion due to their own density gradients. We fully account for the photovoltaic currents, both dc and spatially inhomogeneous.

The dynamic variables are the mobile electron density n_e, the ion density n_i and the trapped charge (ionized donor) density N_d^+. The complete set of transport equations first formulated by Kukhtarev [15] is

$$\frac{\partial N_d^+}{\partial t} = (\sigma/h\nu I_0 + \beta)(N_d - N_d^+) - \gamma_e N_d^+ n_e , \qquad 4.1$$

$$\frac{\partial n_e}{\partial t} = \frac{\partial N_d^+}{\partial t} + \frac{1}{e}\frac{\partial}{\partial x}\left(e\mu_e n_e E + eD_e\frac{\partial n_e}{\partial x} + \kappa\sigma I_0(N_d - N_d^+)\right), \qquad 4.2$$

$$\frac{\partial n_i}{\partial t} = -\frac{1}{e}\frac{\partial}{\partial x}\left(e\,\mu_i\, n_i\, E - eD_i\frac{\partial n_i}{\partial x}\right), \qquad 4.3$$

$$\varepsilon\varepsilon_0\frac{\partial E}{\partial x} = e\left(N_d^+ - N_a + n_i - n_{i0} - n_e\right). \qquad 4.4$$

In the equations 4.1-4.4 I_0 is the average optical intensity, σN_d^0 is the optical intensity absorption coefficient, β is the thermal excitation rate, and γ_e is the recombination constant for electrons. μ_e and μ_i are the mobilities of the electrons and ions respectively and we assumed $D/\mu = k_bT/e$, where k_b is the Boltzman constant. κ is the photovoltaic coefficient. The density of neutral donors is N_d^0. Total donor density is $N_d = N_d^0 + N_d^+$, and $N_{d0}^+ = N_a$ is the density of deep traps. The total current is equal to the sum of the ionic and electronic currents and that is due to the photovoltaic effect.

The equations 4.1-4.4 are linearized by approximating the dynamic variables in terms of (time and space) averages and small signal time varying amplitudes, i.e.,

$$n_e = n_{e0} + \left(n_{e1}e^{-iKx} + c.c.\right), \qquad 4.5$$

$$N_d^+ = N_a + \left(N_{d1}^+ e^{-iKx} + c.c.\right), \qquad 4.6$$

$$n_i = n_{i0} + \left(n_{i1}e^{-iKx} + c.c.\right), \qquad 4.7$$

where $n_{e1} << n_{eo}$, etc., K is the spatial frequency of the grating and x is the spatial coordinate. A dependent variable is the space charge field

$$E = E_0 + \left(E_1\, e^{-iKx} + c.c.\right). \qquad 4.8$$

Using the above definitions the transport equations 4.1-4.4 can be reduced to the following linearized form

$$\frac{\partial N_{d1}^{+}}{\partial t} = -(\sigma/h\nu I_0 + \beta)\frac{N_d}{N_a} N_{d1}^{+} - \gamma_e N_a n_{e1}\,, \tag{4.9}$$

$$\frac{\partial n_{e1}}{\partial t} = \left(-(\sigma/h\nu I_0 + \beta)\frac{N_d}{N_a} + \frac{\mu_e n_{e0} e}{\varepsilon} + i\frac{\kappa\sigma I_o K}{e}\right) N_{d1}^{+} - \left(\gamma_e N_a + \frac{\mu_e n_{e0} e}{\varepsilon} + D_e K^2 + i\mu_e K E_0\right) n_{e1} + \frac{\mu_e n_{e0} e}{\varepsilon} n_{i1}\,, \tag{4.10}$$

$$\frac{\partial n_{i1}}{\partial t} = -\left(\frac{\mu_i n_{io} e}{\varepsilon} + D_i K^2 + i\mu_i K E_o\right) n_{i1} + \frac{\mu_i n_{io} e}{\varepsilon}\left(n_{e1} - N_{d1}^{+}\right), \tag{4.11}$$

$$E_1 = \frac{ie}{\varepsilon K}\left(N_{d1}^{+} + n_{i1} - n_{e1}\right), \tag{4.12}$$

with the last equation following from the Gauss law.

A major feature of our analysis is the inequality $n_{e1} << N_{d1}^{+}$, n_{i1} so that n_{e1} can be neglected in equations 4.11 and 4.12, but not otherwise. This inequality results from the fact that the electron trapping rate $\gamma_e N_a \sim 10^7 - 10^9\ s^{-1}$ exceeds by many orders of magnitude any other rate. This causes the electrons to reach an essentially instantaneous (i.e., within $t \leq 10^{-7}$ s) local equilibrium with N_{d1}^{+} and n_{i1}. The equilibrium value of n_{e1} is obtained by setting the left side of equation 4.10 equal to zero. This enables us to eliminate n_{e1} from the mathematics (but not from the physics) and rewrite the governing equations of grating dynamics 4.9-4.12 in terms of two dynamic variables, i.e., n_{i1} and N_{d1}^{+}, only:

$$\frac{\partial N_{d1}^{+}}{\partial t} = -N_{d1}^{+}\frac{\omega_e\gamma_e N_a + \left(\frac{\sigma}{h\nu}I_0 + \beta\right)\frac{N_d}{N_a}\left(D_e K^2 - i\mu_e K E_0\right) - iK\kappa\frac{\sigma}{h\nu} I_o \gamma_e N_a}{\gamma_e N_a + D_e K^2 - i\mu_e K E_0} - n_{i1}\frac{\omega_e\gamma_e N_a}{\gamma_e N_a + D_e K^2 - i\mu_e K E_0}\,, \tag{4.13}$$

$$\frac{\partial n_{i1}}{\partial t} = -\, n_{i1}\left(\omega_i + D_i K^2 + i\,\mu_i K E_0\right) - N_{d1}^{+}\,\omega_i\,, \tag{4.14}$$

$$E_1 = \frac{ie}{\varepsilon K}\left(N_{d1}^{+} + n_{i1}\right), \tag{4.15}$$

where

$$\omega_e \equiv \frac{e\mu_e\, n_{e0}}{\varepsilon} = \frac{e\mu_e\left(\dfrac{\sigma}{h\nu}I_0 + \beta\right)(N_d - N_a)}{\varepsilon\,\gamma_e N_a}\,, \tag{4.16}$$

is the dielectric relaxation rate for conduction band electrons, and

$$\omega_i \equiv \frac{e\mu_i\, n_{i0}}{\varepsilon}\,, \tag{4.17}$$

is the dielectric relaxation frequency for conducting ions.

In what follows we consider the solutions of equations 4.13, 4.14 and 4.15 in each of the phases of Figure 4.1.

4.3 Compensation of electronic space charge by ionic transport (phase I)

In this stage a pre-recorded electronic N_{d1}^{+} grating is compensated in the dark by mobile ionic species. Typically, this takes place at elevated temperature where (e.g., in lithium niobate) the ionic conductivity is substantially larger than the electronic conduction associated with thermal detrapping. Therefore, the N_{d1}^{+} modulation can be assumed essentially constant throughout this stage. The space charge field decays to its equilibrium value as given by

$$E_1^{(I)}(t) = E_1^{(0)}(0)\left[\frac{D_i K^2 + iK\mu_i E_0}{\omega_i + D_i K^2 + iK\mu_i E_0} + \frac{\omega_i}{\omega_i + D_i K^2 + iK\mu_i E_0} e^{-(\omega_i + D_i K^2 + iK\mu_i E_0)t}\right], \quad 4.18$$

where $E_1^{(0)}(0)$ is the space charge field of the initially recorded (phase 0 in Figure 4.1) electronic grating. The relaxation time constant describing this phase is

$$\tau_I = (\omega_i + D_i K^2 + iK\mu_i E_0)^{-1}. \quad 4.19$$

Due to the diffusion of ions and their finite density the ionic compensation of the electronic space charge is never complete, i.e. there remains, in the steady state, a residual stabilized electric field $E_1^{(1)}$. Equation 4.18 predicts that at the end of phase I the value of this steady-state stabilized field is

$$E_1^{(1)} = \frac{D_i K^2 + iK\mu_i E_0}{\omega_i + D_i K^2 + iK\mu_i E_0} E_1^{(0)}. \quad 4.20$$

In data storage applications the aim of this stage is to culminate in as perfect a compensation as possible, i.e., $n_{i1}(t_1) \approx -N_{d1}^{+}(t_0)$ or, equivalently $E_1^{(1)} << E_1^{(0)}$. For the most practical case of zero applied field this requires, according to equation 4.20, that $\omega_i >> D_i K^2$ or, equivalently

$$n_{i0} >> \frac{\varepsilon k_b T K^2}{e^2}. \quad 4.21$$

This condition sets the *lower* boundary for the optimized density of the free ions in a crystal used for holographic data storage. Further increase of n_{i0} does not improve the fixing efficiency but decreases the possible storage time since the ionic relaxation frequency ω_i is proportional to n_{i0} at any temperature. The minimal density of free ions needed for perfect compensation in $LiNbO_3$ is thus $n_{i0} >> 5\times10^{16}$ cm^{-3} (for the grating spacing

$2\pi/K = 1\ \mu m$). Typical H^+ impurity density in these crystals [16] is about $10^{18}\ cm^{-3}$ and therefore the ionic compensation is always very strong even if we assume that the only ionic species responsible for hologram fixing is hydrogen.

The above results apply in their basic features, also to the case where the recording phase 0 and the ionic compensation phase I are simultaneous. If the ionic compensation takes place in the presence of light under open circuit conditions, then $E_0 = -E_{p.v.} = -\kappa\gamma_e N_a/e\mu_e$.

4.4 Electronic decay in the dark (phase II)

This phase consists of a slow decay in the dark of the ionically compensated electronic grating, the end product of phase I. This decay is due to thermally excited electrons which proceed to drift and diffuse, thus, reducing the strength of the hologram $E_1^{(1)}$. The ionic grating adiabatically follows the decaying electronic hologram due to the much faster (at elevated temperature [4]), adjustment by transport of ions so that at any moment the dynamic equilibrium between the ionic and the electronic gratings is preserved

$$\frac{n_{i1}}{N_{d1}^+} = -\frac{\omega_i}{\omega_i + D_i K^2} . \qquad 4.22$$

This relation follows from equation 4.14 when we take $\partial n_{i1}/\partial t = 0$ and assume a zero dc field ($E_0 = 0$). By substituting 4.22 into equations 4.13 and 4.15 we find that the total space charge field (i.e., grating amplitude) decays as

$$E_1^{(II)}(t) = \frac{ie}{\varepsilon K}\left(N_{d1}^+(t) + n_{i1}(t)\right) = E_1^{(0)}\frac{D_i K^2}{\omega_i + D_i K^2}\, e^{-\omega_e\left(\frac{D_i K^2}{D_i K^2 + \omega_i} + K^2 d^2\right)t} , \qquad 4.23$$

and

$$\omega_e = \frac{e\mu_e \beta(N_d - N_a)}{\varepsilon \gamma_e N_a} \qquad d^2 \equiv \frac{N_d kT\,\varepsilon}{N_a (N_d - N_a)\, e^2}, \tag{4.24}$$

where d is the electronic Debye screening length due to ionized donors.

The decay rate

$$\omega_{decay}^{(II)} = \omega_e \left[\frac{D_i K^2}{\omega_i + D_i K^2} + K^2 d^2 \right] \tag{4.25}$$

is proportional to the electronic dielectric relaxation frequency ω_e (at $I_0 = 0$) multiplied by the ionic screening factor plus a term due to diffusion of electrons. The electronic decay in the dark, therefore, is slowed down in the presence of large ionic conductivity. The residual electronic dark decay is primarily due to the diffusion (term proportional to K^2d^2 in equation 4.25) rather than drift in the hologram electric field, since the letter is strongly reduced due to the conducting ions (see equations 4.20 and 4.23). Furthermore, in the usual case of strong ionic compensation, the dark decay rate is always proportional to the square of the spatial frequency K *without* saturation at small K. This is different from the unscreened case when no ions are present and $\omega_{decay} \rightarrow \omega_e$ for sufficiently small K, $K^2d^2 \ll 1$. The above results are derived for the most typical case of zero applied field. If the electronic dark decay takes place under externally applied field E_0 the equations 4.23-4.25 are modified as follows

$$\frac{n_{i1}}{N_{d1}^+} = - \frac{\omega_i}{\omega_i + D_i K^2 + iK\mu_i E_0}, \tag{4.26}$$

$$E_1^{(II)}(t) = E_1^{(0)} \frac{D_i K^2 + iK\mu_i E_0}{\omega_i + D_i K^2 + iK\mu_i E_0} e^{-\omega_e \left(\frac{D_i K^2 + iK\mu_i E_0}{\omega_i + D_i K^2 + iK\mu_i E_0} + K^2 d^2 + iK\mu_e E_0 \right) t}, \quad 4.27$$

$$\omega_{decay}^{(II)} = \omega_e \left[\frac{D_i K^2 + iK\mu_i E_0}{\omega_i + D_i K^2 + iK\mu_i E_0} + K^2 d^2 + iK\mu_e E_0 \right], \quad 4.28$$

Experimental data reproduced in Figure 4.2 show the dark decay of holographic gratings recorded in Fe:$LiNbO_3$ at elevated temperature. Two distinct stages of the process (fast and slow) can be identified as fast ionic compensation (phase I) and the much slower thermal decay of the electronic grating screened by the mobile ions (phase II) [9].

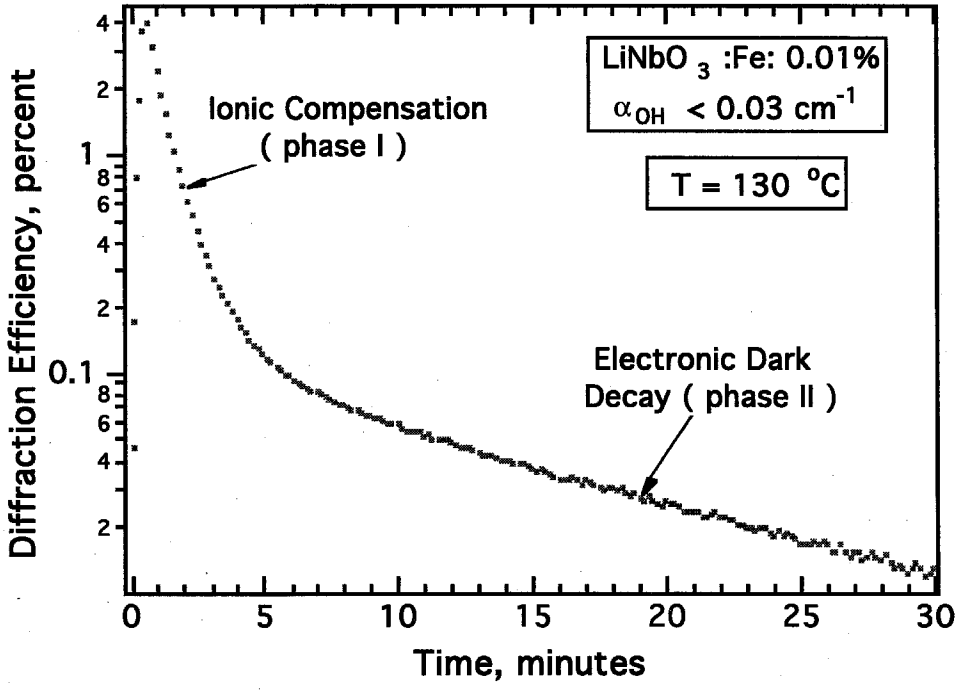

Figure 4.2. Diffraction efficiency vs. time for a hologram recorded and stored in Fe-doped $LiNbO_3$ (partially reduced) at 130°C. The grating spacing is $2\pi/K$ = 1.15 μm. Two stages of the dark decay can be identified as ionic compensation (fast stage of the decay, phase I) and a much slower decay due to conduction by the thermally excited electrons (phase II).

4.5 Developing or readout (phase III)

This stage consists of the developing (revealing) of the compensated grating by continuous illumination ($I_0 \neq 0$), typically at or near room temperature. This phase also describes what happens when we read the hologram. This causes an increase in the electronic conductivity so that it greatly exceeds that of the ions $(\sigma_e >> \sigma_i)$. The mobile electrons diffuse and drift in the electric field induced by semi-permanent ionic charge distribution. Therefore, even under spatially homogeneous illumination I_0 the equilibrium trapped electrons distribution N_{d1}^{+} is not uniform, but rather screens the "fixed" ionic pattern [9,10]. The degree of this electronic screening is greatly dependent on the amount of available traps N_e, the grating spatial frequency K, and the strength of the photovoltaic effect [9]. The treatment of the photovoltaic effect in this stage makes it necessary to distinguish two different types of boundary condition imposed on the electron current density and the total electric space-charge field. Besides, since the electronic conductivity is dominant in this phase we can consider the ions as stationary and derive the expressions for the transient hologram electric field upon light read-out.

(a) Short Circuit

Under the short-circuit conditions $E_0 = 0$ and we allow for the full dc photovoltaic current $\kappa\alpha I_0(N_d - N_a)$ to flow. The resulting space charge holographic field during the phase III is

$$E_1^{(III)}(t) = \frac{ie}{\varepsilon}\left\{\frac{E_d - iE_{p.v.}\,N_a/N_d}{E_d + E_q - iE_{p.v.}N_a/N_d}\, n_{i1}(t_1) + \left[N_{d1}^{+}(t_1) + \frac{E_q}{E_d + E_q - iE_{p.v.}N_a/N_d}\, n_{i1}(t_1)\right] e^{-\omega_i t}\right\}. \qquad 4.29$$

The relaxation rate which describes this stage of the hologram "life-cycle" is

$$\omega_1 \equiv \omega_e \left[1 + K^2 d^2 - i \frac{E_{p.v.}}{E_q} \left(\frac{N_a}{N_d} \right) \right], \qquad 4.30$$

where the characteristic electric fields are defined as follows:

Characteristic photovoltaic field:

$$E_{p.v.} \equiv \frac{\kappa\sigma/h\nu I_0 (N_d - N_a)}{e\mu_e n_{e0}} = \frac{\kappa\gamma_e N_a}{e\mu_e} . \qquad 4.31$$

The limiting space charge field

$$E_q \equiv \frac{eN_a(1 - N_a/N_d)}{\varepsilon K} . \qquad 4.32$$

The diffusion field

$$E_d \equiv \frac{D_e K}{\mu_e} = \frac{K k_b T}{e} . \qquad 4.33$$

Equation 4.29 predicts a quasi-stabilized field at the end of phase III in the presence of illumination whose value is

$$E_1^{(2)} = \frac{ie}{\varepsilon K} n_{i1}(t_1) \frac{E_d - iE_{p.v.} N_a/N_d}{E_d + E_q - iE_{p.v.} N_a/N_d} , \qquad 4.34$$

independent of the initial trapped charge grating $N_{d1}^{+}(t_1)$. This field can approach the original field $E_1^{(0)}$ provided

$$n_{i1}(t_1) \approx -N_{d1}^{+}(t_0) \quad \text{and} \quad E_1^{(2)} \approx \frac{ie}{\varepsilon K} n_{i1}(t_1) . \qquad 4.35$$

The first condition 4.35 is satisfied when the ionic compensation in phase I is nearly complete which according to equation 4.20 happens, when $\omega_i >> D_iK^2$, i.e., the density of ions is sufficiently large $n_{i0} >> (\varepsilon k_bT/e^2)K^2$ (equation 4.21). This condition, in fact, is most usually satisfied due to the large density of conducting ions at elevated temperature. The second condition is practically more important and requires that the screening of the "fixed" ionic space-charge by trapped electrons during the readout is not strong. According to equation 4.34 this is the case provided

$$|E_d - iN_a/N_dE_{p.v.}| >> E_q . \qquad 4.36$$

This condition may be satisfied for high spatial frequencies, namely $K >> K_e \equiv 1/d$ or in case of strong photovoltaic effect: $E_{p.v.} >> E_q$. In Fe-doped $LiNbO_3$, high developing efficiency can be achieved only in strongly oxidized (large photovoltaic field) weakly (<0.05%wt) Fe-doped crystals, since the limiting space charge field E_q largely exceeds the photovoltaic and diffusion fields otherwise.

(b) Open Circuit

In the open circuit case no spatial-dc current flows through the crystal, but there exists an internally generated (due to the photovoltaic effect) dc field E_0 in the crystal. The solution for the spatially varying component (i.e., hologram) of the electric space charge field is

$$E_1^{(III)}(t) = \frac{ie}{\varepsilon K}\frac{E_d + iE_{p.v.}(N_d\text{-}N_a)/N_d}{E_d + E_q + iE_{p.v.}(N_d\text{-}N_a)/N_d} n_{i1}(t_1) + \frac{ie}{\varepsilon K}\left[N_{d1}^{+}(t_1) + \frac{E_q}{E_d + E_q + iE_{p.v.}(N_d\text{-}N_a)/N_d} n_{i1}(t_1)\right] e^{-\omega_1 t} . \qquad 4.37$$

The characteristic relaxation rate in this case is

$$\omega_1 = \omega_e \left[1 + K^2 d^2 + i \frac{E_{p.v.}}{E_q} \frac{(N_d - N_a)}{N_d} \right]. \qquad 4.38$$

In $LiNbO_3$ the open circuit case in general gives lower diffraction efficiencies [17] during the initial recording, hence, we expect a weaker initial hologram magnitude (smaller $E_1^{(0)}$). Besides, since in strongly oxidize lithium niobate $N_d - N_a << N_d$, the unscreening of the ionic hologram due to photovoltaic effect is also reduced, leading to even weaker developed holograms than in the short-circuited case (compare equations 4.29 and 4.37).

4.6 Ionic grating decay upon readout (phase IV)

(a) Short Circuit

This phase relates directly to the lifetime of the hologram in actual applications. It involves the decay of the ionic backbone grating due to ion (drift + diffusive) transport. In phase III we neglected ionic transport and considered the transient behavior of the grating before the dynamic equilibrium is reached. This was justified since the duration of that phase is short compared to the ionic decay time $(\omega_i + D_i K^2)^{-1}$. The dynamic electronic compensation resulted in a stabilized space charge field (hologram) as given by equation 4.34. This field proceeds to decay to zero because of the ionic transport which erases the ionic backbone charge n_{i1}. This phase usually takes place under light illumination, when the electronic photoconductivity is much larger than the ionic conductivity. The key physical assumption here is that the ionic decay process is sufficiently slow so that while it takes place the faster electronic transport in the presence of light causes the trapped charge density $N_{d1}^{+}(t)$ to be always in equilibrium with n_{i1}. This equilibrium ratio is obtained from equations 4.15 and 4.34 for $t \rightarrow \infty$ (i.e., after the relaxation of the transient)

$$\frac{N_{d1}^{+}(t)}{n_{il}(t)} = -\frac{E_q}{E_d + E_q - iE_{p.v.}\,N_a/N_d}. \qquad 4.39$$

With this last condition we obtain from equation 4.14

$$n_{i1}^{(IV)}(t) = n_{i1}(t_2)\, e^{-[\omega_i\left(\frac{E_d - iE_{p.v.}\,N_a/N_d}{E_d + E_q - iE_{p.v.}\,N_a/N_d}\right) + D_iK^2]\,t} \qquad 4.40$$

for the short-circuit case. We recall that $n_{i1}(t_2) \approx n_{i1}(t_1)$ since phase III is too short for significant ionic transport.

The corresponding grating fields are obtained from equations 4.15 and 4.39 and replacing $n_{il}(t)$ by its solution 4.40. The result is that during phase IV the electronically screened ionic hologram decays to zero due to ionic transport which, however, is slowed down because of partial electronic compensation

$$E_1^{(IV)}(t) = \frac{ie}{\varepsilon K}\left(\frac{E_d - iE_{p.v.}\,N_a/N_d}{E_d + E_q - iE_{p.v.}\,N_a/N_d}\right) n_{i1}(t_1)\, e^{-[\omega_i\left(\frac{E_d - iE_{p.v.}\,N_a/N_d}{E_d + E_q - iE_{p.v.}\,N_a/N_d}\right) + D_iK^2]\,t}. \qquad 4.41$$

(b) Open Circuit

The decay dynamics of the ionic backbone grating in the open circuit case can be found using a similar procedure. The equilibrium trap density modulation in this case is

$$\frac{N_{d1}^{+}(t)}{n_{il}(t)} = -\frac{E_q}{E_d + E_q + iE_{p.v.}(N_d - N_a)/N_d}. \qquad 4.42$$

And the total hologram space-charge field of electronically compensated ionic grating decay is given by

$$E_1^{(IV)}(t) = \frac{ie}{\varepsilon K}\left(\frac{E_d + iE_{p.v.}\,(N_d - N_a)/\,N_d}{E_d + E_q + iE_{p.v.}\,(N_d - N_a)/N_d}\right) n_{i1}(t_1)\, e^{-[\omega_i\left(\frac{E_d + iE_{p.v.}\,(N_d - N_a)/N_d}{E_d + E_q + iE_{p.v.}(N_d - N_a)/N_d}\right) + D_iK^2]\,t}. \qquad 4.43$$

4.7 General remarks on hologram fixing and ionic conduction in $LiNbO_3$

The hologram thermal ionic fixing in photorefractive lithium niobate has been studied extensively [4, 9, 11-14, 18-22]. In general, it is agreed that above 70-80°C the ionic conductivity in this crystal largely prevails over the dark electronic conduction due to Fe^{2+} electron detrapping. At temperatures somewhat below 60°C, however, the conductivity is predominantly due to electrons and is characterized by a small activation energy (0.1 to 0.4 eV) which is due to small polaron electronic conduction associated with the Nb_{Li}^{4+} defect center [23]. This defect (i.e., Nb^{5+} ion occupying a Li^+ crystal lattice cite) is due to the inherent Li-deficiency in congruent lithium niobate and it plays an important role in considerations of the material dark conductivity at and near room temperature. In the presence of light, however, the photoconductivity is governed by Fe-impurities in Fe-doped lithium niobate [24].

The thermally activated ionic (and, similarly, thermally activated electronic) conductivity obeys an Arrhenius-type dependence on the absolute temperature T

$$\sigma_i = en_i\mu_0 e^{-E_a/k_bT}, \qquad 4.44$$

where n_i is the density of ions and E_a is the activation energy. At any given temperature the lifetime of the ionic space-charge is determined by the residual ionic conductivity given by equations 4.17, 4.41, 4.44 and, importantly, is inversely proportional to the density of the conducting ions. It is well established [19,25] that the ionic conductivity in as-grown and hydrogen-doped lithium niobate crystals is predominantly due to the H^+ ions. Hydrogen is normally located in the oxygen planes along the O-O bond and its relative contents can be evaluated, therefore, as the strength (peak or integral) of the OH^- stretching vibration absorption line near 2.87 μm [26]. Vormann *et al.* [19] have shown unambiguously that in

as-grown and H^+-doped crystals the ionic conductivity is due to the hydrogen and deduced the activation energy of E_a =1.2 eV for its migration. It was recognized, though, that in as-grown lithium niobate the residual ionic conductivity gives extrapolated lifetime of an ionic hologram of only 50-70 day at room temperature, and therefore, a substantial reduction of the ion density is essential to increase the available storage time [9,27]. The latter is achieved in our work via substantial dehydration of as-grown crystals.

In what follows, we describe our experimental study on the long-lifetime hologram fixing and ionic conductivity in Fe-doped congruent and non-congruent lithium niobate and, also, present some results on high- and low- temperature electronic dark conductivity.

4.8 Experimental procedure

We investigate hologram fixing and the temperature dependence of the ionic conductivity in Fe-doped lithium niobate crystals grown by Deltronic Crystal Industries. An Ar^+-ion laser with the wavelength λ = 488 nm was used in most of the experiments (Figure 4.3). The crystal is placed on the heater plate whose temperature is controlled with 0.1°C accuracy. The crystal and the heater are enclosed in a vacuum chamber in order to avoid the optical phase perturbations during the recording stage which otherwise occur due to the air density fluctuations in the vicinity of the hot plate. The samples measured 5 mm × 5mm × 10 mm with the longest edge lying along the optical *c*-axis, except for the vapor-transport-equilibrated (VTE) sample which was only about 1 mm thick. The crystals were short-circuited by conducting electrodes placed over the four facets of the crystal.

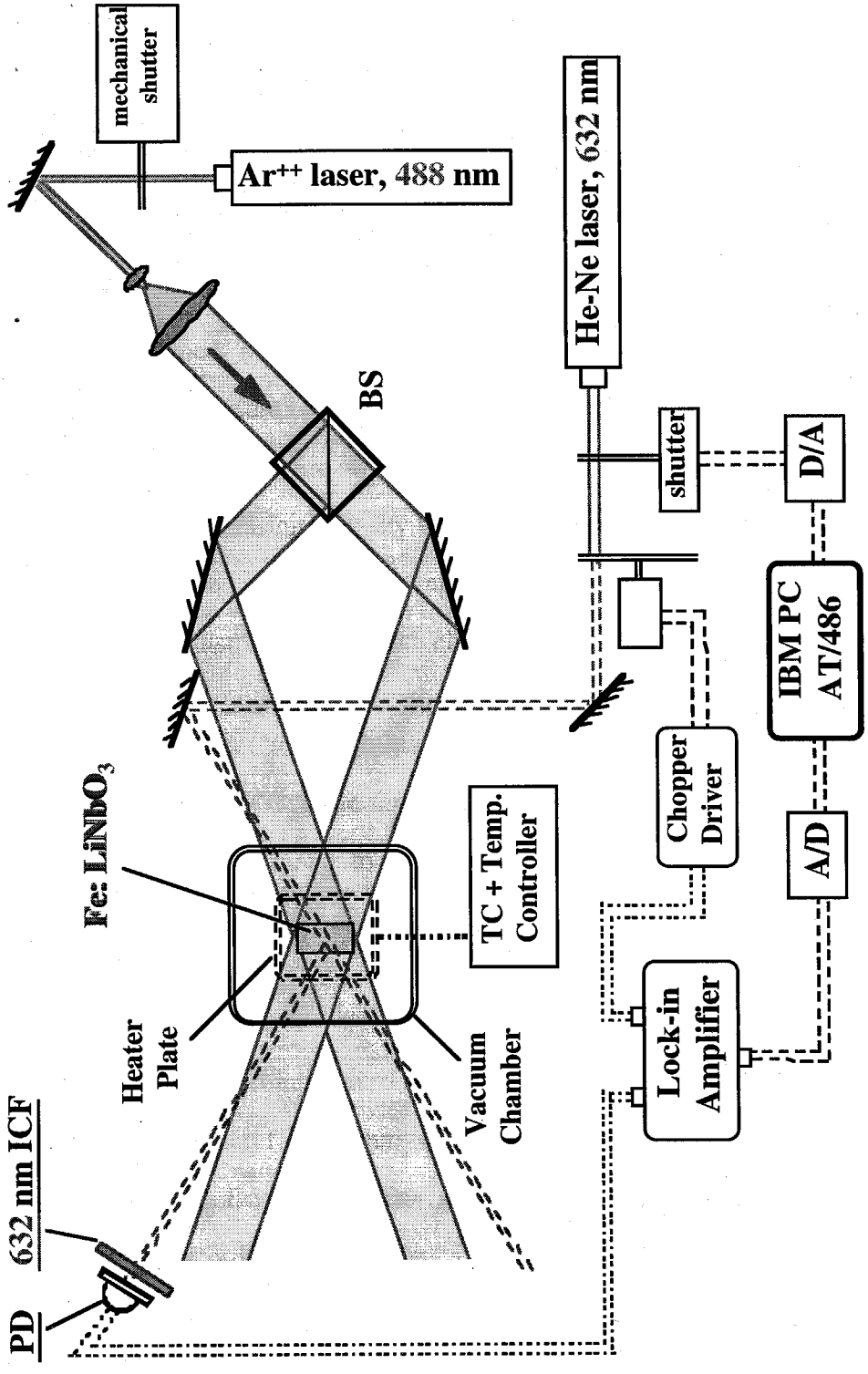

Figure 4.3. Experimental setup.

The holograms are recorded with two equal intensity ordinarily polarized 488 nm beams with the grating vector lying along the *c*-axis direction. The recording beams were expanded to approximately 1 cm in diameter and covered the whole crystal during the recording. The total recording (and erasing) optical intensity was about 100 mW/cm^2. The holographic diffraction efficiency was monitored with a weak Bragg-matched extraordinarily polarized He-Ne laser beam. The diffraction efficiency was sampled at controllable rate (determined mostly by the temperature of the sample during the experiment) to minimize the erasure of the hologram by the probing beam itself. During the developing stage a non-Bragg-matched 488 nm expanded beam was used to issue an approximate uniformity of the erasing intensity throughout the volume of the sample. After each experiment the crystal was heated up to approximately 230°C and soaked for ~30 minutes to achieve uniform distributions of both electrons and ions.

In the fixing experiments ("low-high-low fixing," Section 4.9) the grating was recorded at low temperature (50°C), the sample was heated up in the dark to cause fast ionic transport, and then cooled down to the temperature of recording (50°C). The resulting electronically compensated ionic grating was revealed (developed) with a non-Bragg-matched erasing beam.

The dark decay of ionically compensated trapped electron grating is measured as the decay rate of the weak hologram (see Figure 4.2, phase (2)) left behind after the ionic compensation was complete. Due to very fast ionic screening and high ion density, a prolonged (5-30 minutes) recording of the grating at elevated temperature (T >130°C) was required to obtain a measurable diffracted signal during this stage.

The ionic hologram lifetime (Section 4.12) was determined by monitoring the dark decay (see Figure 4.2, phase (1)) of gratings recorded and stored at different (although

constant throughout each measurement) temperatures. The recording time was kept at a minimum (until the holographic diffraction efficiency reached 10% to 20%).

4.9 Hologram fixing via temperature cycling ("low-high-low" fixing)

Very high diffraction efficiencies of the fixed (reflection) holograms can be obtained via prolonged recording at high temperature [28]. In this case, effectively, the hologram is recorded and ionically compensated many times leading to a substantially higher ionic space charge perturbation. However, this procedure is not practical for complex image-bearing hologram because of the inevitable degradation of the Bragg-conditions due to thermal mismatch. Only simple single gratings can be recorded and fixed using this method. In the holographic data storage it is essential that recording and reconstruction of (fixed) holograms be performed at the same temperature. We, therefore, investigate the fixing of holograms by temperature cycling method (Figures 4.4 and 4.5).

In all of the experiments on "low-high-low" fixing the holograms were initially recorded at 50°C. The ionic compensation is very slow at this temperature and the dark decay time (exponential) of the holograms was more than 100 hours in the samples used. After the recording the writing beams were blocked and the sample with the hologram was heated up to ~120°C in order to cause fast ionic transport. Once the hologram is compensated, the temperature is returned to the initial value corresponding to the recording stage. When the sample temperature is stabilized at 50°C, a non-Bragg-matched expanded beam is shined directly on the crystal to develop (reveal) the fixed holograms. Both crystals used in these experiments have very low hydrogen impurity content (see Section 4.12 below); the magnitude of the OH^- stretching absorption band was < 0.01 cm^{-1} (i.e., below the resolution limit of the spectrometer) and 0.035 cm^{-1} in 0.05% Fe and 0.01% Fe-doped samples respectively.

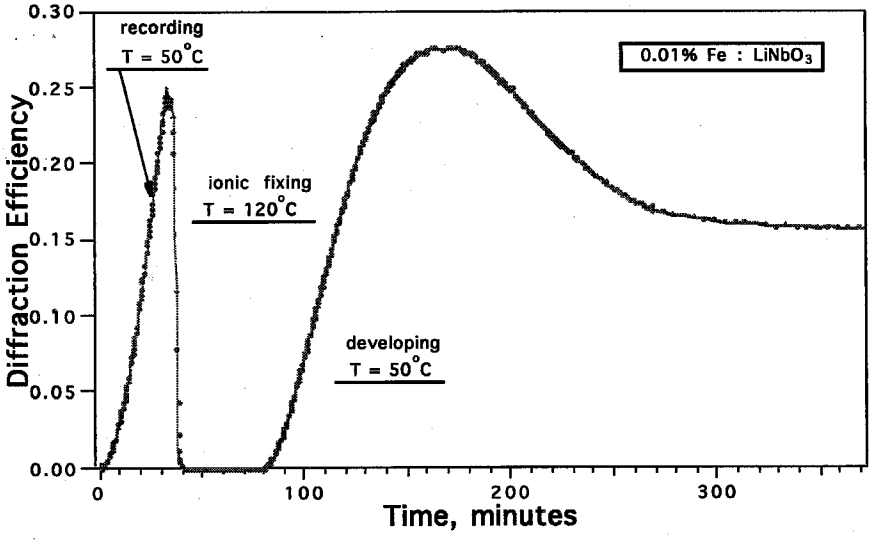

(a)

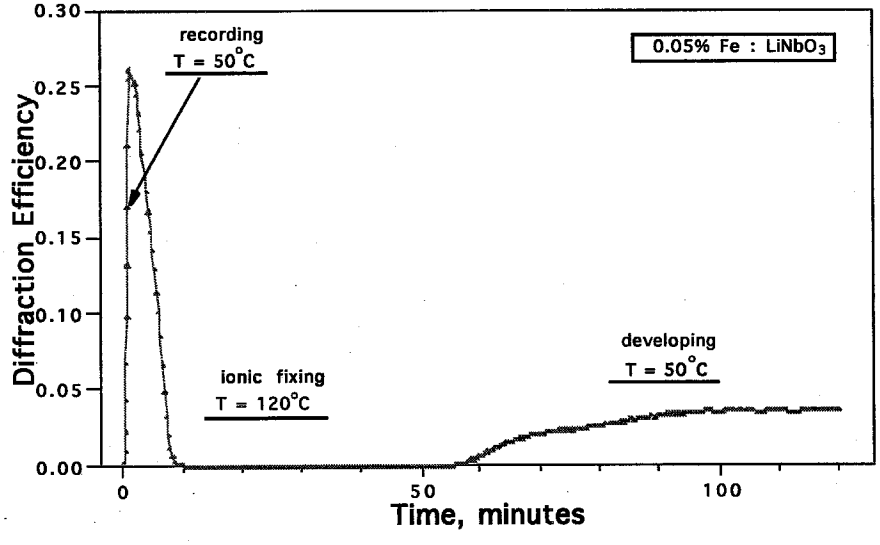

(b)

Figure 4.4. Ionic fixing in oxidized dehydrated lithium niobate crystals with (a) 0.01% Fe and (b) 0.05% Fe-doping. Initial diffraction efficiencies are ~25% and the grating spacing is $2\pi/K \approx 1$ μm in both cases.

In the experiments, shown in Figures 4.4 (a,b) the holograms were recorded for short periods of time until they reach the same magnitude (~25%). This low value of diffraction efficiency is chosen in order to avoid the saturation effects due to the $\sin^2$ dependence of diffraction efficiency on the index perturbation, and, thus, to be able to compare directly the relative fixing / development efficiencies. In agreement with theoretical predictions (see Section 4.5) the fixing / development efficiency depends strongly on Fe-doping and the oxidation state of the crystal. In Fe-doped lithium niobate the limiting space-charge field E_q is proportional to Fe^{2+} density (see equation 4.32):

$$E_q = \frac{e\left[Fe^{3+}\right]\left[Fe^{2+}\right]}{\varepsilon K\left(\left[Fe^{3+}\right]+\left[Fe^{2+}\right]\right)} \approx \frac{e\left[Fe^{2+}\right]}{\varepsilon K}. \qquad 4.45$$

The limiting space charge field E_q determines the degree of electronic screening of fixed ionic hologram (equation 4.34) and the fixing / developing efficiency is decreased with increasing $[Fe^{2+}]$ (Figure 4.4 (b)). At the same time, almost 70% reconstruction efficiency (i.e., weak screening) is realizable in weakly Fe-doped crystals as shown in Figure 4.4(a). This observation also demonstrates that the electronic detrapping from Fe^{2+}-sites can be avoided even in lithium niobate with largely reduced ionic conductivity (i.e., low hydrogen impurity content).

Shown in Figures 4.5 (a), (b) are the fixing experiments in which the recording was performed until the perturbation in the index reaches its steady state. The maximal index perturbation which can be induced in oxidized lithium niobate is larger the higher the Fe-doping. However, the developing efficiency decreases with Fe-doping as well. The net result is that the fixed holograms have almost the same efficiencies in the crystals with different iron dopant concentration (see Figures 4.5 (a,b)) when the "low-high-low" fixing technique is used.

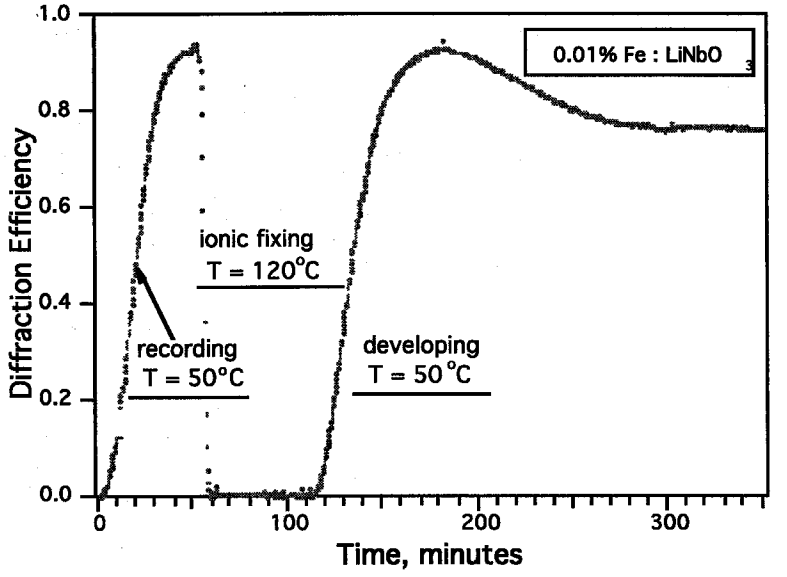

(a)

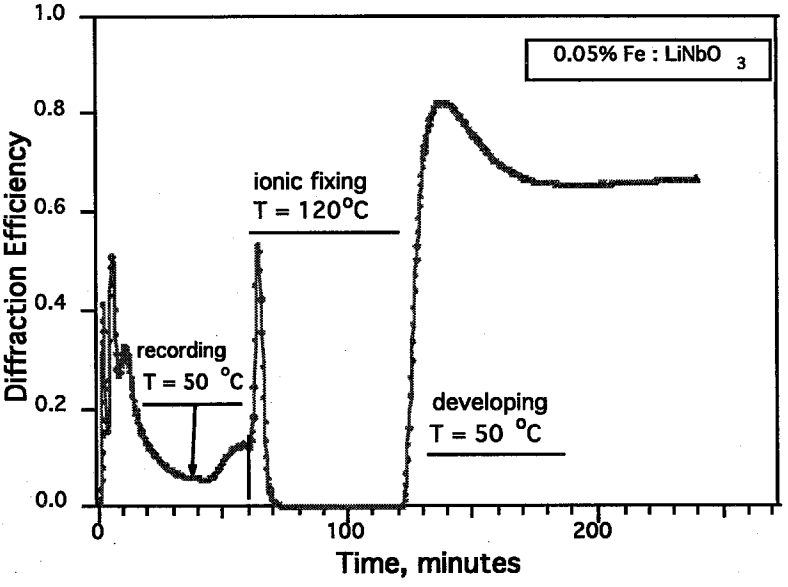

(b)

Figure 4.5. Ionic fixing in oxidized dehydrated lithium niobate crystals with (a) 0.01% Fe and (b) 0.05% Fe-doping. The holograms were recorded for approximately 1 hour until the saturation was reached. The oscillations in the recording curve in (b) are due to the $\sin^2$ dependence of η on index perturbation δn. The grating spacing is $2\pi/K \approx 1$ μm in both cases.

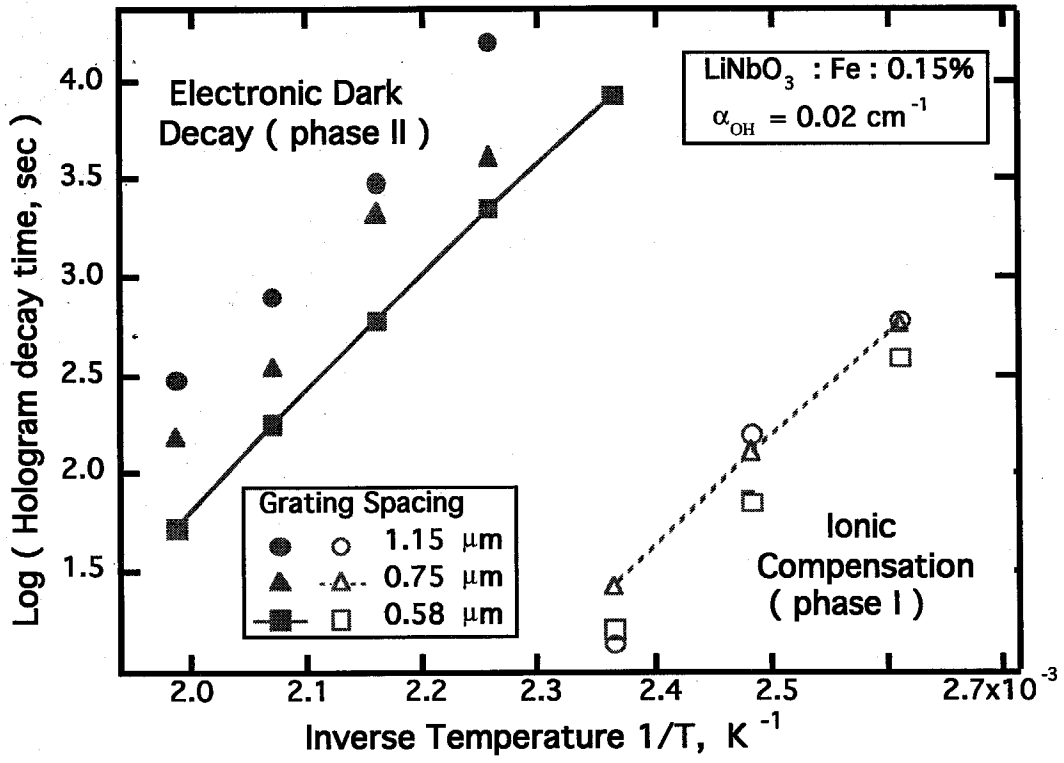

Figure 4.6. Arrhenius plot of the hologram dark electronic decay time (phase II).

4.10 Dark electronic decay at elevated temperature

A hologram recorded at elevated temperature and left in the dark experiences fast ionic compensation (Figure 4.2, phase (1)), which, of course, also takes place during recording if the ionic conductivity is larger or comparable to the electronic photoconductivity. Fast ionic decay is further followed by a much slower electronic grating decay which is due to electron detrapping from Fe^{2+} sites (Figure 4.2, phase (2)). The ionic compensation is very strong due to the relatively high density ($> 10^{18}$ cm^{-3}) of compensating ions and, therefore, the residual weak index grating may have both the electrooptic (that due to the remaining electric field as given by equation 4.20) and the photochromic contributions

[29]. Arrhenius plot of dark electronic decay time in 0.15% Fe-doped congruent lithium niobate for different grating spacings is shown in Figure 4.6. The corresponding ionic lifetimes are also shown as a reference. In agreement with theory the dark electronic grating lifetime strongly depends on the grating spacing (equation 4.25). At the same time, ionic decay time (fast stage of the decay) is almost independent of the grating spacing. We also observe that if the erasing light is shined on the crystal during the phase (2) of Figure 4.2, the weak residual grating decays rapidly to zero at a rate which is close to that of the recording stage. Thus, the slow decay can be enhanced by light and, therefore, is indeed electronic. It is worth emphasizing that above ~90°C, even in heavily Fe-doped oxidized lithium niobate crystals, the ionic conductivity is higher than the dark electronic conduction (due to both thermal Fe-detrapping and the small polaron Nb_{Li}^{4+} shallow trap defect).

4.11 Ionic hologram decay upon readout.

Ionic transport is the mechanism which is responsible both for the ionic compensation in the dark (Figure 4.1, phase I) and for the decay of the fixed ionic grating during the readout (Figure 4.1, phase IV). The latter, however, can be slowed down to a certain amount due to the compensation effect of the electronic grating. Figures 4.7 (a,b) show the evolution of two holograms which were recorded, fixed, and reconstructed at 90°C (temperature was kept constant throughout the experiments) in the dehydrated lithium crystals with different iron dopant concentration. In the crystal with low Fe-doping (0.01% Fe, small E_q) the rate of ionic decay during the readout is very close to the dark compensation rate. This is not surprising since the electronic screening is weak in this crystal (Figure 4.4 (a)). The higher doped crystal exhibits substantial electronic screening (Figure 4.7 (b)), and, consequently, the decay upon development is slower (approximately by a factor of 5 in the conditions of Figure 4.7 (b)) than that during the ionic compensation.

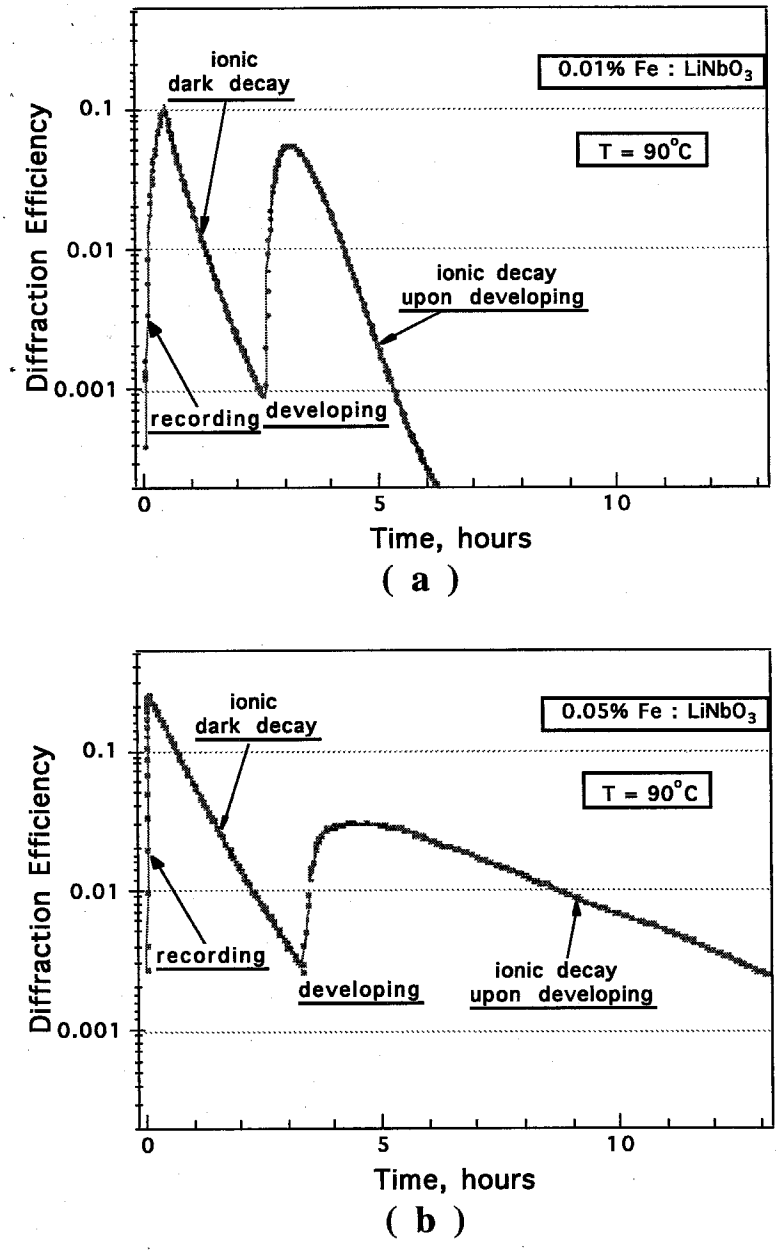

Figure 4.7. Recording, ionic compensation, developing, and final decay of the holograms in oxidized dehydrated lithium niobate crystals with (a) 0.01% Fe and (b) 0.05% Fe-doping. In (b) the fixed grating decay is ~5 times slower than the ionic compensation (ionic dark decay) due to stronger electronic screening, while in (a) they are almost equal. The ratio between the decay rate in the dark and the decay rate of the fixed ionic grating upon readout is preserved, as long as the ionic conductivity is much smaller than the electronic photoconductivity (i.e., for $T \leq \sim 100^{\circ}C$). The grating spacing is $2\pi/K \approx 1$ μm in both cases.

At the same time, the reconstruction efficiency (in this case, the ratio between the maximal value of reconstructed signal and the initially recorded signal) is substantially lower than in the case of weak electronic compensation (see also Figure 4.4 (b)). It can be concluded, therefore, that for a given residual ionic conductivity and a given storage temperature, an increase in the lifetime of an electronically compensated fixed ionic hologram can be achieved *only* at the proportionate expense of its reconstruction efficiency.

4.12 Lifetime of the fixed ionic hologram

The lifetime of a fixed ionic grating is determined mainly by the conductivity σ_i of ionic species at given temperature T, i.e. $\tau \propto \varepsilon\varepsilon_0/\sigma_i$, where σ_i is given by equation 4.44. In order to determine the ionic conductivity and the corresponding activation energies we measure the dark decay time (Figure 4.2, phase (1)) of the holograms recorded and stored at different (although, constant throughout each experiment) temperatures. We find, that in as-grown congruent lithium niobate crystals with fairly high hydrogen content (measured as the strength of the OH^- absorption near 2.87 μm) the ionic conductivity exhibits a ~1.2 eV activation energy and is relatively high (Figure 4.8, sample (a)). This activation energy is characteristic for hydrogen conductivity [19, 25]. The lifetime extrapolated to room temperature (24 °C) is about 50 days, which is too short for the majority of applications [27]. Partial electronic screening under illumination slows down the ionic decay but at the same time decreases the grating strength (see Section 4.11 and equation 4.41). Therefore, the most feasible mechanism for increasing the fixed hologram lifetime is the decrease in the ionic conductivity, which can be achieved by reducing the total density of conducting ions. The high temperature (~950°C) post growth processing in dry oxygen atmosphere results in a substantial reduction up to 100 times compared to as-grown of OH^- density in the crystal and leads to a significant increase in the ionic hologram lifetime. However, we

find (Figure 4.8 (b,c)) that after substantial hydrogen removal, the ionic conductivity is determined by a species other than hydrogen. The ionic conductivity in dehydrated crystals does not depend on the hydrogen density as opposed to the linear dependence of σ_i on [OH^-] found in as-grown and hydrogen doped samples [19,25]. The activation energy also differs from that typical for the H^+ impurity transport and is equal to ~1.4 eV. The fixed ionic hologram lifetime in dehydrated samples at room temperature (24°C) can be extrapolated to be about 2 years.

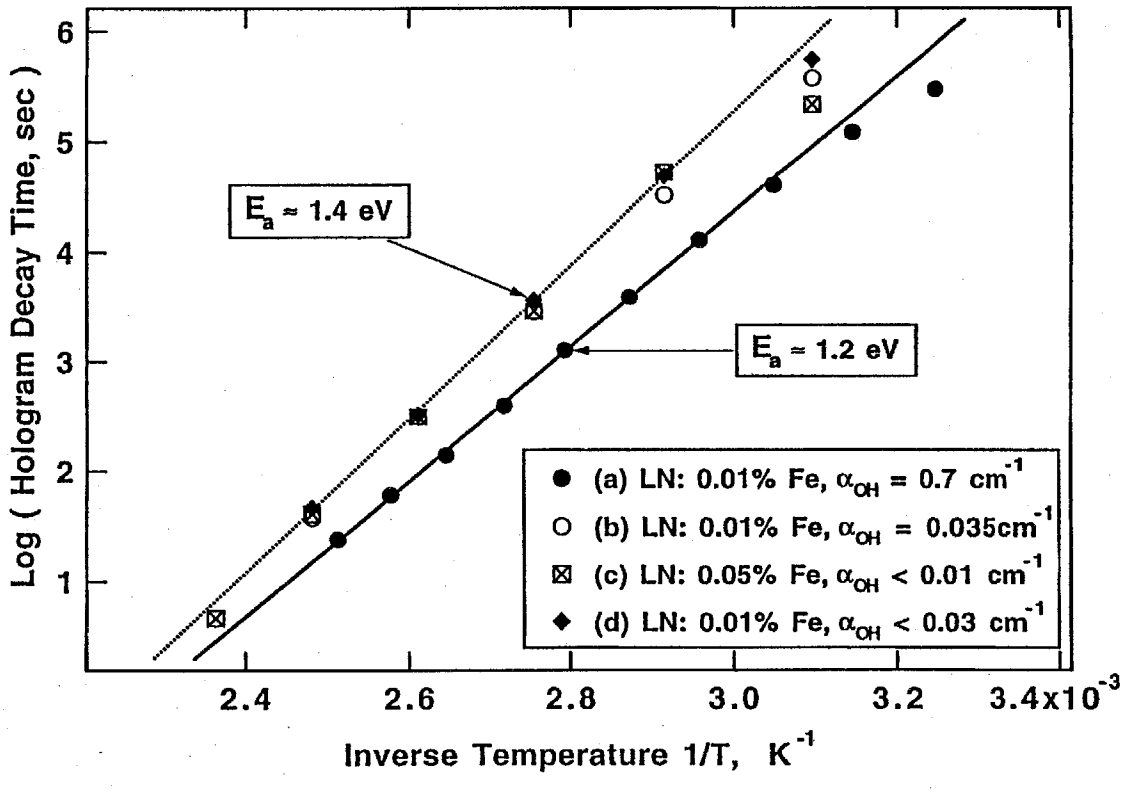

Figure 4.8. Arrhenius plot of the ionic hologram lifetime in (a) as-grown (E_a = 1.2 eV) crystal, (b,c) samples with low hydrogen impurity content and different Fe-doping (E_a = 1.4 eV), (d) Li_2O equilibrated (VTE processed) crystal. The fall-off in the hologram lifetime in the low temperature range (i.e., when T < 70°C) is due to the shallow trap (Nb_{Li}^{4+} small polaron defect) electronic decay in nonstoicheometric lithium niobate.

In order to investigate the influence of lithium vacancies on the ionic conductivity [30], a more stoicheometric sample was prepared using vapor transport equilibration (VTE) technique [31, 32]. The processing temperature was 1080°C, and the processing time was 400 hours for a 1 mm thick *a* -cut lithium niobate crystal. The Li_2O content in this sample was estimated to be at least 49.5% (congruent lithium niobate contains 48.6% Li_2O [33]) from the phase-matching angle measurements for the second harmonic generation at 1.064 μm [34]. In the temperature range studied in our experiments the ionic conductivity in the VTE sample also exhibits a ~1.4 eV activation energy (Figure 4.8, sample (d)) and is nearly the same as the one in congruent dehydrated lithium niobate. This may rule out the mechanisms of ionic conduction which involve a substantial role of lithium vacancies / lithium deficiency. The nature of ionic conducting species in the dehydrated lithium niobate crystals is yet to be determined. Migration of lithium self-interstitials [32] may be a possible mechanism responsible for the ionic conductivity with activation energy of 1.4 eV.

It should be noted that the ionic conductivity with the 1.4 eV activation energy *and* the substantially increased ionic hologram lifetimes at room temperature can be found only in fully oxidized lithium niobate crystals with very low hydrogen impurity content ($[OH^-] < 5\times10^{17}$ cm^{-3}, that is for OH^- absorption at 2.87 μm less than 0.05 cm^{-1}). In the samples with higher hydrogen contents the dark decay time constant may exhibit activation energies which are ranging widely from 0.9 eV to 1.4 eV, depending on the density of H^+ impurity, range of the temperatures used in the experiments, and the oxidation state and density of the iron dopant [20-22, 35].

4.13 Summary

Holographic gratings which are based on charge redistribution inevitably decay due to ionic and electronic conduction. Relevant decay rates and transient hologram field expressions are derived. Ionic gratings are partially screened by trapped electrons upon readout. The lifetimes of *fixed* ionic holograms are limited by the finite ionic conductivity at low (i.e., room) temperature. A significant increase in fixed ionic hologram lifetime is realized in lithium niobate with low hydrogen impurity content. The residual ionic conductivity (decay time constant) in these samples exhibits ~1.4 eV activation energy and is *not* due to protonic conduction. Fixed hologram lifetimes of about 2 years at room temperature are projected in dehydrated lithium niobate crystals.

There is a good agreement between the experimental results on hologram fixing in Fe-doped photorefractive lithium niobate and the prediction of the theory. Experimental study reveals some new features in the holographic ionic fixing and related low temperature ionic conductivity in lithium niobate. A few main conclusions are worth emphasizing:

(a) At elevated temperature (T> ~60°C for lithium niobate) the initial decay of the recorded grating is due to ionic compensation (phase I). Under dark storage conditions, the (phase II) decay as described by equation 4.23 is due to the thermal electronic transport slowed down by ionic screening.

(b) A near perfect development and fixing (i.e., $E_1(t_2) \approx E_1(t_0)$ in Figure 4.1) can be obtained provided that the screening of the residual ionic grating by electronic grating is weak upon read-out. According to equation 4.34, this happens when $|E_d - iN_a/N_dE_{p.v.}| >> E_q$. This condition is realized in weakly iron doped oxidized lithium

niobate crystals with strong photovoltaic response. The fixing efficiency can be close to 100% in such crystals.

(c) Under illumination (phase IV) the hologram is quasi-stabilized. The residual decay is due to the transport of the ionic charge backbone (equation 4.41). Major reduction of the ionic conductivity at the operating temperature is necessary to bring this decay rate to the acceptable range of lifetimes $\geq$ 10 years. An increase of the fixed hologram lifetime can be also achieved due to strong electronic compensation, but only at the expense of its reconstruction efficiency (equation 4.41).

(d) Substantial increase in the fixed (ionic hologram) lifetime can be realized in lithium niobate crystals with low hydrogen content. The residual ionic conductivity (and associated hologram decay time constant) exhibits a ~1.4 eV activation energy and is not due to protonic conduction. Fixed hologram lifetimes at room temperature of about 2 years are projected in dehydrated crystals.

References for Chapter four

[1] J. F. Heanue, M. C. Bashaw, and L. Hesselink, Science **265**, 749 (1994).

[2] D. Psaltis and F. Mok, Sci. Am. **273**, 70 (1995).

[3] J. H. Hong, I. McMichael, T. Y. Chang, W. Christian, and E. G. Paek, Opt. Eng. **34**, 2193 (1995).

[4] J. J. Amodei and D. L. Staebler, Appl. Phys. Lett. **18**, 540 (1971).

[5] F. Micheron and G. Bismuth, Appl. Phys. Lett. **20**, 79 (1972).

[6] D. Kirillov and J. Feinberg, Opt. Lett. **16**, 1520 (1991).

[7] G. Montemezzani and P. Günter, J. Opt. Soc. Am. B **7**, 2323 (1990).

[8] G. Montemezzani, M. Zgonik and P. Günter, J. Opt. Soc. Am. B **10**, 171 (1993).

[9] A. Yariv, S. Orlov, G. Rakuljic, and V. Leyva, Opt. Lett. **20**, 1334 (1995).

[10] S. Orlov, D. Psaltis, and R. R. Neurgaonkar, Appl. Phys. Letts. **63,** 2466 (1993).

[11] M. Carrascosa and F. Agullo-Lopez, J. Opt. Soc. Am. B **7**, 2317 (1990).

[12] R. Matull and R. A. Rupp, Journal of Physics D - Appl. Physics **21** , 1556 (1988).

[13] V. V. Kulikov and S. I. Stepanov, Sov. Phys. Solid State **21**, 1849 (1979).

[14] P. Hertel, K. H. Ringhofer, and R. Sommerfeldt, Phys. Status Solidi A **104**, 855 (1987).

[15] N. K. Kukhtarev, Sov. Tech. Phys. Lett. **2**, 438 (1976).

[16] W. Bollmann, phys. stat. sol. (a) **104**, 643 (1987).

[17] C. Gu, J. Hong, H. Y. Li, D. Psaltis, and P. Yeh, J. Appl. Phys. **69**, 1167 (1991).

[18] W. Bollman and H. J. Stöhr, Phys. Stat. Solidi (a) **39**, 477 (1977).

[19] H. Vormann, G. Weber, S. Kapphan, and M. Wöhlecke, Solid State Commun. **57**, 543 (1981).

[20] L. Arizmendi, P. D. Townsend, M. Carrascosa, J. Baquedano and J. M. Cabrera, J. Phys. Cond. Matter **3**, 5399 (1991).

[21] M. Carrascosa and L. Arizmendi, J. Appl. Phys. **73**, 2709 (1993).

[22] R. Müller, L. Arizmendi, M. Carrascosa, and J. M. Cabrera, J. Appl. Phys. **77**, 308 (1995).

[23] O. F. Schirmer, O. Thiemann, and M. Wöhlecke, J. Phys. Chem. Solids **52**, 185 (1991).

[24] T. Volk, N. Rubinina, and M. Wöhlecke, J. Opt. Soc. Am. B **11**, 1681 (1994).

[25] S. Klauer, M. Wöhlecke, and S. Kapphan, Phys. Rev. B **45**, 2786 (1992).

[26] J. R. Herrington, B. Dischler, A. Rauber, and J. Schneider, Solid State Commun. **12**, 351 (1973).

[27] A. Yariv, V. Leyva, and G. A. Rakuljic, "Relaxation and lifetime of "fixed" charge holograms," in *Technical Digest, 1994 IEEE Nonlinear Optics, Materials, Fundamentals, and Applications,* Waikoloa, Hawaii, post-deadline paper PD6.

[28] G. A. Rakuljic and A. Yariv, "Photorefractive systems and methods," U.S. Patent #5,440,669 (Aug. 8, 1995).

[29] D. L. Staebler, W. J. Burke, W. Phillips, and J. J. Amodei, Appl. Phys. Lett. **26**, 182 (1975).

[30] A. Mehta, E. K. Chang, and D. M. Smyth, J. Mater. Res. **6**, 851 (1991).

[31] P. F. Bordui, R. G. Norwood, D. H. Jundt, and M. M. Fejer, J. Appl. Phys. **71**, 875 (1992).

[32] D. H. Jundt, M. M. Fejer, R. G. Norwood, and P. F. Bordui, J. Appl. Phys. **72**, 3468 (1992).

[33] S. C. Abrahams and P. Marsh, Acta Cryst. B **42**, 61 (1986).

[34] U. Schlarb and K. Betzler, Phys. Rev. B **48**, 15613 (1993).

[35] L. Kovàcs and K. Polgar, in *Properties of lithium niobate*, EMIS Datareview series No 5, p.109, RN-16037 (1989).

Chapter Five

Material Response, Noise in Optical Detection, and Holographic Storage Capacity

5.1 Introduction

Holographic data storage initially proposed during the 1960s [1-3] uses the concept of storing data in the form of multiplexed holographic gratings distributed through the volume of the recording media. Bragg selectivity provided by the volume interaction allows independent retrieval of each of the pages of data stored in the common volume on the basis of the optical parameters such as the wavelength of light (wavelength multiplexing [4]), incidence angle of the reference (angular multiplexing [5]), or the spatial distribution of reference light (phase-encoding [6, 7], shift multiplexing [8]). The attractiveness of this storage architecture [9, 10] is due to its highly parallel access to the stored data, very short access time (< 100 μs), as well as potentially large theoretical capacity given by, essentially, the *diffraction limit* of ~V/λ^3 bits in a volume V. The actual amount of information which can be stored in the volumetric storage media may differ significantly due to a number of reasons which include the interpage and interpixel cross-talk present in

any multiplexing technique [11-14], optical scattering noise of the material [15], as well as the optical detection noise and finite material dynamic range [16, 17].

Due to the finite dynamic range of the media (i.e., the finite maximum index perturbation δn_{max} which can be induced) the amplitude of the sinusoidal index perturbation representing an individual bit is smaller the larger the total number of bits recorded. Therefore, the diffracted signal which represents an individual bit of data decreases with the number of bits. The minimal signal which can be detected is limited by the optical detection noise: thermal and 1/f noise of the detector, and more fundamentally, the quantum shot noise. Given the source optical power, readout rate, and optical frequency, the requirement of a given signal-to-noise ratio (SNR) upon detection and, ultimately, the quantum shot noise set the upper limit on the number of bits which can be stored.

In this chapter we present an estimate of the number of bits, sharing the same volume of the recording material, which can be stored and faithfully retrieved with acceptable bit-error-rate. This estimate limits the storage capacity of a single volume; further increase can be achieved by spatial multiplexing, i.e., the use of spatially non-overlapping volumes.

5.2 Diffraction efficiency per bit

We assume that each individual bit n is stored in the form of a sinusoidal index grating $\delta n_n(\mathbf{r})$ with the grating vector $\mathbf{k}_n$ and a constant (real) amplitude for each bit δn_k:

$$\delta n_n(\mathbf{r}) = \delta n_0 + \frac{\delta n_k}{2} e^{-i(\mathbf{k}_n \cdot \mathbf{r} + \theta_n)} + \frac{\delta n_k}{2} e^{i(\mathbf{k}_n \cdot \mathbf{r} + \theta_n)}, \qquad 5.1$$

where δn_0 is the dc term in the index perturbation, and θ_n is the phase of the n-th grating. The $\delta n_n(\mathbf{r})$ is given by equation 5.1 if the corresponding bit is 1 and $\delta n_n(\mathbf{r}) \equiv 0$ otherwise.

The diffraction efficiency η_{bit} due to the index perturbation 5.1 is given by the Kogelnik's formula [18] and, in the limit of weak index perturbation considered here, is

$$\eta_{bit} \cong \left(\frac{\pi L \, \delta n_k}{\lambda} \right)^2 , \qquad 5.2$$

where L is the length of the crystal and λ is the wavelength of light. For maximal storage capacity the diffraction efficiencies for all "1" bits should be the same, since the noise spectrum is uniform [19] (the noise is determined by the detection system and, thus, does not depend on the bit number n or the grating vector $\mathbf{k}_n$).

The δn_k can be considered as the magnitude of the index perturbation due to individual bit of information in the $\mathbf{k}$-space. In the real space the total index perturbation $\delta n(\mathbf{r})$ is the sum over $\delta n_n(\mathbf{r})$ given in 5.1:

$$\delta n(\mathbf{r}) = \Sigma_{n=1}^{N_{bit}} \left(\delta n_0 + \frac{\delta n_k}{2} e^{-i(\mathbf{k}_n \cdot \mathbf{r} + \theta_n)} + \frac{\delta n_k}{2} e^{i(\mathbf{k}_n \cdot \mathbf{r} + \theta_n)} \right), \qquad 5.3$$

where N_{bit} is the total number of bits stored in the single storage volume. The finite dynamic range of the material limits the maximal index perturbation in the *real* space $\delta n(\mathbf{r})$, i.e., both first and second moments of the $\delta n(\mathbf{r})$ must satisfy the following conditions:

$$\langle \delta n(\mathbf{r}) \rangle < \delta n_{max} , \qquad 5.4$$

$$\left\langle \left(\delta n(\mathbf{r}) \right)^2 \right\rangle < \delta n_{max}^2 , \qquad 5.5$$

where $\langle \ \rangle$ denotes the statistical expectation value (w.r.t. random phases θ_n). Therefore, given the maximal index perturbation δn_{max}, the maximal δn_k can be calculated using equations 5.3-5.5. The minimal reliably detectable η_{bit} is determined by the optical detection noise and acceptable SNR.

5.3 Optical detection noise and minimal diffraction efficiency

One of the most fundamental sources of noise in the optical detection system is the shot noise. Other sources include Johnson thermal noise, 1/f noise, relative intensity noise of the source laser, etc. The quantum shot noise gives the lowest possible (fundamental) limit to the noise power in the detection system (unless quantum squeezing is introduced, what is not relevant to the topic considered here - the low diffraction efficiency would reduce the degree of squeezing dramatically and the diffracted light incident on the detector would have the usual Poissonian statistics anyway).

The power diffracted due to a single bit in a page is $P_0\eta_{bit}$, where P_0 is the source laser power. The average signal current generated by a photodetector with unity quantum efficiency is

$$\bar{i}_s = e\bar{N} = e\frac{P_0\,\eta_{bit}}{h\nu}. \qquad 5.6$$

The mean-square noise current amplitude due to the shot noise is [20]

$$\overline{i_N^2} = 2e\bar{i}_s\Delta f \cong 2e\bar{i}_s/\tau, \qquad 5.7$$

where τ is the readout time. The (amplitude) signal-to-noise ratio SNR is then given by

$$SNR = \frac{\bar{i}_s}{\sqrt{\overline{i_N^2}}} = \left(\frac{P_0\,\eta_{bit}\,\tau}{2\,h\nu}\right)^{1/2}. \qquad 5.8$$

For a given specified readout bit-error-rate the SNR is a given number and, thus, equation 5.8 places the lower limit on the minimal diffraction efficiency per bit $(\eta_{bit})_{min}$ for the system in which the dominant noise source is the shot noise in the optical detection system:

$$(\eta_{bit})_{min} = \frac{2h\nu(SNR)^2}{P_0 \tau} \quad . \qquad 5.9$$

For the typical parameters of P_0 = 100 mW, τ = 100 μs, $h\nu = 5.10^{-19}$ J, and SNR = 20 (~26 dB), the estimate 5.9 gives $(\eta_{bit})_{min} \approx 10^{-10}$, which translates into the minimal power per bit of ~10^{-11} Watt (or, $2(SNR)^2$ = 800 received optical quanta per bit per readout).

The noise properties of the commercial detectors (which are not necessarily determined by the ultimate quantum shot noise) are usually characterized by the noise equivalent power (NEP, in $W/\sqrt{Hz}$). The SNR in such a detection system is simply

$$SNR = \frac{P_0 \eta_{bit}}{NEP \sqrt{\Delta f}} = \frac{P_0 \eta_{bit} \sqrt{\tau}}{NEP} \quad . \qquad 5.10$$

And, therefore, the minimal diffraction efficiency per bit is

$$(\eta_{bit})_{min}^{NEP} = \frac{SNR \cdot NEP}{P_0 \sqrt{\tau}} \quad . \qquad 5.11$$

Using the same values of parameters P_0, τ, and SNR, and taking a typical (low) NEP value of 10^{-14} $W/\sqrt{Hz}$, we calculate $(\eta_{bit})_{min}^{NEP} \approx 2\times10^{-10}$ and minimum power per bit of ~2×10^{-11} Watt. In what follows we consider the limitations due to the quantum shot noise, as given by 5.8-5.9, and then give the corresponding formulas for the case when other noise sources are dominant (as described by equations 5.10- 5.11).

5.4 Media without erasure and dc saturation

In this (ideal) media each bit (and page of information) can be recorded without erasing the index grating of the others and there is no dc saturation during the recording, i.e., $\delta n_0 \equiv$

0 in the equation 5.3. Then, obviously, $\langle \delta n(\mathbf{r}) \rangle \equiv 0$ and condition 5.4 is satisfied automatically. The calculation of the second moment (equation 5.5) gives

$$\langle \delta n^2(\mathbf{r}) \rangle = \frac{(\delta n_k)^2}{4} \left\langle \sum_{n=1}^{N_{bit}} \sum_{m=1}^{N_{bit}} \left(e^{i((\mathbf{k}_n - \mathbf{k}_m)\cdot\mathbf{r} + (\theta_n - \theta_m))} + e^{i((\mathbf{k}_n + \mathbf{k}_m)\cdot\mathbf{r} + (\theta_n + \theta_m))} + \text{c.c.} \right) \right\rangle =$$

$$= \frac{(\delta n_k)^2}{4} \left\langle \sum_{n=1}^{N_{bit}} \sum_{m=1}^{N_{bit}} 2\delta_{n,m} \right\rangle = \frac{(\delta n_k)^2}{2} N_{bit} . \qquad 5.12$$

The mean-square value of the index perturbation in the real space $\langle \delta n^2(\mathbf{r}) \rangle$ cannot exceed the maximum squared index perturbation δn^2_{max}. Therefore, the maximal index variation per each bit δn_k is equal (equation 5.12)

$$\delta n_k = \frac{\delta n_{max} \sqrt{2}}{\sqrt{N_{bit}}} . \qquad 5.13$$

The diffraction efficiency per bit (given by equation 5.2) is then equal to

$$\eta_{bit} = 2\pi^2 \frac{\delta n^2_{max}}{N_{bit}} \left(\frac{L}{\lambda} \right)^2 , \qquad 5.14$$

and must be more than or equal to the minimal value $(\eta_{bit})_{min}$ calculated from detection noise considerations, and which is given by the (shot noise limit) equation 5.9. This gives the estimate for the maximum number of bits N_{bit} which can share the same volume in the material without dc saturation and erasure:

$$N_{bit} = \pi^2 \left(\frac{P_0 \tau}{h\nu (SNR)^2} \right) \delta n^2_{max} \left(\frac{L}{\lambda} \right)^2 . \qquad 5.15$$

For a cubic storage volume with $L/\lambda = 10^4$ (i.e., $L \approx 0.5$ cm), $\delta n_{max} = 10^{-3}$ and typical parameters given in Section 5.3 the estimate 5.15 gives $N_{bit} \approx 5.10^{13}$ bits, which is far beyond the diffraction limit of $(L/\lambda)^3 \approx 10^{12}$ bits. Therefore, the conclusion can be drawn

that in a media with no dc saturation and erasure, the diffraction limit can be achieved and the main limiting factor is the information cross-talk rather than the optical detection noise.

5.5 Photorefractive media

The index gratings in photorefractive materials are produced by the redistribution of photoexcited electrons between traps, buildup of the internal space-charge field, and electrooptic effect. Recording of each subsequent page of information partially erases the index grating of previously recorded pages. Let the information be arranged in M pages with page capacity of n_0 bits/page (the total number of bits is $N_{bit} = Mn_0$). For recording of a single page the results of the previous Section (equation 5.13) for the maximum index variation per bit apply, and, therefore

$$(\delta n_k)_{1\ page} = \frac{\delta n_{max}\sqrt{2}}{\sqrt{n_0}}, \qquad 5.16$$

where $(\delta n_k)_{1\ page}$ is the index perturbation (in **k**-space) per bit in a single page. Subsequent recording of M-1 pages decreases δn_k. Since for maximal storage capacity [20] the magnitude of the index gratings in different pages has to be equal, we consider incremental recording [21] (i.e., the best case scenario for the uniformity of the page diffraction efficiencies), in which each page is recorded for a short period of time ($\Delta t M << t_{resp}$, where t_{resp} is the recording response time of the material), sequentially ($1 \rightarrow 2 \rightarrow ... \rightarrow M-1 \rightarrow M \rightarrow 1 \rightarrow 2...$), until the saturation is reached. The change in the index perturbation of an individual bit per cycle of recording is

$$\Delta(\delta n_k)_{cycle} \cong 1 \cdot \Delta t \frac{(\delta n_k)_{1\ page}}{t_{resp}} - M \cdot \Delta t \frac{\delta n_k}{t_{resp}}, \qquad 5.17$$

where the first term describes the recording of the bit grating due to one page, the second represents the erasure (and saturation) due to M pages. We also neglect possible asymmetry between recording and erasure time constants, which is a correct approximation unless hologram fixing techniques are employed. In the steady state $\Delta(\delta n_k)_{cycle} = 0$ and, therefore, (also using the expression for $(\delta n_k)_{1\ page}$, equation 5.16)

$$\delta n_k = \frac{1}{M}\cdot(\delta n_k)_{1\ page} = \frac{\delta n_{max}\sqrt{2}}{M\sqrt{n_0}} = \frac{\delta n_{max}\sqrt{2\,n_0}}{N_{bit}}. \qquad 5.18$$

The diffraction efficiency (equation 5.2) due to individual bit grating δn_k is given by

$$\eta_{bit} = 2\pi^2 \frac{\delta n_{max}^2\, n_0}{(N_{bit})^2}\left(\frac{L}{\lambda}\right)^2, \qquad 5.19$$

and, unlike the case of the material without erasure (equation 5.14) is inversely proportional to the *square* of the total number of bits N_{bit} (and the square of the total number of holograms M [1, 16]). Comparing the diffraction efficiency 5.19 and the minimal value $(\eta_{bit})_{min}$ which is given by the (shot noise) detection limit (equation 5.9), one arrives to the following expression for the maximum number of bits N_{bit} which can be stored in a common location in the volumetric photorefractive media:

$$N_{bit} = \pi\sqrt{\left(\frac{P_0\,\tau}{h\nu\,(SNR)^2}\,n_0\right)}\,\delta n_{max}\left(\frac{L}{\lambda}\right). \qquad 5.20$$

The maximum storage capacity of a single storage location grows only as a first power of the media length L, besides the capacity increases with the information content of an individual page n_0 (in agreement with results in [16]). For a cubic storage volume with $L/\lambda = 10^4$ (i.e., $L \approx 0.5$ cm), $\delta n_{max} = 10^{-3}$, $n_0 = 10^6$ bits/page (1000×1000 pixel per page), and

typical values of P_0, τ, SNR, and $h\nu$ given in Section 5.3, the estimate 5.20 gives $N_{bit} \approx 7.10^9$ bits = 7 Gbit, which is *far below* the ultimate diffraction limit of $(L/\lambda)^3 \approx 10^{12}$ bits. Therefore, in the case of holographic storage in thick photorefractive media the optical detection noise and finite material response (rather then the cross-talk) represent the main factors limiting the ultimate capacity of an individual storage location [22].

5.6 Photochemical recording media (photopolymers, doped silica, etc.)

In these media (e.g., photopolymers) the change in the index of refraction is produced due to the chemical reaction inside the volume of the material [16, 22]. Since the chemical reaction is strongly irreversible, subsequent exposure does not erase the previously recorded holograms, as long as the total index change is below its maximum saturation value δn_{max}. The index change is proportional to the total light exposure and saturates as the reactive radicals are depleted. The intensity distribution which records a refractive index grating for an individual bit in a page (equation 5.1) is of the form

$$\frac{I_n(\mathbf{r})}{m} = \frac{I_k}{m} + \frac{I_k}{2} e^{-i(\mathbf{k}_n \cdot \mathbf{r} + \theta_n)} + \frac{I_k}{2} e^{i(\mathbf{k}_n \cdot \mathbf{r} + \theta_n)}, \qquad 5.21$$

where m is the modulation index ($m \leq 1$). This intensity distribution produces the index variation $\delta n_n(\mathbf{r})$

$$\delta n_n(\mathbf{r}) = \frac{\delta n_k}{m} + \frac{\delta n_k}{2} e^{-i(\mathbf{k}_n \cdot \mathbf{r} + \theta_n)} + \frac{\delta n_k}{2} e^{i(\mathbf{k}_n \cdot \mathbf{r} + \theta_n)}, \qquad 5.22$$

where $\delta n_k = S \Delta t I_k$ (S is the current (after depletion due to previous recording) photosensitivity of the material and Δt is the exposure time). Equation 5.22 shows that unlike the photorefractive materials and "ideal" media of Section 5.4, in the materials with photochemical mechanism of recording, because of the chemical depletion, the creation of the sinusoidal grating also necessarily leads to the *dc terms* in the index of refraction

distribution. For the best case of unity modulation index m=1, the average index change in the material due to N_{bit} bits (equation 5.3) is

$$\langle \delta n(\mathbf{r}) \rangle = \left\langle \Sigma_{n=1}^{N_{bit}} \left(\delta n_k + \frac{\delta n_k}{2} e^{-i(\mathbf{k}_n \cdot \mathbf{r} + \theta_n)} + \frac{\delta n_k}{2} e^{i(\mathbf{k}_n \cdot \mathbf{r} + \theta_n)} \right) \right\rangle = \delta n_k \, N_{bit} \, . \qquad 5.23$$

The average index perturbation $\langle \delta n(\mathbf{r}) \rangle$ cannot exceed the maximum saturation index change of the material δn_{max}. Therefore, the maximal index variation per each bit δn_k is given by

$$\delta n_k = \frac{\delta n_{max}}{N_{bit}} \, . \qquad 5.24$$

The consideration of the second moment $\langle \delta n^2(\mathbf{r}) \rangle$ (equation 5.5) does not change this estimate significantly (in fact, it gives $\delta n_k = \delta n_{max}/\sqrt{N_{bit}^2 + N_{bit}} \approx \delta n_{max}/N_{bit}$, i.e., essentially the same value of δn_k for $N_{bit} >> 1$). The diffraction efficiency per bit (as given by equation 5.2) is then given by

$$\eta_{bit} = \pi^2 \frac{\delta n_{max}^2}{N_{bit}^2} \left(\frac{L}{\lambda} \right)^2 , \qquad 5.25$$

which has to be more than, or equal to the minimal value $(\eta_{bit})_{min}$ determined by the optical detection noise (shot noise, equation 5.9). The estimate for the maximum number of bits N_{bit} which can be stored in a common location of a photochemical storage media is then given by

$$N_{bit} = \pi \sqrt{\left(\frac{P_0 \tau}{2h\nu \, (SNR)^2} \right)} \, \delta n_{max} \left(\frac{L}{\lambda} \right) . \qquad 5.26$$

For the *bulk* cubic storage volume with $L/\lambda = 10^4$ (i.e., $L \approx 0.5$ cm), typical values of P_0, τ, SNR, $h\nu$ same, as given in Section 5.3, and $\delta n_{max} = 0.1$ (probably, maximum for

photopolymer materials), the estimate 5.26 gives $N_{bit} \approx 5.10^8$ bits = 0.5 Gbit, which is *far below* the ultimate diffraction limit of $(L/\lambda)^3 \approx 10^{12}$ bits, and, therefore, the dynamic range of the material and optical detection noise is, indeed, the major limiting factor. In case of storage in a *thin* photopolymer film [22] ($L/\lambda = 10^2$,i.e., $L \approx 50$ μm; and $\delta n_{max} \approx 0.01$), the detection noise limit 5.26 is $N_{bit} \approx 5.10^5$ bits, while the diffraction limit is $(L/\lambda)^3 \approx 10^6$. The two values are comparable and, therefore, in case of storage in thin photopolymer films the major capacity limitations may arise from the information cross-talk [22].

5.7 Comparison of different storage media

To summarize, the maximum number of bits N_{bit} which can share the same location volume of the storage material are (equations 5.15, 5.20, and 5.26):

$$N_{bit}\Big|_{\text{"ideal"}} = \pi^2 \left(\frac{P_0 \tau}{h\nu\,(SNR)^2} \right) \delta n_{max}^2 \left(\frac{L}{\lambda} \right)^2, \qquad 5.27$$

$$N_{bit}\Big|_{\text{photorefractive}} = \pi \sqrt{\left(\frac{P_0 \tau}{h\nu\,(SNR)^2}\, n_0 \right)}\, \delta n_{max} \left(\frac{L}{\lambda} \right), \qquad 5.28$$

$$N_{bit}\Big|_{\text{photochemical}} = \pi \sqrt{\left(\frac{P_0 \tau}{2h\nu\,(SNR)^2} \right)}\, \delta n_{max} \left(\frac{L}{\lambda} \right). \qquad 5.29$$

These are plotted in Figure 5.1 for typical values of parameters P_0, τ, $h\nu$, SNR, etc., as a function of the volume thickness L/λ. In case of the bulk volumetric storage ($L/\lambda > 10^3$) only in the "ideal" media without erasure and dc saturation the storage capacity is limited by the information cross-talk. The finite dynamic range and optical detection noise is the dominant factor which limits the storage capacity of holographic memory based on photorefractive and photochemical materials. The hologram fixing after the recording of

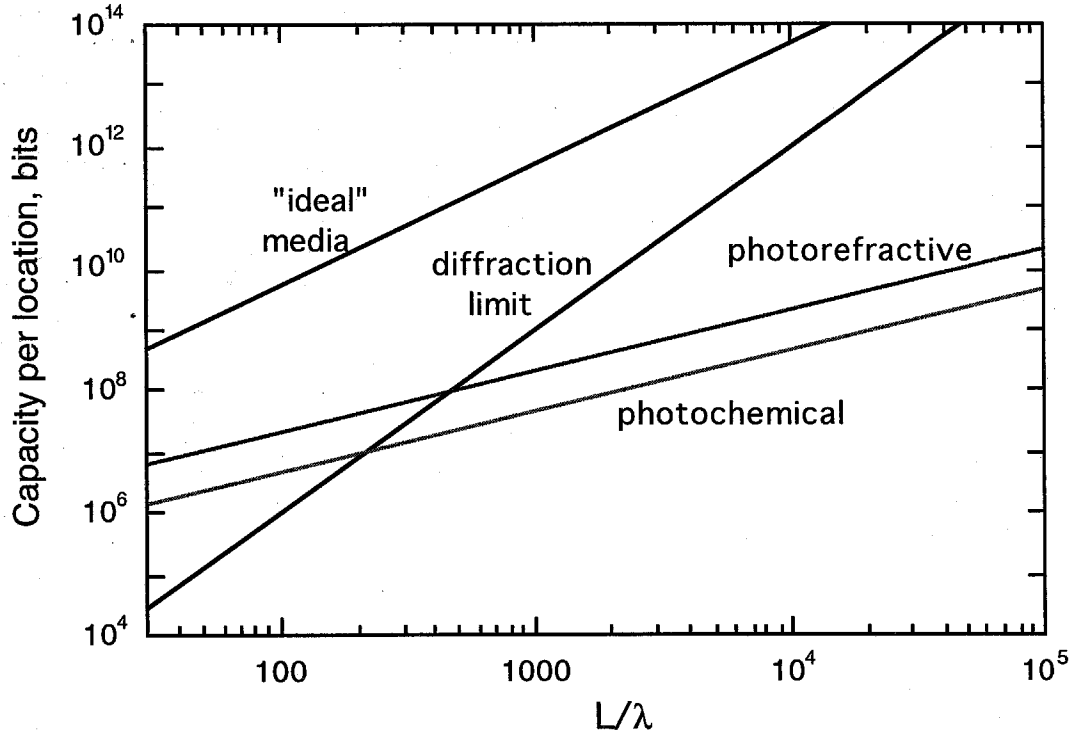

Figure 5.1. Storage capacity of an individual location for different storage media and diffraction limit vs. volume size L. The parameters used in calculations: optical power P_0 = 0.1 W, $h\nu = 5.10^{-19}$ J, required signal-to-noise ratio SNR = 20, readout time τ = 100 μs; page capacity $n_0 = 10^5$ bit/page and $\delta n_{max} = 10^{-4}$ (for photorefractive media); $\delta n_{max} = 10^{-3}$ ("ideal" media without erasure and dc saturation); $\delta n_{max} = 0.1$ for photochemical media (photopolymer).

each individual information page in photorefractives could increase the effective dynamic range and, thus, the ultimate storage capacity.

A substantial increase in the total capacity using currently available materials can also be achieved by using multiple, independent, spatially non-overlapping storage volumes with an individual storage unit size of the order of 100 μm (see Figure 5.1). In this case

(relatively thin storage media, massive spatial multiplexing, i.e., holographic disk [22,23]), the maximum storage capacity is mainly limited by the **k**-space information cross-talk, and with the use of appropriate multiplexing technique [4- 8] the storage capacity may approach the diffraction limit of V/λ^3.

5.8 Other noise sources in the optical detection system

So far we have considered the optical detection noise due to the quantum shot noise. It should be noted that the calculations based on this type of noise give the lowest possible limit for the diffraction efficiency per bit (equation 5.9), and, therefore, the maximal, most optimistic values of the maximal storage capacity (equations 5.27- 5.29). The noise properties of a real detection system may be worse than those of the system limited by the quantum shot noise (this may be the case particularly for multiple pixel detector arrays). Other noise sources include the thermal Johnson noise, relative intensity noise of the source laser, the amplifier noise, as well as the optical scattering noise of the media itself. As mentioned in section 5.3, the resulting noise characteristic of the whole detection *system* (i.e., the optical detector, laser, amplifier, etc.) can be characterized by the noise equivalent power (NEP, in $W/\sqrt{Hz}$), which is the power of the input optical signal which produces the output rms signal equal to the output rms noise of the system (in 1 Hz bandwidth). The NEP can be calculated given the noise parameters of the detector ($\overline{e_n}$, $\overline{i_n}$, R_{in}), the noise figures of the amplifiers, etc.. In the regime when the NEP dominates over the quantum shot noise limit, the signal-to-noise ratio is given by equation 5.10, and the minimal diffraction efficiency per bit is (equation 5.11):

$$(\eta_{bit})_{min}^{NEP} = \frac{SNR \cdot NEP}{P_0\sqrt{\tau}} \quad . \qquad 5.30$$

Using this expression in the derivations of the maximal N_{bit} instead of the shot noise limit (equation 5.9), we arrive to the following formulas for the maximal number of bits which can be stored in a single location of the storage media for the case when the optical detection system is limited by the noise sources other than the quantum shot noise:

$$N_{bit}\Big|_{\text{"ideal"}}^{NEP} = \pi^2 \left(\frac{2 P_0 \sqrt{\tau}}{NEP \cdot SNR} \right) \delta n_{max}^2 \left(\frac{L}{\lambda} \right)^2, \qquad 5.31$$

$$N_{bit}\Big|_{\text{photorefractive}}^{NEP} = \pi \sqrt{\left(\frac{2 P_0 \sqrt{\tau}}{NEP \cdot SNR} n_0 \right)} \delta n_{max} \left(\frac{L}{\lambda} \right), \qquad 5.32$$

$$N_{bit}\Big|_{\text{photochemical}}^{NEP} = \pi \sqrt{\left(\frac{P_0 \sqrt{\tau}}{NEP \cdot SNR} \right)} \delta n_{max} \left(\frac{L}{\lambda} \right). \qquad 5.33$$

5.9 Summary

The storage capacity of holographic media is limited by the information cross-talk, the finite material response (dynamic range), and the optical detection noise. The ultimate lowest level of the latter is given by the quantum shot noise. For the bulk ($L/\lambda > 10^3$) volumetric storage media (e.g., photorefractives or photopolymers) the dominant limiting factor is the dynamic range of the media and the optical detection noise. The volumetric storage densities close to the diffraction limit of V/λ^3 *and* high storage capacities (~1 Tbit) can be achieved only via massive spatial multiplexing (use of multiple independent storage volumes) in relatively thin materials ($L/\lambda \approx 10^2$).

References for Chapter Five

[1] E. N. Leith, A. Kozma, J. Upatneiks, J. Marks, and N. Massey, Appl. Opt. **5**, 1303 (1966).

[2] J. P. VanHeerden, Appl. Opt. **2**, 393 (1963).

[3] E. G. Ramberg, RCA Review **33**, 5-53 (1972).

[4] G. A. Rakuljic, V. Leyva, and A. Yariv, Opt. Lett. **17**, 1471 (1992).

[5] L. d'Auria, J. P. Huignard, C. Slezak, and E. Spitz, Appl. Opt. **13**, 808 (1974).

[6] C. Denz, G. Pauliat, G. Roosen, and T. Tschudi, Opt. Commun. **85**, 171 (1991).

[7] H. Sasaki, J. Ma, Y. Fainman, and S. H. Lee, Opt. Lett. **17**, 1468 (1992).

[8] D. Psaltis, M. Levene, A. Pu, G. Barbastathis, and K. Curtis, Opt. Lett. **20**, 782 (1995).

[9] J. F. Heanue, M. C. Bashaw, and L. Hesselink, Science **265**, 749 (1994).

[10] J. H. Hong, I. McMichael, T. Y. Chang, W. Christian, E. G. Paek, Opt. Eng. **34**, 2193 (1995).

[11] C. Gu, J. Hong, I. McMichael, R. Saxena, and F. H. Mok, J. Opt. Soc. Am. A **9**, 1978 (1991).

[12] A. Yariv, Opt. Lett. **18**, 652 (1993).

[13] K. Curtis and D. Psaltis, J. Opt. Soc. Am. A **10**, 2547 (1993).

[14] M. C. Bashaw and L. Hesselink, J. Opt. Soc. A. B **11**, 1820 (1994).

[15] S. V. Miridonov, A. V. Khomenko, D. Tentori, and A. A. Kamshilin, Opt. Lett. **19**, 502 (1994).

[16] K. Bløtekjaer, Appl. Opt. **18**, 57 (1979).

[17] A. Lahrichi, K. Johnson, E. Maniloff, and G. Fredericks, J. Opt. Soc. Am. A **9**, 749 (1992).

[18] H. Kogelnik, Bell. Syst. Tech. J. **48**, 2909 (1969).

[19] C. Shannon, Proc. IRE **37**, 1 (1949).

[20] A. Yariv, *Optical Electronics*, 3rd edition, (Holt, Rinehart, and Winston, New York, 1985), Chapter 10.

[21] Y. Taketomi, J. E. Ford, H. Sasaki, J. Ma, Y. Fainman, and S. H. Lee, Opt. Lett. **16**, 1774 (1991).

[22] K. Curtis, "3-D photopolymer disks for correlation and data storage, and cross-talk in volume holographic memories," Ph. D. thesis, California Institute of Technology (1994).

[23] D. Psaltis and F. Mok, Sci. Am. **273**, 70 (1995).

Chapter Six

Double Phase Conjugation in Photorefractive Media

6.1 Introduction

The phase conjugate replica of a monochromatic optical field is a field, of the same frequency (in the frequency degenerate case considered here), whose wavefronts take the same shape throughout space, but propagate in the opposite direction at every point [1]. There are several methods of generating optical phase conjugation, such as three- and four-wave mixing, stimulated Brillouin and Raman scattering. Among them, the four-wave mixing (Figure 6.1) is a very efficient and low threshold optical technique for the cw phase conjugate wave generation [1]. For low light intensities the photorefractive materials are unique in their abilities to display large nonlinearities over the entire visible, as well as the near infrared range, what makes them an attractive candidate for demonstration of a variety of four-wave mixing phase conjugate oscillators.

The first photorefractive oscillator [2,3] involved a photorefractive $BaTiO_3$ crystal externally pumped with a pair of counterpropagating beams. This resulted in the build-up of the oscillation in the form of another pair of counterpropagating beams in an external

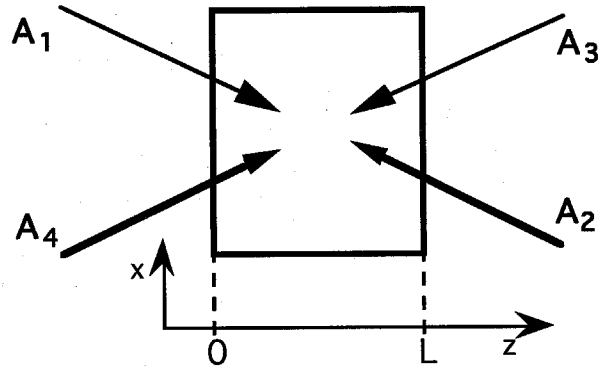

Figure 6.1. A schematic diagram of a four-wave mixing interaction.

cavity. Subsequently, a large number of self-pumped and externally pumped photorefractive oscillators has been developed [4-8]. Some of them are depicted in Figure 6.2. One of the most interesting and basic interactions (although discovered in its "pure" form the latest [8]) is the Double Phase Conjugate Mirror (DPCM) - a photorefractive device in which two mutually incoherent input beams create phase conjugates of each other (Fig. 6.2 (g)). The two incoherent beams cannot write stationary gratings in the photorefractive crystals because of their slow response (0.1 Hz to 10 kHz typically), but the effective interaction between the input beams is produced through the scattering off each other's noise holographic gratings. The gratings which are common for both of the beams experience strong amplification and if the gain of the medium is large enough, the double phase conjugate oscillation establishes itself [8]. The result of these oscillations is that the two beams which don't need to be coherent, produce each others phase conjugate replicas. The basic properties of DPCM (e.g., oscillation and threshold conditions) can be understood within the framework of the general mode-coupling formalism of four-wave mixing in photorefractives [4]. However, a more refined analysis, which accounts for the

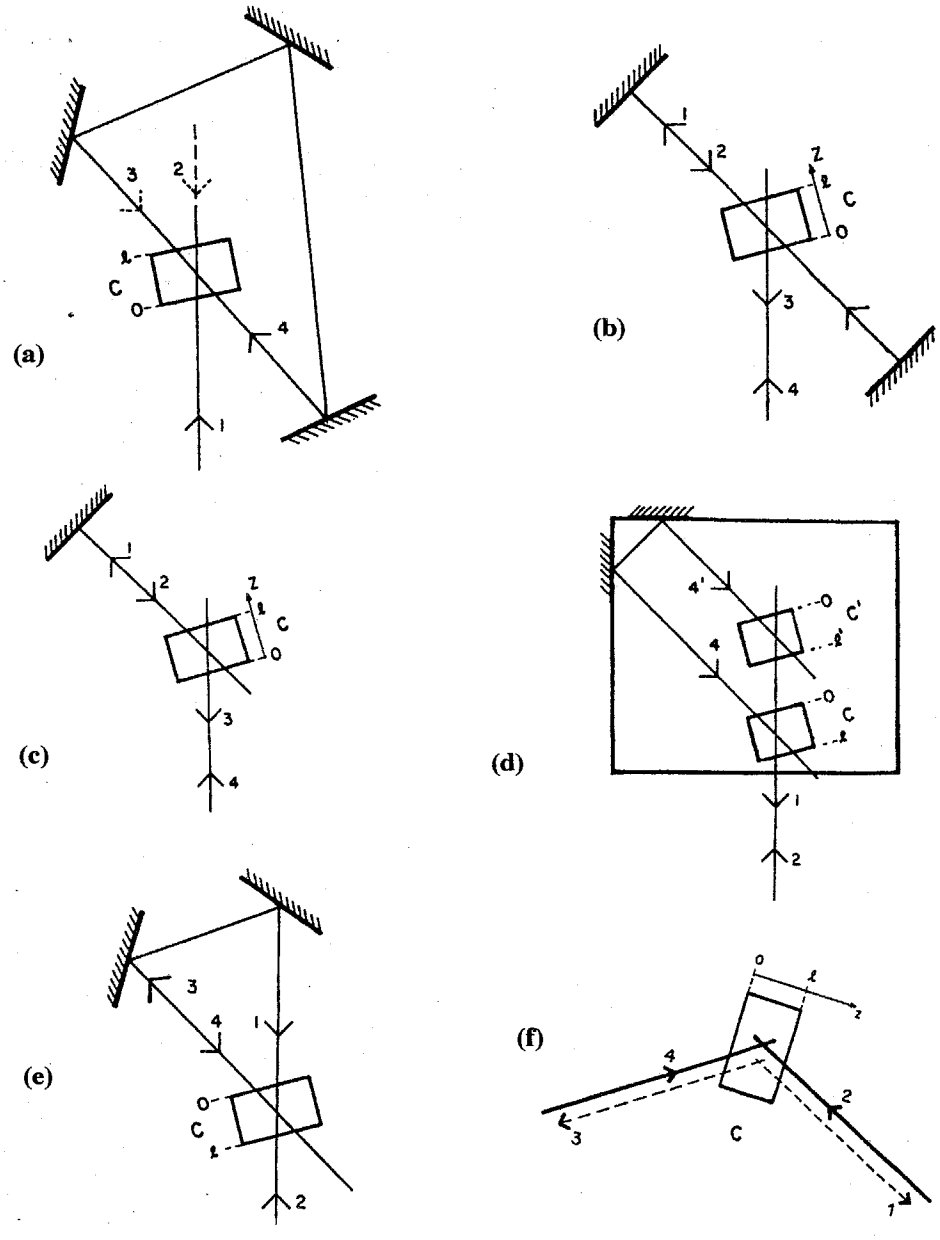

Figure 6.2. Photorefractive oscillators. (a) The bidirectional ring oscillator (with beams 2 and 3 present). (b) Linear passive phase conjugate mirror (PPCM). (c) Semilnear PPCM. (d) Total internal reflection ("cat") mirror. (e) Ring oscillator. (f) Double phase conjugate mirror.

spatial structure of the interacting waves, is necessary if one addresses the issues such as the quality of phase conjugation (phase conjugate fidelity), signal-to-noise ratio in phase conjugation, and conjugation with amplification of the conjugated signal. These topics are of particular importance for the understanding of the limitations of particular device applications, e.g., in image processors [9, 10], multimode-to-singlemode fiber couplers [11], phase conjugate interferometers [12], and coupled-laser devices [13].

In the past few years a number of two dimensional theoretical models of DPCM has been proposed which take into account the complex spatial structure of the interacting optical waves. The model by Segev *et al.* [14, 15] invokes the decomposition of the input beams into a discrete set of eigenmodes of the free space (i.e., plane waves). The interaction between the individual planewave components is then considered in a fashion similar to the conventional one-dimensional theory [8]. Another approach used by Shkunov *et al.* [16, 17] describes the self-pumped phase conjugation of a speckled beam [18]. The interacting beams are assumed to consist of a set of interacting angular components which are located within a wide solid angle and have arbitrary phases. The resulting index perturbation and wave amplitudes are then obtained via statistical averaging over the ensemble of realizations of the speckle structure. Yet another theoretical model (by Zozulya *et al.* [19-21]) is based on paraxial wave propagation of the interacting waves, which are assumed to have finite extent in the transverse dimension with a slowly varying envelope. A special emphasize is made on the noncollinearity of the interacting beams. One of the main conclusions of this formulation is that the DPCM is a convective noise amplifier (like, e.g., SBS conjugator) rather then a nonlinear optical oscillator [19].

In this chapter we will present the results of our experimental study [22, 23] of DPCM, review the basic one-dimensional model, as well as the formulation and basic results of the two-dimensional model of double phase conjugation [15].

6.2 Basic coupled-modes analysis of the DPCM

The electric field of each of the interacting optical beams (Figure 6.1) is represented as

$$E_j(\mathbf{r}, t) = A_j(\mathbf{r}) \exp\left(i(\mathbf{k_j}\cdot\mathbf{r} - \omega t)\right) + c.c.\,, \qquad 6.1$$

where $A_j(\mathbf{r})$ is a slowly varying amplitude of the j-s beam. The two pairs of interacting beams {1, 4} and {2, 3} induce the photorefractive index grating whose grating vector $\mathbf{k_g}$ is given by

$$\mathbf{k_g} = \mathbf{k_4} - \mathbf{k_1} = \mathbf{k_2} - \mathbf{k_3}\ . \qquad 6.2$$

The coupled equations for the complex amplitudes $A_j(z, t)$ are obtained by substituting equations 6.1 and the expression for the index perturbation into the wave equation

$$\nabla^2 E + (n_0 + \Delta n)^2 k^2 E = 0\,, \qquad 6.3$$

and are given by [4, 8]

$$\frac{\partial A_1}{\partial z} = ik\Delta n A_4\,, \qquad 6.4$$

$$\frac{\partial A_2^*}{\partial z} = ik\Delta n A_3^*\,, \qquad 6.5$$

$$\frac{\partial A_3}{\partial z} = ik\Delta n A_2 , \qquad 6.6$$

$$\frac{\partial A_4^*}{\partial z} = ik\Delta n A_1^* , \qquad 6.7$$

where $k = 2\pi/\lambda$ is the wave number and $\Delta n(z)$ is the perturbation in the refractive index. These coupled waves equations are supplemented by the equation for the index perturbation

$$\tau\frac{\partial \Delta n}{\partial t} + \Delta n = \gamma\left(\frac{A_1 A_4^* + A_2^* A_3}{I_0}\right), \qquad 6.8$$

where $I_0 = \Sigma|A_j|^2$ is the total optical intensity, the response time τ is inversely proportional to I_0, and $\gamma = i\omega\Delta n/c$ is the nonlinear coupling coefficient which is imaginary in photorefractive materials without external or photovoltaic field, thus enabling power exchange between beams. The analysis of the DPCM [8] shows that the intensity of the phase conjugate output can be greater or less than their corresponding input , depending upon the strength of the coupling constant for the crystal, and the ratio of the input intensities. The boundary and initial conditions for the set of equations 6.3-6.8 are

$$A_2(z=L, t) = A_{20} , \qquad 6.9$$

$$A_4(z=L, t) = A_{40} , \qquad 6.10$$

$$A_1(z=0, t) = A_3(z=L, t) = 0 , \qquad 6.11$$

$$\Delta n\,(z, t=0) = 0 . \qquad 6.12$$

An expression for the symmetric intensity transmission $T = I_3(0)/I_2(L) = I_1(L)/I_4(0)$ in the steady state is given by [8]

$$T = \frac{a^2}{4}\left(\left[q^{-1/2} + q^{1/2}\right]^2 - \left[q^{-1/2} - q^{1/2}\right]^2 \right), \qquad 6.13$$

where $q = I_4(0)/I_2(L)$ is the input intensities ratio and a is related to the gain-length product γL by

$$a = \tanh\left(-a\frac{\gamma L}{2}\right) = \tanh\left(-a\frac{\gamma L}{\gamma L_{th}}\right). \qquad 6.14$$

The DPCM has the lowest oscillation threshold $(\gamma L)_{th} = 2$ for the case of equal input intensities q=1 (PC reflectivity and transmittivity T both are equal to a^2 in this case). The transient solution [24] (for $a^2 << 1$) gives the characteristic time τ_{ss} to reach the steady state

$$\tau_{ss} = \frac{\tau}{\gamma L - \gamma L_{th}}. \qquad 6.15$$

The two properties of DPCM as given by equations 6.14 and 6.15 indicate the self-oscillation (i.e., T>0 even when no seeding signal is present) and critical slowing down [23] (i.e., $\tau_{ss} \rightarrow \infty$ for $\gamma L \rightarrow (\gamma L)_{th}$).

6.3 Conjugation fidelity and reflectivity

In this Section we present experimental evidence of a threshold in the conjugation fidelity of the DPCM. In addition, we observe that the fidelity threshold depends on the feature size in the conjugated images. The phase conjugate reflectivity, however, is a smooth function of the gain. We have also modified the input beams' intensity ratio until one output is well phase conjugated while the other output is masked by the noise. These results are useful for an understanding of the limitations of particular device applications [9-13].

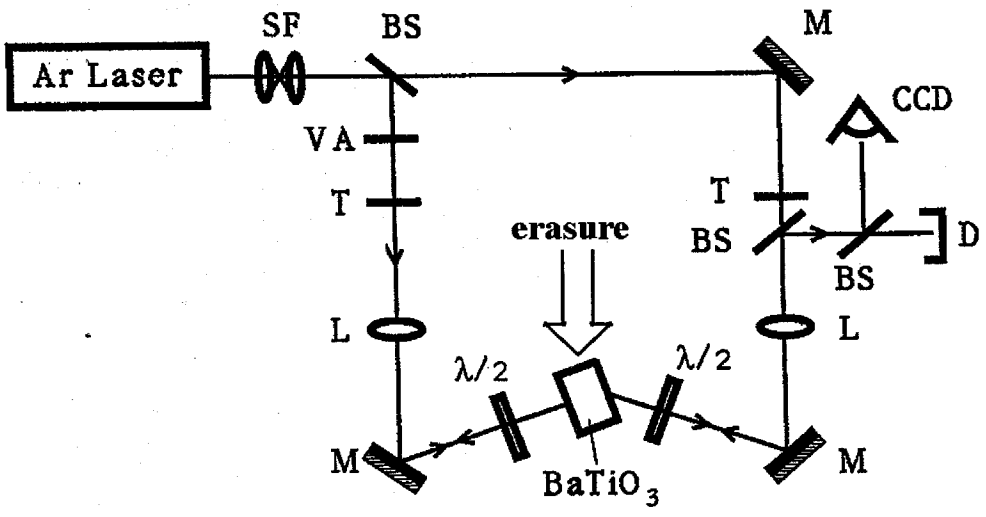

Figure 6.3. Experimental setup for the DPCM studies.

The experimental setup shown in Figure 6.3 consists of an Ar-ion laser, a beam splitter BS, and two transparencies T followed by beam splitters and CCD cameras located on opposite sides of a $BaTiO_3$ crystal. The multimode 488-nm Ar-ion laser with a 3-cm coherence length is polarized in the plane of the optical system (extraordinary polarization). Each beam acquires an image by propagating through a US Air Force resolution chart. After passing through an additional beam splitter and an imaging system, both beams recombine at the $BaTiO_3$ crystal. Care is taken to ensure that the beams are mutually incoherent at the crystal plane (the optical path difference between the arms is much larger than the coherence length). The crystal is placed between the image and the focal planes of the resolution chart so that the transverse intensity distribution in the crystal is nearly uniform. To vary the photorefractive coupling coefficient, we uniformly illuminate the crystal from above with a third, erasure, beam from the Ar-ion laser that is incoherent with respect to the DPCM beams and has ordinary polarization to eliminate fanning of the erase

beam. Changing the intensity of the erase beam varies the visibility of the DPCM interference patterns and hence the modulation depth of the index gratings or the PR coupling coefficient throughout the crystal. We measure the conjugation fidelity and reflectivity of the DPCM, using the backpropagating reflections from the beam splitters in both arms. These reflections are magnified and captured by a CCD camera. When the fidelity of the conjugated images is measured, we use a scanning variable slit across the magnified image plane and measure the transmitted power in different locations. In this manner we are able to compare the conjugation fidelity of the bars of a specific resolution with the original contrast of the resolution chart. The best conjugate image obtained from our DPCM is shown in Figure 6.4 (a). Figure 6.4 (b) shows the magnified central portion of the chart. The best resolution in the phase-conjugate image is 40 μm (across the entire image), limited only by the apertures of our optical components, and the maximum observed phase-conjugate reflectivity is 35%.

An important issue in the operation of the DPCM is the orientation of the structure within the input images with respect to the main plane of interaction (defined by the largest average projection of the gratings and the polarization of the beams). When all the bars in an image are perpendicular to the plane of interaction, Bragg degeneracy results in the formation of conical rings (in the general direction of the bars). This effect cannot be accounted for by the two-dimensional theoretical model [15] and requires a full three-dimensional analysis. We overcome these problems simply by a 45° rotation of the images, which provides grating distributions that are neither parallel or perpendicular to the main plane of interaction. In this respect, our current results never suffer from Bragg degeneracy, and we obtain equal fidelities for bars in both directions. We note another method for suppression of Bragg degeneracy that uses speckles borne on the input beams [16].

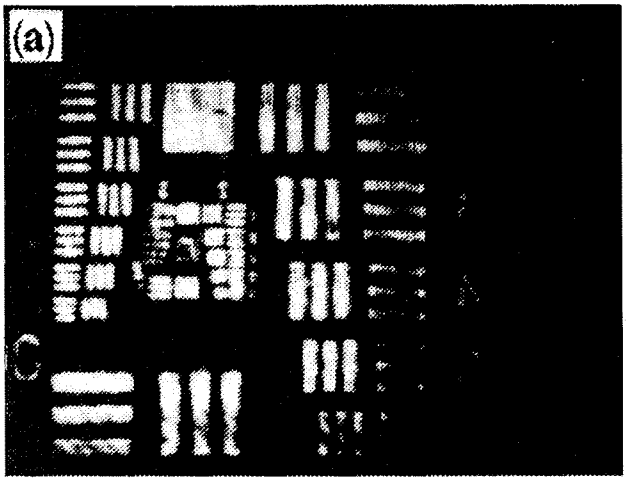

(a)

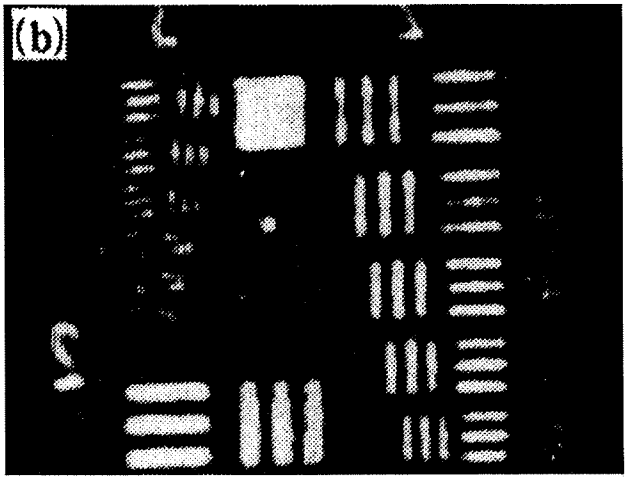

(b)

Figure 6.4. Phase-conjugate images of (a) the entire resolution chart and (b) the inner frame of (a).

In the first experiment we measure the conjugation fidelity and the conjugation reflectivity of a specific group of elements in the image (resolution chart). We concentrated on element #1, group #2, which consists of three bars at the density of 4.00 line pairs/mm

(bar width, 125 μm) in the original image plane. Because in the original image all the bright bars have equal intensities, it is essential to account for the relative intensities in the reconstruction plane. Hence we use a measure for the conjugation fidelity, given by

$$F = \frac{0.5\,(\upsilon_1+\upsilon_3) - \upsilon_2}{\max(\upsilon_1,\upsilon_3) + \upsilon_2}, \qquad 6.16$$

where υ_1, υ_2, and υ_3 are the optical intensities measured in a sequence of bars that are bright–dark–bright in the original image. For example, if the conjugate image is bright-dark-bright, F would be 1; if the conjugate image is bright–dark–dark, F = 1/2; if the conjugate image is reversed (dark–bright–dark), F = -1; and if the conjugate image is bright–bright–bright, F = 0. We point out that F does not equal the conjugation fidelity of [15], although they have similar qualitative behavior (there the fidelity is defined in the Fourier plane, where phases are crucial; here we compare intensity distribution of the original and conjugated images; the slit provided averaging along the bright-dark bars).

The normalized conjugation reflectivity is defined as the intensity integrated over the entire region of the image, $\upsilon_1 + \upsilon_2 + \upsilon_3$, divided by its maximal obtainable value (at the highest available gain). We measure the fidelity and the reflectivity as function of the power of the erasure beam I_e. Since the perturbation in the refractive index is proportional to the visibility of the corresponding interference fringes, the coupling coefficient γ may be rewritten [4] to incorporate the reduction in the visibility resulting from I_e as

$$\gamma(I_e) = \frac{\gamma_0}{1 + (I_e / I_0)}, \qquad 6.17$$

where $I_0 = I_1 + I_2$, I_1 and I_2 are the intensities of the interacting beams and γ_0 is the coupling constant for $I_e = 0$. The PR gain is defined as coupling coefficient γ times the

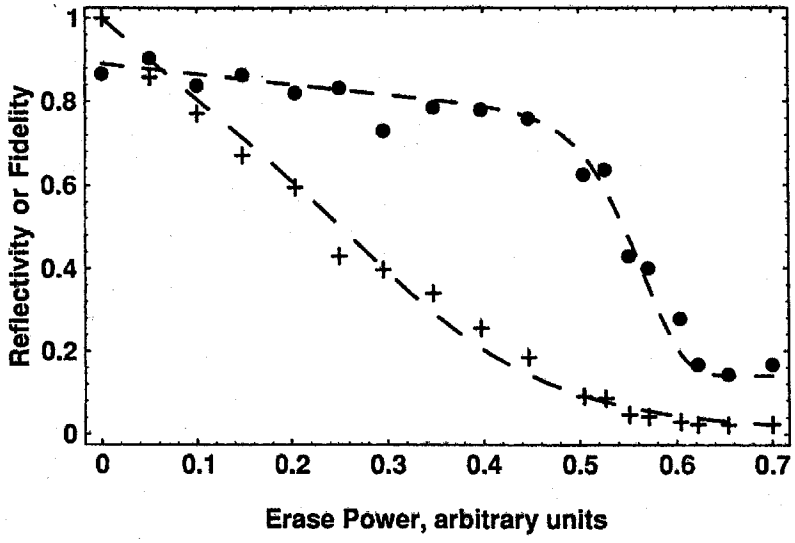

Figure 6.5. Phase-conjugation fidelity (circles) and reflectivity (crosses) as a function the power of the erasure beam. Note the fidelity threshold at erase power of 0.55 a.u. The curves are only a guide to the eye.

interaction length L (in our experiment L = 7 mm). The results shown in Figure 6.5 reveal a sharp fidelity threshold at $I_e = 0.55$ (in arbitrary units). From the optical power of the input beams and the beams' cross sections, we estimate the average I_0 to be roughly 0.32 ± 0.05 (in arbitrary units of the scale of Figure 6.5). We have measured the average coupling coefficient in this configuration by a standard small-signal two wave mixing amplification experiment. This measurement provides a value of 8 cm^{-1}, which gives roughly a gain-threshold value of 2.06 (because beam fanning drives down the value of γ for these measurements, we suspect that the true value is somewhat higher). The conjugation reflectivity, compared with the fidelity, exhibits a smooth behavior. We notice that the reflectivity does saturate at high gains but does not display a threshold behavior as does the fidelity. Intuitively, it is clear that conjugation reflectivity cannot provide accurate data for characterization of the DPCM device, simply because part of this reflection is amplified

noise (fanning), which may be distinguished from the reflectivity of the desired image only by fidelity measurements.

6.4 Conjugation threshold and image resolution

We measure the conjugation fidelity as a function of the resolution (feature size) within the conjugated image. Figure 6.6 shows the conjugation fidelity for two cases: high resolution, 6.36 line pairs/mm (bar width 78.74 μm; element #5, group #2; solid curve) and low resolution, 4.00 line pairs/mm (bar width 125 μm; element #1, group #2; dashed curve). Note that we use the same arbitrary units for I_e in both Figures 6.5 and 6.6. Figure 6.6 clearly shows that the gain threshold value significantly differs in both cases: the lower resolution has a lower threshold value. To emphasize this we show Figure 6.7 with both resolutions conjugated (Figure 6.7(a) maximal gain, $I_e = 0$; Figure 6.7 (b) relatively high gain, small I_e) and only the low resolution conjugated (Figure 6.7 (c) low gain, large I_e).

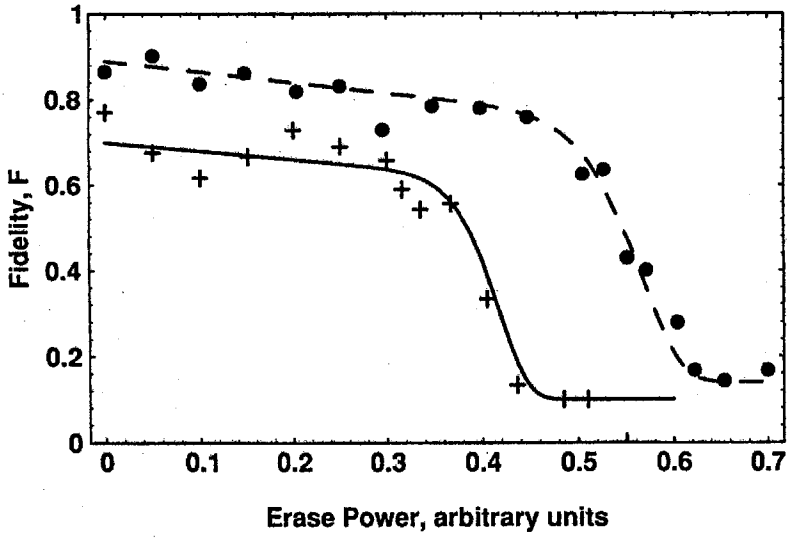

Figure 6.6. Phase-conjugation fidelity as a function the power of the erasure beam for high (crosses) and low (circles) resolutions. The curves are only a guide to the eye.

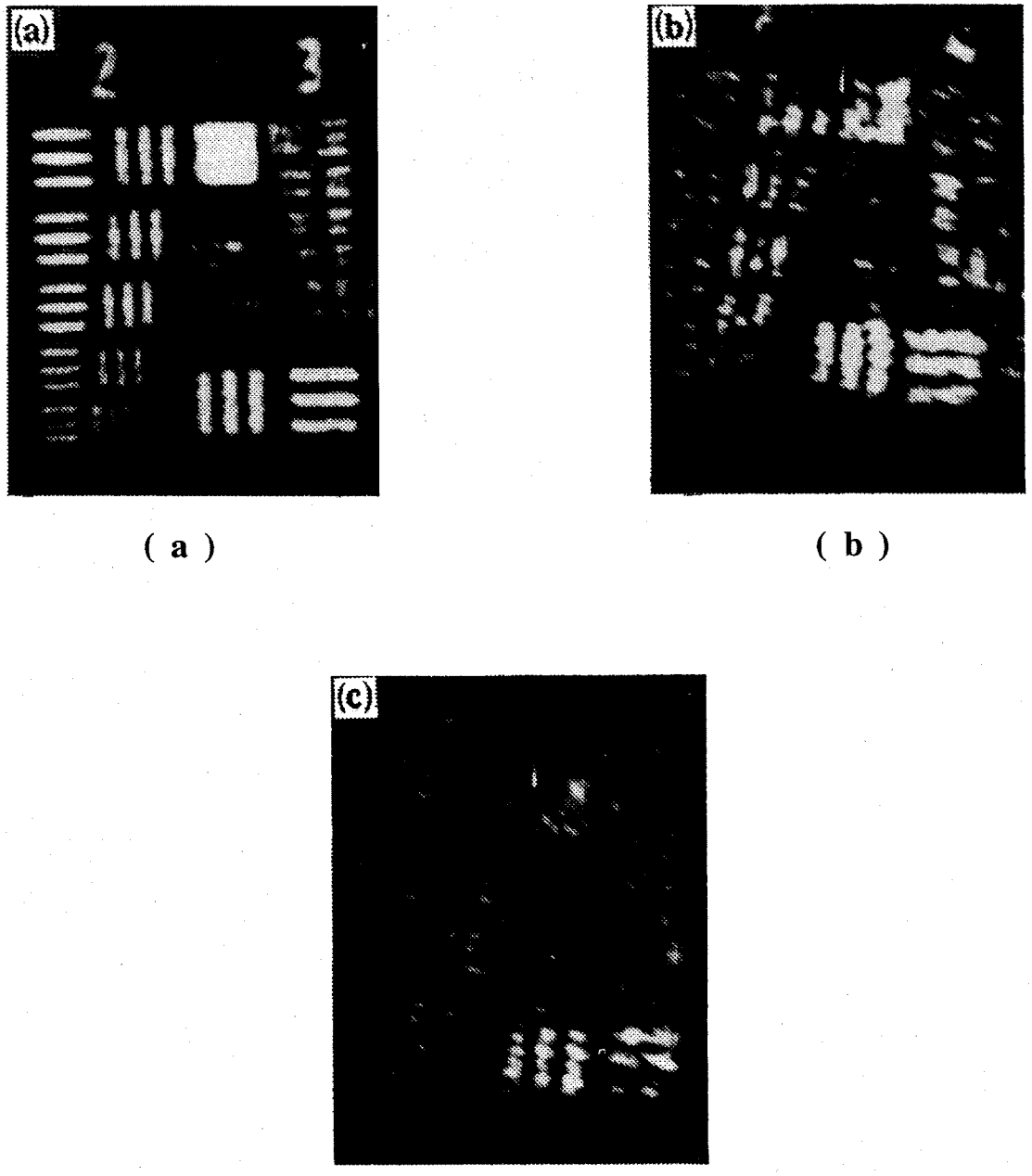

(a) (b)

(c)

Figure 6.7. Phase-conjugate images at (a) maximal, (b) high, and (c) low gain for an input image that contains elements of both resolutions. Note that most of (c) is below threshold.

6.5 Conjugation with unbalanced beams and fidelity degradation

In the third experiment we keep the gain fixed (at $I_e = 0$) but modify the intensity ratio of the input beams from unity to 1:5. In this case we find asymmetry in the conjugation process. Specifically, the stronger beam bleaches the fanning (amplified noise) gratings of the weak beam and permits relatively high conjugation quality on its input side (i.e., high fidelity is obtained for the image originally borne on the strong beam and transferred to the weak beam). The opposite process, however, is inefficient because of the unbalanced process, and the weak beam is not able to eliminate the appearance of fanning gratings, which result in a conjugated image embedded in fanning. This is shown in Figure 6.8. Note the difference between this result on fidelity and the known result [8] (which is present here as well) of an increase in conjugation reflectivity threshold as a result of unequal intensities of the input beams.

6.6 Time response and critical slowing down

We now present experimental results that illustrate the critical slowing down in DPCM. We used the same experimental setup shown in Figure 6.3 with slight modifications: two half-wave plates and a variable beam splitter were inserted in the optical path. In controlling the photorefractive gain, we recall (equation 6.17) that additional illumination, incoherent with both interacting beams, reduces the modulation depth of the interference gratings and, consequently, decreases the resultant perturbation in the refractive index. Since in the current experiment we measure time response, it is essential to maintain the total illumination intensity at a constant value and as uniform as possible across the entire crystal. Since in $BaTiO_3$ the photorefractive coupling is large for the extraordinarily polarized light and almost negligible for the ordinary polarization, in this experiment we control the coupling by varying the polarization of the interacting beams. Thus, the

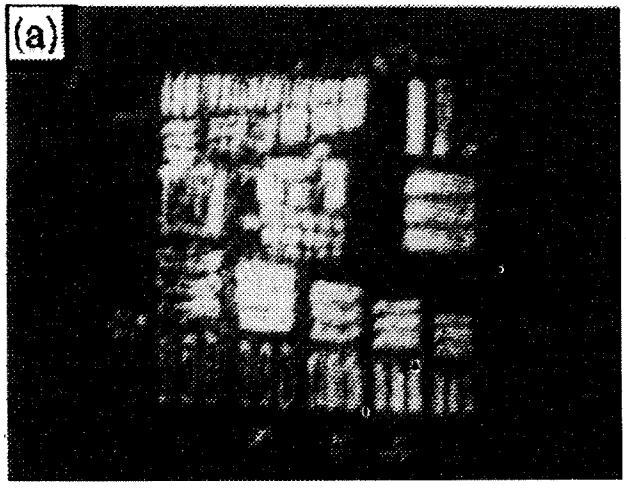

(a)

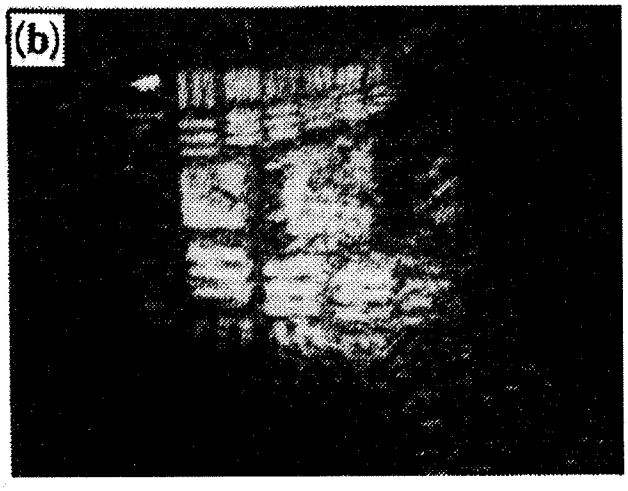

(b)

Figure 6.8. Phase-conjugate images for unbalanced input beams of intensity ratio 1:5: (a) the beam that leaves the face on which the beam of intensity 5 enters (i.e., the phase conjugate replica of the strong beam). (b) the beam that leaves the face on which the beam of intensity 1 enters (i.e., the phase conjugate replica of the weak beam).

ordinarily polarized portion of each beam serves as an erasure beam. Extraordinary polarization provides the highest gain, and ordinary polarization yields minimal gain. The coefficient γ may be expressed [22, 23] as a function of the polarization angle ϕ of the input beams

$$\gamma(\phi) = \frac{\gamma_0}{1 + I_{ord} / I_{ext}} \approx \frac{\gamma_0}{1 + \tan^2\phi}, \qquad 6.18$$

where $\phi = 0$ corresponds to the maximal gain (extraordinary polarization), and I_{ext} and I_{ord} are the sums of the intensities of the extraordinarily and ordinarily polarized beams, respectively. Note that the ordinarily polarized beams do not interact with each other or with the extraordinarily polarized beams, while the extraordinarily polarized beams form the DPCM and transform into each other's phase conjugates. This may result in a different spatial (x and z) dependence of I_{ext} and I_{ord}. Our choice for the interaction plane and the small angle between the beams minimizes this difference, and γ can be well approximated as a function of ϕ only, as in Equation 6.18.

We concentrate on a specific spatial frequency within the image. We block (using an aperture) the phase conjugate reflection of the entire image except for that of three bars (1.26 line pairs/mm). The phase-conjugate reflectivity (normalized to its maximal value of 30%) and the response time in minutes as a function of gain are shown by the triangles and circles in Figure 6.9. The response time reaches its maximal value exactly at the critical point of the reflectivity curve [$(\gamma L)_{th} \approx 2.06$]. The ratio between the response times at the threshold and at the highest gain is about 10. When the aperture is removed and the entire phase conjugate image is captured, we notice two effects. The first is the shift in the threshold value (which is also the gain value at the peak of the response time) toward higher gain levels for the whole phase-conjugate image. This is in accordance with our

previous results [22] that show higher gain threshold values for higher spatial frequencies (section 6.3). The second is the broadening of the response time curve (for the whole image). This is a consequence of the different resolutions of the features incorporated in the Air Force resolution chart. Each spatial frequency in the image has a slightly different threshold, and consequently the response time averages and results in a slightly broader curve than in the single-resolution measurement.

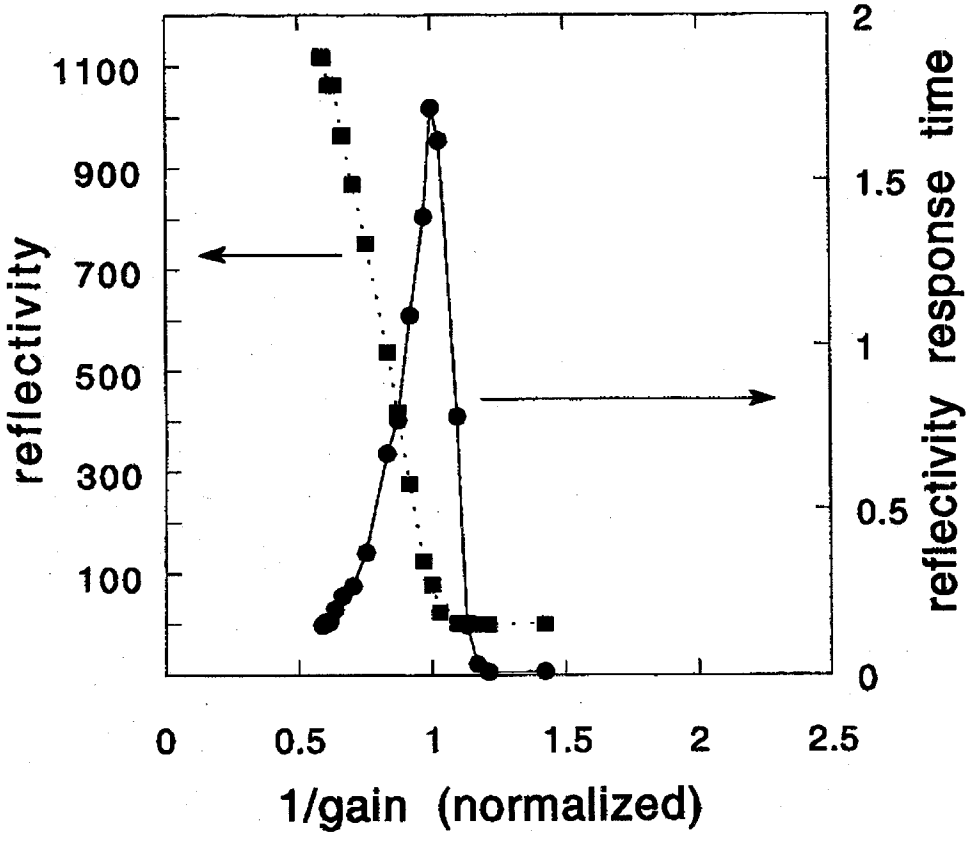

Figure 6.9. Experimental results of the phase-conjugate reflectivity and response time as a function of inverse gain for a single resolution element (1.26 line pairs/mm) of the image. The curves are only a guide to the eye.

To illustrate the change in the angular spectrum when the DPCM goes through its threshold, we show in Figure 6.10 the experimental results (photographs, right column; profile, left column) of the far field pattern (i.e., angular spectrum) of one of the output beams below (upper sections) and above (lower sections) the transition point (threshold). It is evident that the spectrum narrows practically to a single Fourier component, broadened only by the pictorial information borne on the input beam. The behavior of the reflectivity, the response time, and the angular spectrum at the threshold are conclusive experimental evidence that the DPCM is indeed a nonlinear oscillator which undergoes a phase transition at its oscillation threshold point (at $\gamma L \approx (\gamma L)_{th}$) [23].

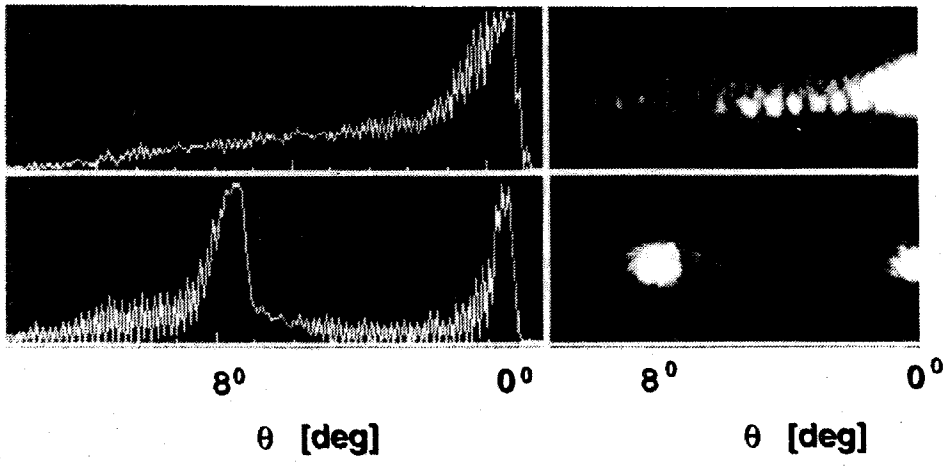

Figure 6.10. The angular spectrum (the far field, photographs, right; averaged intensity profiles, left) of one of the output beams below (upper section) and above (lower section) the transition point (gain threshold). The intensity of the small features in the upper right photograph is much smaller than the single (phase conjugate) peak in the lower right photograph.

6.7 Two-dimensional model of the DPCM

In this section we describe briefly the major results and basic formulation of the two-dimensional theory of DPCM [14, 15]. The model is based on decomposition of the image bearing interacting beams into a discrete set of the free space eigenmodes (plane waves) and perturbation analysis of the mode-coupling arising due to the photorefractive nonlinear index perturbation.

The total electric field of the electromagnetic wave in the crystal is decomposed into a sum of two counterpropagating beams whose slowly varying amplitudes are A(x,z,t) and B(x,z,t) (A includes the pair $\{A_1, A_4\}$ and B includes the pair $\{A_2, A_3\}$ of Figure 6.1):

$$\mathbf{E}(x,z,t) = 1/2\left(A(x,z,t)\exp(ikz-i\omega t) + B^{*}(x,z,t)\exp(-ikz-i\omega t) + c.c.\right)\hat{x}\,, \qquad 6.19$$

where $\hat{x}$ is the unit vector in the transverse direction. The small deviation of the propagation angle from 180° is accounted for in the slowly varying envelope. The slowly varying amplitudes A and B are further expanded in the basis of the eigenmodes of the free space (plane waves) about the nominal propagation direction z:

$$A(x,z,t) = \Sigma_m\, a_m(z,t)\exp\left(-ik\varepsilon mx - ik\varepsilon^2 m^2 z/2\right), \qquad 6.20$$

$$B(x,z,t) = \Sigma_m\, b_m(z,t)\exp\left(ik\varepsilon mx + ik\varepsilon^2 m^2 z/2\right), \qquad 6.21$$

where ε is the small angular difference between the two adjacent plane waves and a_m and b_m are the (complex) expansion coefficients. The (transmission) photorefractive grating $\Delta n(x,z,t)$ can be recorded only due to the mutually coherent copropagating plane wave components and, therefore, $\Delta n(x,z,t)$ can be expanded as

$$\Delta n(x,z,t) = \Sigma_{m,n}\, \delta n_{mn}(z,t)\, \exp\left(-ik(m-n)\varepsilon x - ik\varepsilon^2(m^2 - m^2)z/2\right). \qquad 6.22$$

The temporal and spatial evolution of the expansion coefficients δn_{mn} is governed by the standard equations for the grating formation in photorefractive materials [25] and is described by the following set of coupled nonlinear differential equations

$$\tau_{mn} I_d \frac{\partial \delta n_{mn}(z,t)}{\partial t} + (I_0 + I_d)\, \delta n_{mn}(z,t) = i\gamma_{mn}\left(a_m(z,t) a_n^*(z,t) + b_n(z,t) b_m^*(z,t)\right), \qquad 6.23$$

where $I_0 = \Sigma_m\, a_m a_m^* + b_m b_m^*$ is the total light intensity which is assume to be constant throughout the crystal volume (energy conservation invariant) and τ_{mn} and γ_{mn} are the grating formation time (normalized to the background irradiance I_d) and coupling constants, respectively, for a specific grating spacing due to m's and n's copropagating plane wave component. The master equations for the amplitude expansion coefficients can be obtained by inserting the expressions for the field amplitudes (equations 6.20,21) and $\Delta n(x,z,t)$ (equation 6.22) into the wave equation 6.3, invoking the paraxial approximation, and neglecting the non phase matched terms in the wave equation [14]. These result in [15]

$$\frac{\partial a_m(z,t)}{\partial z} = ik\Sigma_n\, \delta n_{mn}(z,t)\, a_n(z,t), \qquad 6.24$$

$$\frac{\partial b_m(z,t)}{\partial z} = -ik\Sigma_n\, \delta n_{nm}(z,t)\, b_n(z,t). \qquad 6.25$$

The systems of differential equations 6.23, 6.24, and 6.26 constitute the mathematical model of the DPCM. These are solved numerically [15] using the appropriate initial and boundary conditions, where the letter includes the two input beams as well as weak time-independent seeding with random phase and amplitude.

6.8 Basic results and limitations of the two-dimensional perturbation analysis

The numerical analysis [15] of the model establishes the fact that the conjugation fidelity and reflectivity have significantly different dependencies on the gain. These differences are particularly large near the threshold. Figure 6.11 shows the steady-state conjugation fidelities for both beams and the conjugate reflectivity as a function of gain. Here the two beams possess different phase and amplitude information but have equal total intensities. The model also predicts that the fidelity and reflectivity have largely different time dependence: well above the threshold the phase conjugate beams reach high fidelity while their intensities (i.e., reflectivity) continues to grow in time.

The numerical analysis also predicts that for the case of unbalanced input beams (i.e., the intensities ratio is not unity) the conjugation becomes asymmetric. At a given gain value the phase conjugate replica of the weaker beam has lower conjugation fidelity than the phase conjugate of the stronger beam. Besides, the conjugation fidelity threshold on the side of the weaker beam is shifted toward higher gain values [15, Figures 11 and 12].

The model characterizes the DPCM as a nonlinear oscillator which exhibits a critical slowing down in the vicinity of the threshold (Figure 6.12). The critical slowing down becomes less pronounced as the amplitude of seeding is increased or the intensities ratio differs significantly from unity . At the same time the phase conjugate reflectivity does not depend on the seed amplitude if the nonlinear gain is well above its threshold value. Moreover, in this case the phase conjugation process is self-sustained if the seeding is turned off (set to zero) after the oscillation establishes itself.

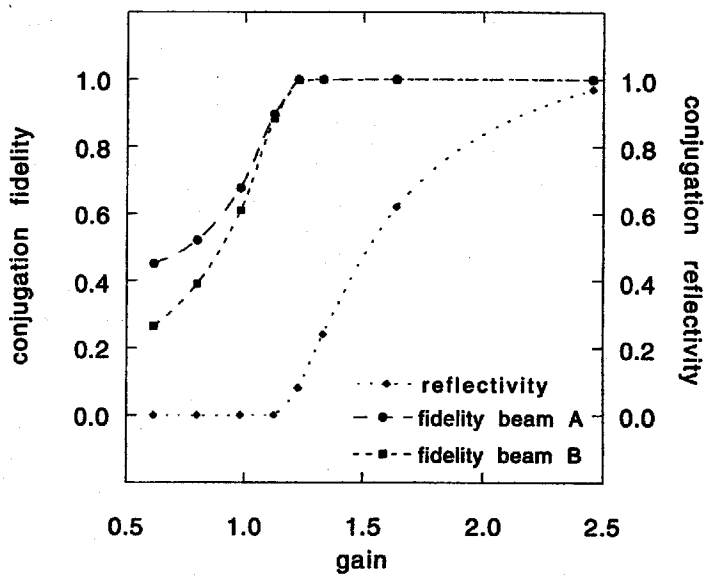

Figure 6.11. Calculated conjugation fidelities for both beams and the conjugation reflectivity as a function of gain (normalized).

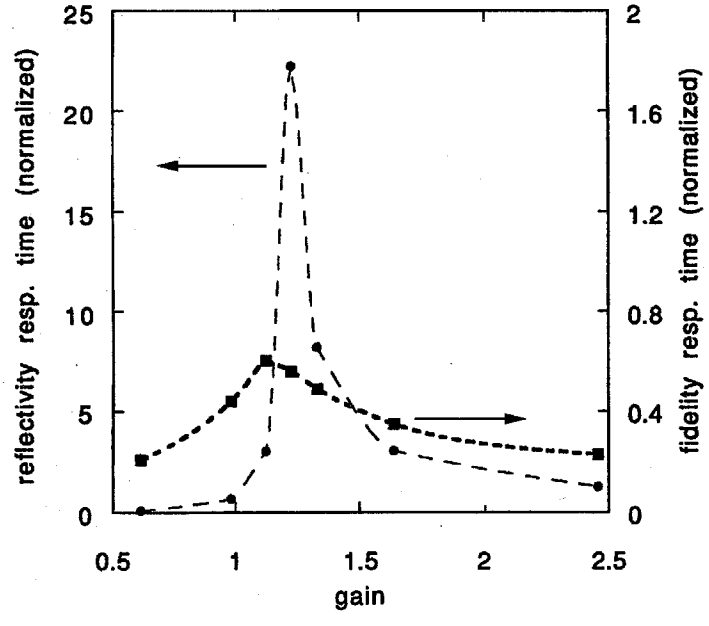

Figure 6.12. Calculated response times of the conjugation fidelity (curves with squares) and of the conjugation reflectivity (curves with points) as a function of gain.

Basic predictions of the two-dimensional theory of the DPCM (the different behavior of fidelity and reflectivity versus gain, the fidelity degradation for unbalanced beams, and the critical slowing down in the vicinity of the threshold) are in a good qualitative agreement with the results of the experimental study (sections 6.3-6.6). The limitation of the current model can be understood if we recall that the theory is essentially based on the rigorous perturbation analysis of the wave equation 6.3. The eigenfunctions used in the plane wave expansions 6.20, 6.21 are the eigenfunctions (plane wave modes) of the homogeneous wave equation 6.3 with no nonlinear inhomogeneous index perturbation (i.e., when $\Delta n(x,z,t) \equiv 0$). The nonlinear index change is considered as a weak perturbation, which leads to the coupling between the initially orthogonal plane wave eigenmodes (as described by equations 6.24 and 6.25) and, eventually, to the excitation of the phase conjugate replica. As any perturbation theory approach [26] the approach used for the analysis of the DPCM is self-consistent only as long as the mode coupling and eigenmodes perturbation can be considered weak compared to the unperturbed state. The latter translates into the condition that the expansion coefficients a_m and b_m in equations 6.20, 6.21 don't change much upon the propagation through the crystal (i.e., the coupling between plane wave eigenmodes is weak). This situation is realized only when the conjugate reflectivities R are low ($R << 1$), i.e., when the DPCM is near or below its threshold. Another limitation arises from the use of the paraxial approximation what limits the angle between the interacting beams inside the crystal (as well as their angular extent) to approximately 10-15°. Under these certain and restricted conditions (often realizable in the experiments, however) the presented theory represents an adequate treatment of the double phase conjugation in photorefractive materials.

6.9 Summary

The double phase conjugate mirror is a photorefractive device in which two mutually incoherent beams create phase conjugate replicas of each other. The DPCM exhibits a sharp conjugation fidelity threshold, while the reflectivity is a smoothly increasing function of the gain. The gain threshold for the conjugation fidelity increases with increasing resolution of the image. Phase conjugation with amplification is possible in DPCM, but the conjugation fidelity of the weak beam's conjugate replica degrades dramatically, when the intensity ratio is increased. The DPCM exhibits critical slowing down (i.e., dramatic increase of the response time) in the vicinity of the oscillation threshold. The basic predictions of the two-dimensional coupled-modes perturbation analysis of the DPCM are in a good qualitative agreement with the results of the experimental study.

References for Chapter Six

[1] A. Yariv, *Optical electronics*, 3rd edition, (Holt, Rinehart, and Winston, New York, 1985).

[2] J. O. White, M. Cronin-Golomb, B. Fischer, and A. Yariv, Appl. Phys. Lett. **40**, 450 (1982).

[3] J. Feinberg and R. W. Hellwarth, Opt. Lett. **5**, 519 (1980).

[4] M. Cronin-Golomb, B. Fischer, J. O. White, and A. Yariv, IEEE J. Quant. Electron., QE-**20**, 12 (1984).

[5] J. Feinberg, Opt. Lett. **7**, 486 (1982).

[6] R. A. McFarlane and D. G. Steel, Opt. Lett. **8**, 208 (1983).

[7] S.-K. Kwong, M. Cronin-Golomb, B. Fischer, and A. Yariv, IEEE J. Quant. Electron., QE-**22**, 1508 (1986).

[8] S. Weiss, S. Sternklar, and B. Fischer, Opt. Lett. **12**, 114 (1987).

[9] S. K. Kwong, G. A. Rakuljic, and A. Yariv, Appl. Phys. Lett. **48**, 201 (1986).

[10] R. J. Anderson, E. J. Sharp, G. L. Wood, W. W. Clark, Q. Vuong, G. J. Salamo, and R. R. Neurgaonkar, Opt. Lett. **18**, 986 (1993).

[11] A. Chiou, P. Yeh, C. Yang, and C. Gu, Opt. Lett. **20**, 1125 (1995).

[12] J. Feinberg, Opt. Lett. **8**, 569 (1983).

[13] S. Sternklar, S. Weiss, M. Segev, and B. Fischer, Opt. Lett. **11**, 528 (1986).

[14] M. Segev, D. Engin, A. Yariv, and G. C. Valley, Opt. Lett. **18**, 956 (1993).

[15] D. Engin, M. Segev, S. S. Orlov, A. Yariv, and G. C. Valley, J. Opt. Soc. Am. B **11**, 1710 (1994).

[16] A. V. Mamaev and V. V. Shkunov, Sov. J. Quantum Electron. **22**, 1036 (1992).

[17] O. V. Łyubomudrov and V. V. Shkunov, Sov. J. Quantum Electron. **22**, 1027 (1992).

[18] B. Ya. Zeldovich, N. F. Pilipetsky, and V. V. Shkunov, *Principles of Phase Conjugation* (Springer-Verlag, Heidelberg, 1985).

[19] A. A. Zozulya, Opt. Lett. **16**, 545 (1991).

[20] N. V. Bogodaev, V. V. Eliseev, L. I. Ivleva, A. S. Korshunov, S. S. Orlov, N. M. Polozkov, and A. A. Zozulya, J. Opt. Soc. Am. B **9**, 1493 (1992).

[21] A. A. Zozulya, M. Saffman, and D. Z. Anderson, J. Opt. Soc. Am. B **12**, 255 (1995) and references therein.

[22] S. S. Orlov, M. Segev, A. Yariv, and G. C. Valley, Opt. Lett. **19**, 578 (1994).

[23] D. Engin, S. S. Orlov, M. Segev, G. C. Valley, and A. Yariv, Phys. Rev. Lett. **74**, 1743 (1995).

[24] V. V. Eliseev, V. T. Tikhonchuk, and A. A. Zozulya, J. Opt. Soc. Am. B **8**, 2497 (1991).

[25] N. V. Kukhtarev, V. B. Markov, S. G. Odoulov, M. S. Soskin, V. L. Vinetskii, Ferroelectrics **22**, 949, 961 (1979).

[26] see, for example, L. Landau and E. Lifshitz, *Quantum Mechanics: Non-relativistic Theory*, 3rd edition (Pergamon Press, New York, 1977).

Chapter Seven

Nonlinear Self-Phase Matching of Optical Second Harmonic Generation in Lithium Niobate

7.1 Introduction

The nonlinear response of the material to excitation by the field of the electromagnetic waves can give rise to exchange of energy between waves of different frequencies. The optical second harmonic generation (SHG) is a process in which an optical wave with frequency ω induces a polarization wave with double that frequency within a nonlinear optical media. This induced nonlinear polarization radiates an optical wave with frequency 2ω. The SHG process is most efficient if the polarization wave travels with the same phase velocity as the electromagnetic wave of frequency 2ω. The latter condition is called the phase matching, or equivalently, momentum conservation condition. Different techniques for phase matching the nonlinear interactions of optical beams have been developed including the birefringent phase matching [1] and quasi-phase matching [2-4] using an alternating sign optical nonlinearity. This chapter describes how large photorefractive nonlinearity affects the phase matching conditions for optical SHG and demonstrates that the large index perturbation due to photovoltaic and photorefractive effects (originally called

"optical damage" [5, 6]) in lithium niobate can promote a new type of phase matching, namely, the nonlinear self-phase matching of (initially not phase matched) SHG [7].

7.2 Phase matching in nonlinear optical interactions

The nonlinear electromagnetic response of the medium is described by an expansion of the induced polarization $P_i(t)$ in powers of the electric field amplitude E [8]:

$$P_i(t) = \varepsilon_0 \chi_{ij} E_j + d_{ijk} E_j E_k + 4\chi^{(3)}_{ijkl} E_j E_k E_l + \dots \quad . \tag{7.1}$$

The term $d_{ijk} E_j E_k$ describes the second-order optical nonlinear effects which include the second harmonic generation, sum and difference frequency generation, optical rectification, and electrooptic effect. In the degenerate case of the second harmonic generation the expansion 7.1 reduces to

$$P_i^{2\omega} = d_{ijk}^{2\omega,\omega,\omega} E_j^{\omega} E_k^{\omega} , \tag{7.2}$$

where $P_i^{2\omega}(z)$ and $E_k^{\omega}(z)$ are corresponding slowly varying amplitudes. The plane wave coupled waves equation describing the evolution of the second harmonic amplitude as it passes through the nonlinear medium is given by [8]

$$\frac{\partial E_i^{2\omega}(z)}{\partial z} = -i\omega \sqrt{\frac{\mu}{\varepsilon}}\, d_{ijk}^{2\omega,\omega,\omega} E_j^{\omega}(z) E_k^{\omega}(z) \exp(i \Delta k\, z) , \tag{7.3}$$

where Δk is the wavevector mismatch which (in collinear case $\mathbf{k}^{2\omega} \parallel \mathbf{k}^{\omega}$) is given by

$$\Delta k = \left| \mathbf{k}^{2\omega} - 2\mathbf{k}^{\omega} \right| = \frac{2\omega}{c} (n^{2\omega} - n^{\omega}) . \tag{7.4}$$

The solution of equation 7.3 for $E^{2\omega}(0) = 0$ and for a crystal of length L is [1]

$$I^{2\omega}(L) = 8\left(\frac{\mu_0}{\varepsilon_0}\right)^{3/2} \frac{\omega^2 (d_{eff}^{2\omega,\omega,\omega})^2 L^2}{n^3} (I^{\omega})^2 \frac{\sin^2(\Delta kL/2)}{(\Delta kL/2)^2}, \qquad 7.5$$

where $I^{2\omega}$ and I^{ω} are the intensities of the second and fundamental harmonics respectively.

According to equation 7.5, a prerequisite for efficient second harmonic generation is that $\Delta k = 0$, or equivalently $n^{2\omega} = n^{\omega}$. The technique that is used widely [1] takes advantage of the natural birefringence of anisotropic crystals. In normally dispersive materials, the index of both the ordinary and the extraordinary waves increase with optical frequency, which makes it to achieve the index matching if both waves have the same polarization. However, if the birefringence of the crystal is large enough, the phase matching can be achieved by using two copropagating waves of different type: one extraordinary and one ordinary. For the case of a *negative* (i.e., $n_e < n_o$) uniaxial crystal the condition $\Delta k = 0$ can be written as

$$n_e^{2\omega}(\theta_m) = n_o^{\omega}, \qquad 7.6$$

where θ_m is the phase matching angle (here θ is defined as the angle between the optical axis and the polarization direction of the extraordinary wave, i.e., $n_e(0^\circ) = n_e$, $n_e(90^\circ) = n_o$). If the birefringence of the crystal is not sufficiently large (this is the case, for example, for second harmonic generation at 1.064 μm in congruent lithium niobate, in which $n_e^{0.532\,\mu m} - n_o^{1.064\,\mu m} \cong 0.002$ [9]), the condition 7.6 can't be satisfied and one has to resort to, e.g., quasi-phase matching techniques [2-4].

Another possibility to provide the phase matching (at least, *locally*) is to use the optical nonlinearity to make up for the insufficient natural birefringence, i.e., provide $n_e^{2\omega} + \delta n_{NL,e}^{2\omega} = n_o^{\omega} + \delta n_{NL,o}^{\omega}$, where δn_{NL} is the induced nonlinear index change (e.g., due to the optical Kerr effect, or photorefractive effect). The mechanism of the index change in

photorefractives is due to the redistribution of photoexcited (usually, by the visible light) electrons between the traps, buildup of the internal space charge field $E_{sc}(\mathbf{r})$, and electrooptic effect. Unlike *electronic* nonlinearities, the photorefractive mechanism is usually very slow (typical response time is from 1 ms to 100 s), but the index change can be as large as 10^{-3}. In the presence of the dc internal space charge electric field the phase matching condition 7.6 is modified and can be expressed as follows

$$n_e^{2\omega}(\mathbf{r}, \theta_m) \cong n_e^{2\omega}(\theta_m) - \frac{r_{e,2\omega}^{eff} n_e^3}{2} E_{sc}(\mathbf{r}) = n_o^{\omega}(\mathbf{r}) \cong n_o^{\omega} - \frac{r_{o,\omega}^{eff} n_o^3}{2} E_{sc}(\mathbf{r}), \qquad 7.7$$

where r^{eff} is the effective electrooptic coefficient and it is assumed that θ is relatively small ($\theta \approx 0°$). Due to the spatial dependence of the space charge field the phase matching conditions can be satisfied (or, at least, improved significantly) only in the vicinity of the interaction volume of the two optical beams, rather than in the whole volume of the crystal. Besides, the spatial variations of the indices of refraction 7.7 may give rise to the spatial self-phase modulation of the beams (e.g., self-defocusing or self-focusing). The schematic diagram of the nonlinear self-phase matching of second harmonic generation in photovoltaic lithium niobate is depicted in Figure 7.1. Section 7.3 describes the experimental study of the effect, and Section 7.4 analyzes the spatial profile of the nonlinear index change and effect of the spatial self-phase modulation on the transverse structure of the second harmonic beam.

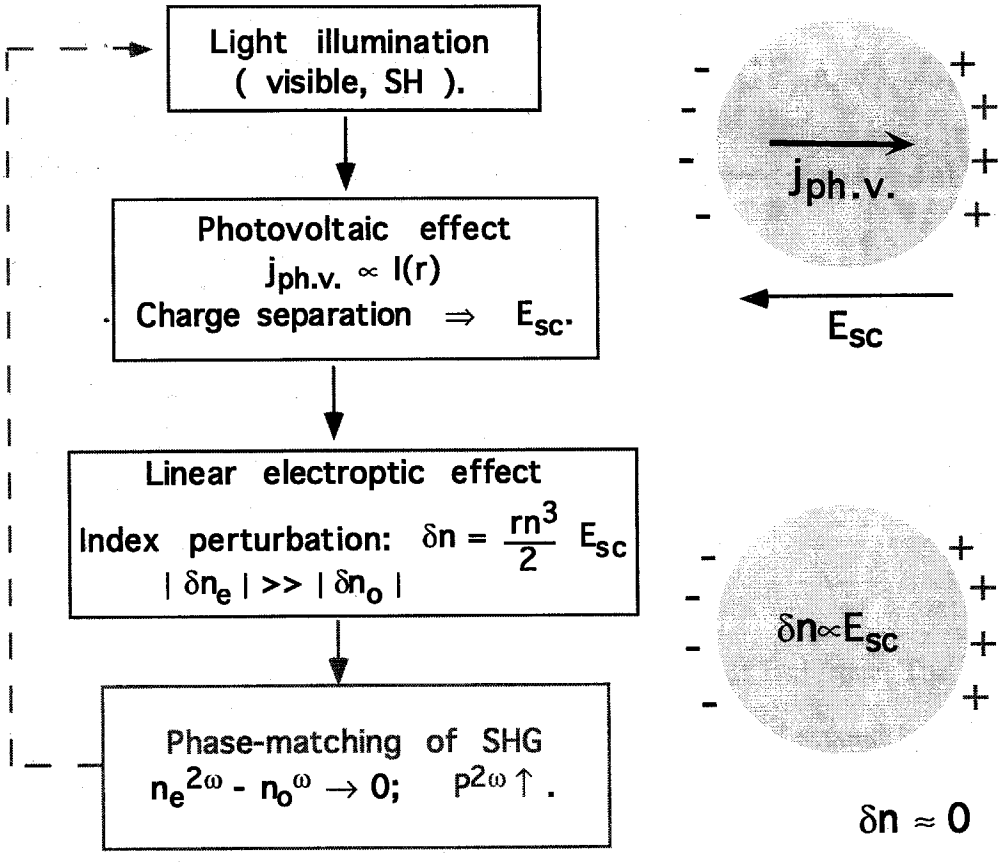

Figure 7.1. Schematic diagram of nonlinear self-phase matching of optical second harmonic generation in photorefractive/photovoltaic lithium niobate.

7.3 Experimental study of nonlinear self-phase matching in photorefractive lithium niobate

The experimental setup is shown in Figure 7.2. As an optical source, we employ a Q-switched (repetition rate 1 kHz) mode-locked (50 MHz) Nd:YAG laser (λ = 1.064 μm), emitting 8-10 mode-locked 100 ps pulses within the Q-switched envelope. The ordinarily polarized infrared radiation is focused with a 50 mm focal length lens on a lightly Fe-doped

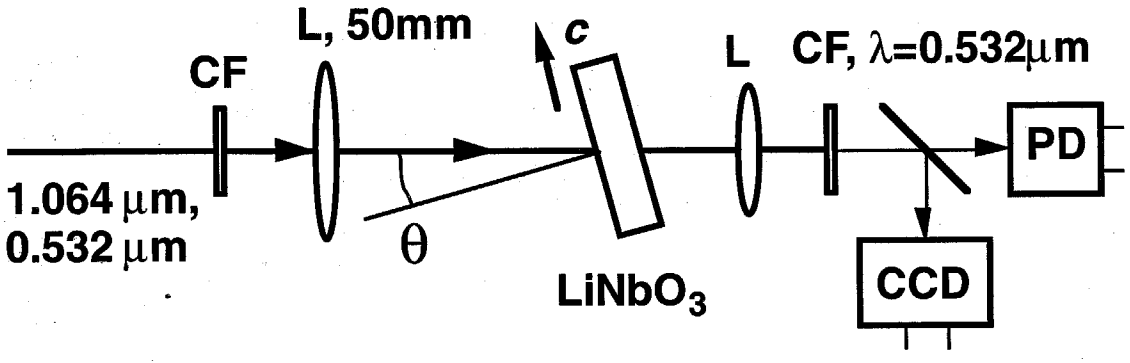

Figure 7.2. Experimental set-up. L is a lens, PD is a photodetector, CF's are appropriate color filters.

2 mm thick $LiNbO_3$ crystal, the *c*-axis of which is in the plane of incidence. The focal spot size of the infrared beam is ~70 μm. The extraordinarily polarized second harmonic light ($\lambda = 0.532$ μm) emerging from the far side of the crystal is captured by a CCD camera and its total CW power is measured with a photodetector.

We observe that for relatively small angles of incidence (between 0° and approximately 20°) of the fundamental light the second harmonic signal increases with time (Figure 7.3) by a factor ~100 from a few μW to several mW average power (up to 0.1% in conversion efficiency). The enhancement in the SH power is accompanied by a pattern formation in the spatial structure of the SH beam (Figure 7.4). The SH beam first becomes elongated along the direction of the *c*-axis of the crystal, has two distinct sidelobes in the intermediate stage (Figure 7.4(b)), and eventually settles into the pattern of Figure 7.4(c). At the same time, the ordinarily polarized infrared beam does not experience substantial phase distortion, as seen from its far field pattern, which remains roughly a Gaussian. The enhancement in the SHG can also be induced by the 0.532 μm seeding beam alone. If a spot previously

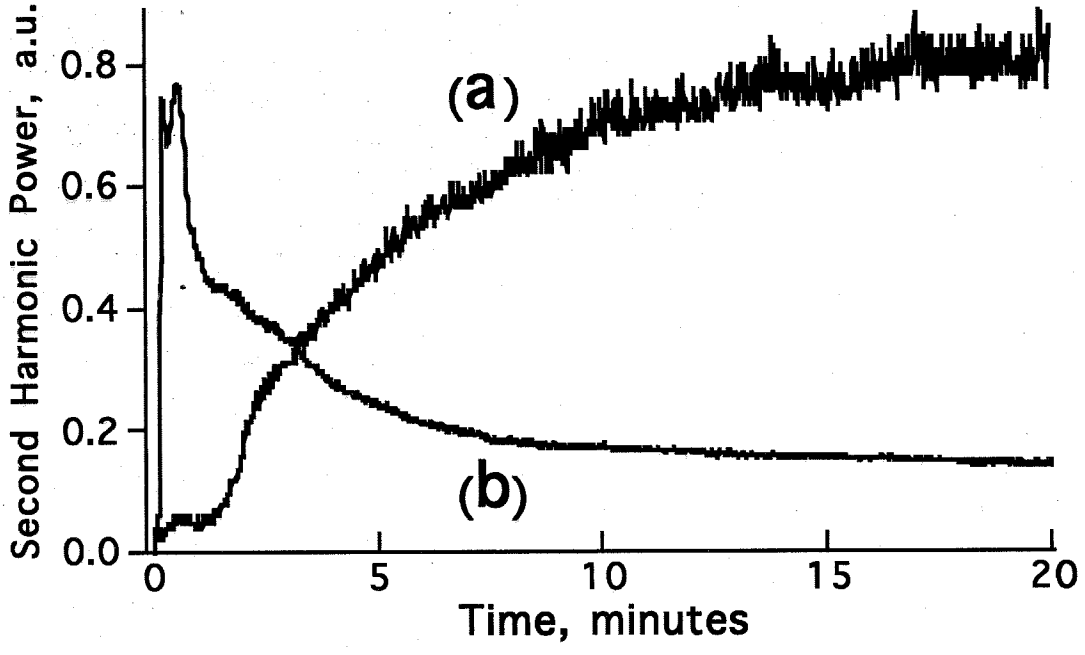

Figure 7.3. Growth of the second harmonic signal with time (a) for $\theta = 16°$ angle of incidence, (b) for normal incidence. Optical power at 1.064 μm is 1.5 W.

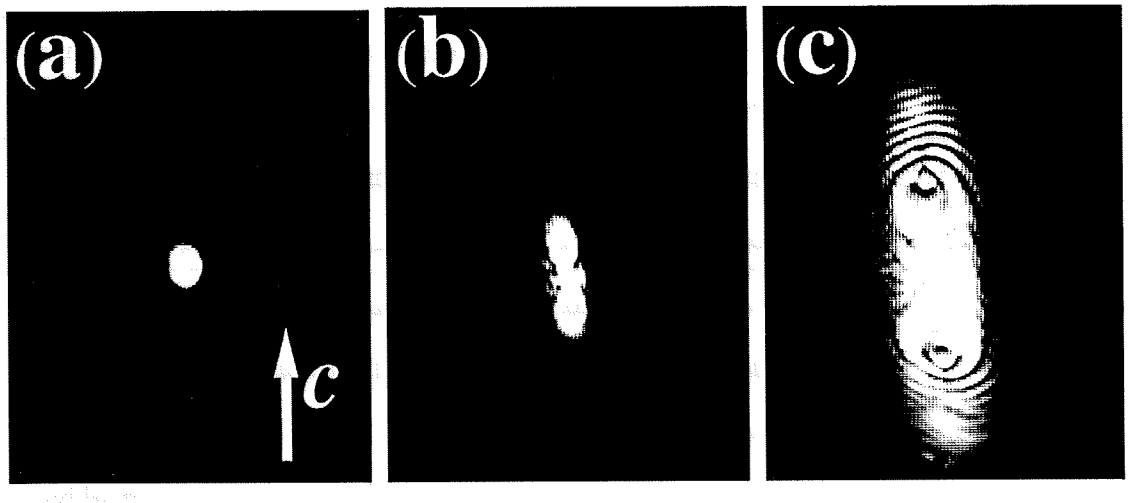

Figure 7.4. Far-field of the generated SH beam in a 2 mm crystal (a) at the beginning of exposure, (b) intermediate stage, (c) at saturation (total far-field angle of the beam in the *c*-axis plane is ~25°).

exposed to the externally injected seeding SH light (focused with the same lens) is probed by the infrared light the initially (t=0) generated SH signal is significantly (50-100 times) higher and the time for the SH signal to reach the final steady-state intensity is shorter than in a "fresh" spot. This is in contrast to the self-induced SHG in glass fibers [10] where the simultaneous presence of the fundamental and SH (either self-induced or injected) light is required by the nature of the $\chi^{(3)}$ coherent photovoltaic effect [11]. The photoinduced index changes persist for prolonged periods of time when the crystal is kept in the dark, but can be completely erased optically by homogeneous prolonged illumination with visible or UV light. This, along with the anisotropy of the SH far-field pattern (Figure 7.4) indicate that the effect is not of thermal origin (since thermally induced refractive index changes are isotropic [12, 13]). Furthermore, the index mismatch for SHG at 1.064 μm increases with temperature in congruent $LiNbO_3$, thus, temperature increase cannot phase match or enhance the SHG process.

The origin of the self-phase matching effect is the photovoltaic field induced by the second harmonic light (initially not phase matched) which via conventional electrooptic effect *locally* changes the birefringence of the crystal to provide (or improve significantly) the index matching, resulting in the increase of the generated SH power. Fe-doped $LiNbO_3$ has very low photosensitivity in the near infrared but exhibits strong photovoltaic response in the visible range (for $\lambda \leq 0.5$ μm). The maximal optically induced perturbation (negative by sign) in the extraordinary index of refraction is typically ~0.001 and is larger the higher the light intensity [14, 15], which is consistent with the mismatch value [9] $\Delta n = n_e^{2\omega} - n_o^{\omega} \cong 0.002$ for SHG at $\lambda = 1.064$ μm. The far-field pattern (Figure 7.4(b,c)) is caused by the spatial self-phase modulation (self-defocusing) owing to the nonlinear index change induced due to the photovoltaic field by the nonuniform spatial profile of the SH beam. The pattern differs from the conventional picture of conical rings (typical for spatial

self-phase-modulation of isotropic origin [12, 13]) because of the anisotropy of the index perturbation arising due to photovoltaic effect, which results in preferential scattering of the SH beam in the *c*-axis plane. This is analyzed in more detail in the next Section.

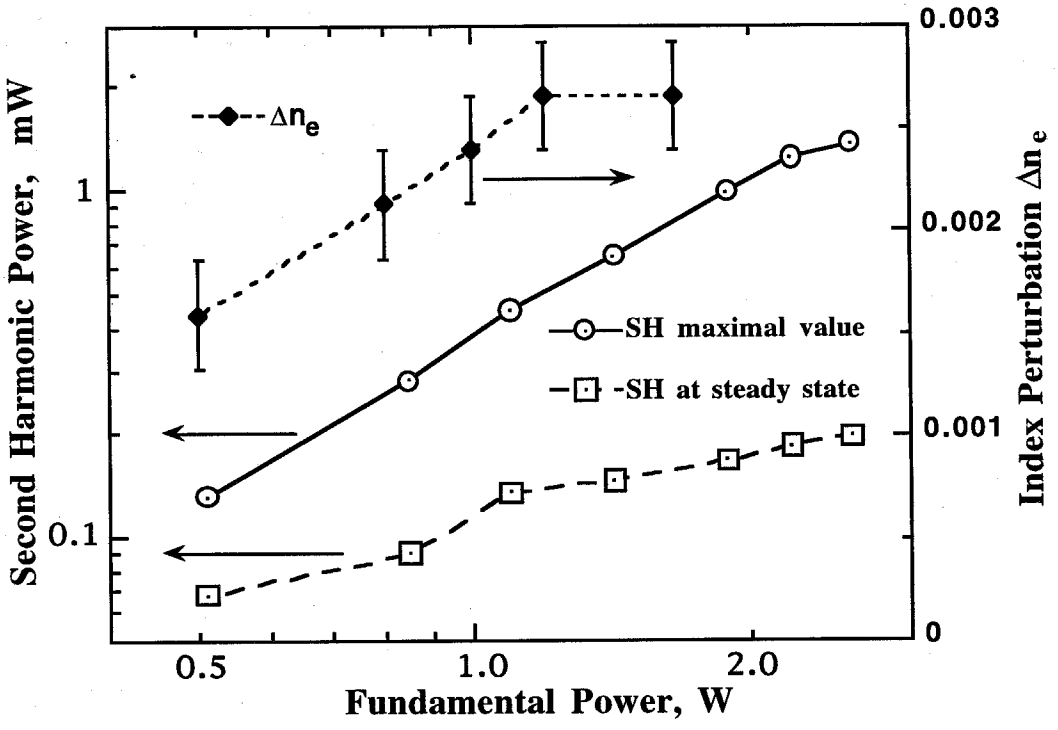

Figure 7.5. Second harmonic power at steady state (after 2000 sec of exposure) and at maximum, and the magnitude of the extraordinary index change Δn_e vs. the incident power of the fundamental beam (normal incidence, $\theta=0°$).

The magnitude of extraordinary index change is estimated using an approximate formula [12] $\Delta n_e L \approx N\lambda$, where N is the number of the orders of diffraction (interference fringes), observed in the far-field, and L is the length of the crystal (Figure 7.5). From Figure 7.4(c) we obtain $N \approx 9$ and, therefore, $\Delta n_e \approx -2.6\times10^{-3}$. The perturbation in the ordinary index for the fundamental light is much smaller since $r_{13}^{1.064\,\mu m}/r_{33}^{0.532\,\mu m} \cong 0.2$ in

$LiNbO_3$. This explains the absence of patterns in the far-field of the infrared beam. The Δn_e changes with input power (see Figure 7.5) indicating that in the range of SH intensities achieved in the experiments, the photovoltaic field is essentially intensity dependent [14, 15]. Therefore, the extraordinary index change and, thus, the phase matching conditions are different for different input powers. This explains the deviation of the SH power in the steady state from the expected square law $P^{2\omega} \propto \left(P^{\omega} \right)^2$. In general, the temporal evolution of the SH signal is not a simple exponent (see Figure 7.3, curve (b)), however, the characteristic response time τ of the buildup process, defined as the time required for the SH signal to reach a half of its maximum value, scales with input power as $\tau \propto \left(P^{\omega} \right)^{-2.4 \pm 0.2}$, when other parameters are kept the same.

For a particular initial index mismatch the generated photovoltaic fields may be larger than required to achieve the ideal phase-matching, i.e. in some cases the light-induced index change over-compensates. This results in the decrease of the SH power after its initial rapid buildup (Figure 7.3, curve (b)). The SH signal does not return to a near zero value due to the strong defocusing channel induced in the medium. Part of the non ideally phase-matched second harmonic leaves the interaction region before being converted back to the fundamental beam. This is somewhat analogous to the Cherenkov-type SHG in waveguides [16]. The SHG process can be optimized by adjusting the initial (t=0) index mismatch of the interacting waves at any particular input power level. Figure 7.6 shows such *angular* tuning curve for SHG. The optimal angle of incidence (14° in the conditions of Figure 7.6) may differ for other Fe-doping concentrations, temperatures, and may also depend on input intensity. Using Sellmeier equation [9] for undoped congruent $LiNbO_3$ we evaluate the maximal "birefringence deficiency" $\Delta n = n_e^{2\omega} - n_o^{\omega}$ which can be compensated using photovoltaic nonlinearity to be $\Delta n \approx 0.003$. This corresponds to the optically induced electric space charge field of order of ~250 kV/cm.

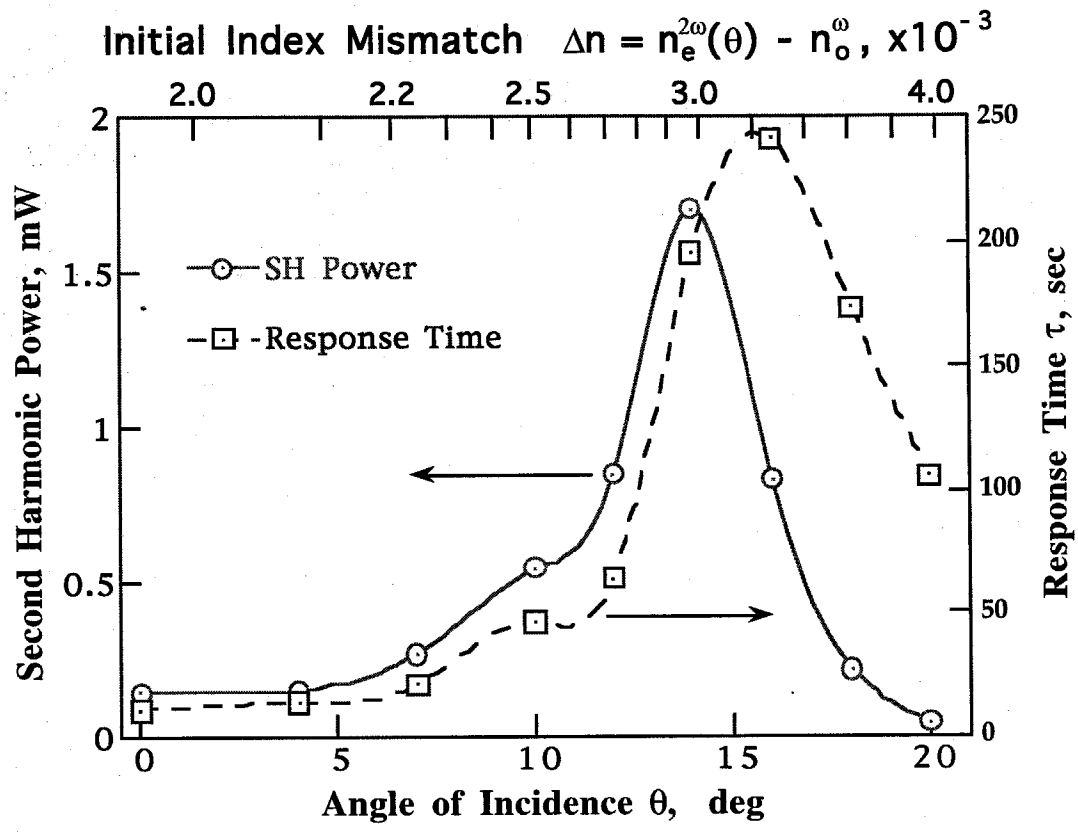

Figure 7.6. Second harmonic power at steady state (after 20 min.) (circles, solid line) and the buildup time τ (squares, dashed line) vs. incidence angle (in air) of the fundamental beam (optical power 1.5 W, lower scale) and the initial $\Delta n = n_e^{2\omega} - n_o^{\omega}$ calculated using Sellmeier equation (upper scale). The SH power obtained with a critically phase-matched MgO-doped $LiNbO_3$ crystal is 4.2 mW in the same experimental arrangements.

The characteristic response time τ of the phase-matching process depends significantly on the initial (t=0) index mismatch, which can be controlled by changing the incidence angle (Figure 7.6). The response time has a maximum in the vicinity of the optimal angle and decreases otherwise, instead of being a monotonically increasing function of the starting mismatch $n_e^{2\omega}(t=0) - n_o^{\omega}$. This behavior resembles the "critical slowing down" phenomenon

described in Chapter 6 of this thesis. Similarly to the photorefractive nonlinear oscillators, the self-phase-matched SHG may also be viewed as a system with (positive or negative) feedback with the threshold parameter being the difference between the induced index perturbation and the one required to achieve the ideally phase matched SHG.

The self-phase-matching effect has been found in a large variety of oxidized Fe-doped $LiNbO_3$ samples. The temporal evolution of the spatial structure of the emerging second harmonic in a 5 mm long Fe-doped (0.05%wt) crystal is shown in Figure 7.7. Although the total power of the second harmonic increases dramatically, as the internal space charge field builds up, strong self-phase modulation due to the spatial dependence of the index of refraction leads to substantial beam distortion, and for sufficiently large interaction length can lead to a complete breakup of the second harmonic beam, in which case the far-field pattern of the generated second harmonic beam eventually evolves into a picture of random speckles (Figure 7.7(c)), where no large scale structures can be resolved [5, 6].

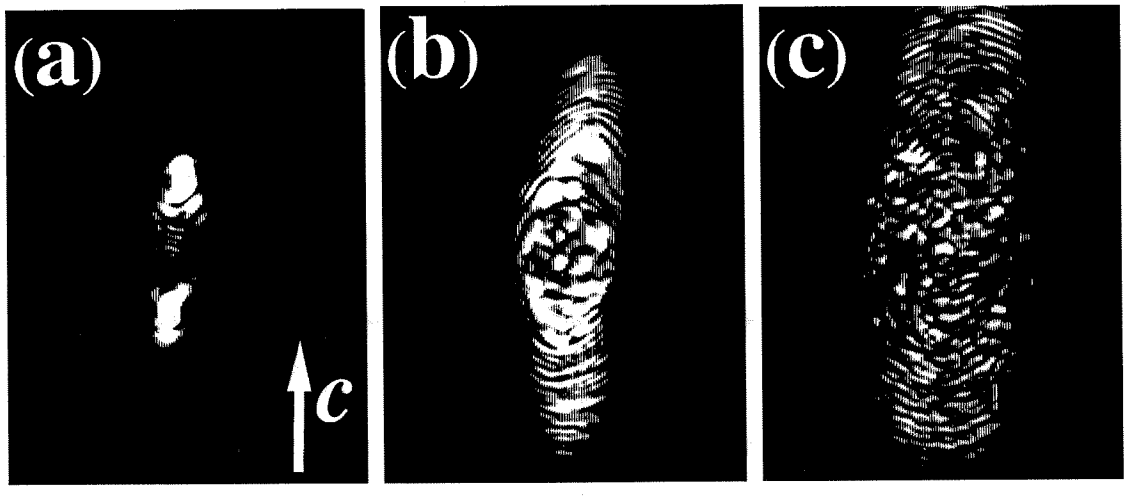

Figure 7.7. Far-field of the generated SH beam in a 5 mm long crystal (a) intermediate stage (t= 20 sec after the beginning of exposure), (b) pattern with multiple orders of diffraction (t = 100 sec) (c) after the speckled structure has developed (t= 400 sec; total far-field angle of the beam in the *c*-axis plane is ~40°).

7.4 Two-dimensional modeling of the photorefractive/photovoltaic effect

The asymmetry in the far-field pattern of the generated second harmonic beam (Figure 7.4(b,c)) is due to the anisotropy of the spatial profile of the index perturbation Δn_e. In lithium niobate the photorefractive nonlinearity arises mainly due to the photovoltaic effect, which is highly anisotropic: the photovoltaic currents (and resulting electric field) are directed along the *c*-axis. The index profile can be calculated by solving numerically the *nonlinear* Kukhtarev's equations [17] (i.e. rate and continuity equation including photovoltaic current, and Gauss law) in two transverse dimensions [18] without invoking the standard linearization procedure (since the light intensity of the beams is localized and the condition $I(\mathbf{r})-I_0 << I_0$ does not hold). The nonlinear band transport equations are

$$\frac{\partial N_D^+(\mathbf{r})}{\partial t} = \alpha(I(\mathbf{r}) + I_d)\left(N_D - N_D^+\right) - \gamma_e n_e N_D^+ , \qquad 7.8$$

$$\frac{\partial n_e(\mathbf{r})}{\partial t} = \frac{\partial N_D^+(\mathbf{r})}{\partial t} + \frac{1}{e}\nabla \mathbf{j}_e , \qquad 7.9$$

$$\mathbf{j}_e = \kappa\,\alpha\, I(\mathbf{r})\left(N_D - N_D^+\right) + \frac{\mu k_b T}{e}\cdot\nabla n_e + e\mu_e n_e(-\nabla\varphi) , \qquad 7.10$$

$$\nabla^2\varphi = -\frac{e}{\varepsilon}\left(N_D^+ - N_a\right), \qquad 7.11$$

where I_d is the effective dark irradiance, κ is the photovoltaic tensor (here we neglect small nondiagonal elements of κ, and take $\kappa = (\kappa,0,0)$, i.e., the *c*-axis is along the x-direction) and φ is the electrostatic potential ($\mathbf{E} = -\nabla\varphi$). The solution of equation 7.8-7.11 can be significantly simplified, if we neglect the trap saturation [18], i.e., assume that $N_D^+(\mathbf{r}) = N_a$. This approximation is valid if the diameter of the beam is much larger than the Debye screening length (see Chapter 4 of this thesis) due to ionized donors, which is typically of the order of 0.1 to 0.5 μm in Fe-doped lithium niobate. In the conditions of the

experiments described here, this is the case. Then the density of free conduction band electrons $n_e(\mathbf{r})$ is

$$n_e(\mathbf{r}) = \frac{\alpha(I(\mathbf{r}) + I_d)(N_D - N_a)}{\gamma_e N_a}, \qquad 7.12$$

and the steady-state value (i.e., when $\partial n_e(\mathbf{r})/\partial t = 0$) of the electrostatic potential $\varphi(x,y)$ can be found by solving a single partial differential equation for the divergence of the steady-state current within the x-y plane:

$$\nabla \mathbf{j}_e(x, y) = 0 . \qquad 7.13$$

Note the difference between the two-dimensional case 7.13 and the one-dimensional formulation: $\partial j_e(x)/\partial x = 0$; solutions $j_e(x) = \text{const}$, $E_x(x) = E_{p.v.} I(x)/(I(x)+I_d)$ [19]. Equation 7.13 can be expressed in terms of the unknown electrostatic potential only:

$$E_{p.v.} \frac{\partial I}{\partial x} + \frac{k_b T}{e}\left(\frac{\partial^2 I}{\partial x^2} + \frac{\partial^2 I}{\partial y^2} \right) - \left(\frac{\partial I}{\partial x}\frac{\partial \varphi}{\partial x} + \frac{\partial I}{\partial y}\frac{\partial \varphi}{\partial y} \right) - (I + I_d)\left(\frac{\partial^2 \varphi}{\partial x^2} + \frac{\partial^2 \varphi}{\partial y^2} \right) = 0 , \qquad 7.14$$

where $E_{p.v.} \equiv \kappa \gamma_e N_a / e\mu_e$ is the characteristic photovoltaic field of the crystal. The equation 7.14 is further transformed and expressed in terms of unitless variables $\tilde{x}$, $\tilde{y}$, and $\tilde{\varphi}$:

$$x = \tilde{x} \cdot a , \qquad 7.15$$

$$y = \tilde{y} \cdot a , \qquad 7.16$$

$$\varphi = \tilde{\varphi} \cdot E_{p.v.} \cdot a , \qquad 7.17$$

$$\gamma_d = \frac{k_b T}{e\, E_{p.v.} \cdot a} , \qquad 7.18$$

where γ_d is a small (< 0.05) parameter which describes the diffusion contribution to the index perturbation (compared to photovoltaic field). We now assume that the light intensity distribution has gaussian profile:

$$I(\tilde{x},\tilde{y}) = I_0 \exp\left(-\left(x^2+y^2\right)/a^2\right) = 1\cdot\exp\left(-\left(\tilde{x}^2+\tilde{y}^2\right)\right), \qquad 7.19$$

where a is the diameter of the gaussian beam. The projections of the internal space charge field **E**(x,y) are given by the spatial derivatives of φ, i.e., for the *c* -axis projection E_x:

$$\tilde{E}_x = -\frac{\partial\tilde{\varphi}}{\partial\tilde{x}} = -\frac{\partial\varphi}{\partial x}\cdot\frac{1}{E_{p.v.}}, \qquad \text{or} \quad E_x = \tilde{E}_x\cdot E_{p.v.}\,. \qquad 7.20$$

Finally, the working equation for the (normalized) electrostatic potential $\tilde{\varphi}$ arising due to the photovoltaic and photorefractive effects in two transverse dimensions is

$$\frac{\partial\ln(I+I_d)}{\partial x} + \frac{\gamma_d}{I+I_d}\left(\frac{\partial^2 I}{\partial\tilde{x}^2}+\frac{\partial^2 I}{\partial\tilde{y}^2}\right) - \left(\frac{\partial\ln(I+I_d)}{\partial\tilde{x}}\frac{\partial\tilde{\varphi}}{\partial\tilde{x}} + \frac{\partial\ln(I+I_d)}{\partial\tilde{y}}\frac{\partial\tilde{\varphi}}{\partial\tilde{y}}\right) - \left(\frac{\partial^2\tilde{\varphi}}{\partial\tilde{x}^2}+\frac{\partial^2\tilde{\varphi}}{\partial\tilde{y}^2}\right) = 0\,, \qquad 7.21$$

which is supplemented by the proper boundary conditions for the electrostatic potential on the boundaries of the computation region. Externally applied electric field would correspond to the proportionate difference between the values of φ on the opposite boundaries. For the simplest case of short circuited boundaries, the case used in the current work, we set

$$\tilde{\varphi}(-L/2, y) = \tilde{\varphi}(L/2, y) = \tilde{\varphi}(x, L/2) = \tilde{\varphi}(x, -L/2) \equiv 0\,. \qquad 7.22$$

Equation 7.21 with boundary conditions 7.22 was solved numerically using the relaxation technique. The perturbation in the extraordinary index of refraction which is proportional to the c-axis projection of the internal space charge field (i.e., $E_x = -\partial\varphi/\partial x$ and $\Delta n_e(x,y) = E_x(x,y) r_{33} n_e^3/2$) is shown in Figure 7.8. The $\Delta n_e(x,y)$ is maximal and has nearly flat profile in the center of the beam, has two sidelobes on its margins, and falls off to zero value where the light intensity is less than the effective dark irradiance $I(r) \ll I_d$. At the same time, the gradients of Δn_e are the largest along the direction of the *c*-axis of the crystal. This

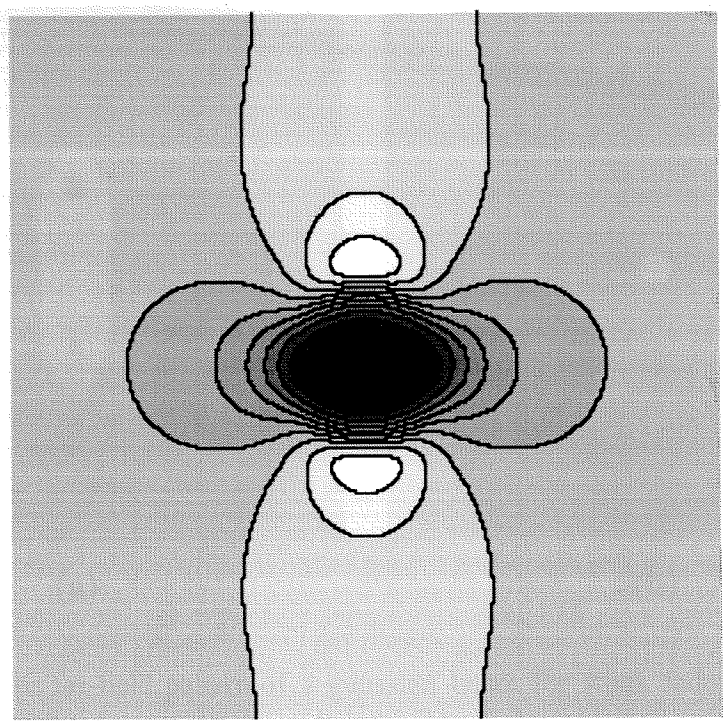

Figure 7.8. Extraordinary index perturbation Δn_e induced by a gaussian beam (dark regions correspond to negative index change). Beam diameter a is 1/6 of the size of computation region, I_d = 0.05 I(0,0), characteristic diffusion field k_bT/ea = $0.01E_{p.v.}$, $\gamma_d = 0.01$, trap saturation is neglected. The *c*-axis direction is vertical.

results in preferential scattering of the SH beam in the *c*-axis plane and large asymmetry of its far-field pattern.

The far-field pattern can also be calculated from the index distribution if we neglect the diffraction *within* the crystal. Then, due to the self-induced photorefractive index perturbation (such as the one shown in Figure 7.8) the complex amplitude of the gaussian beam attains the inhomogeneous phase change as given by

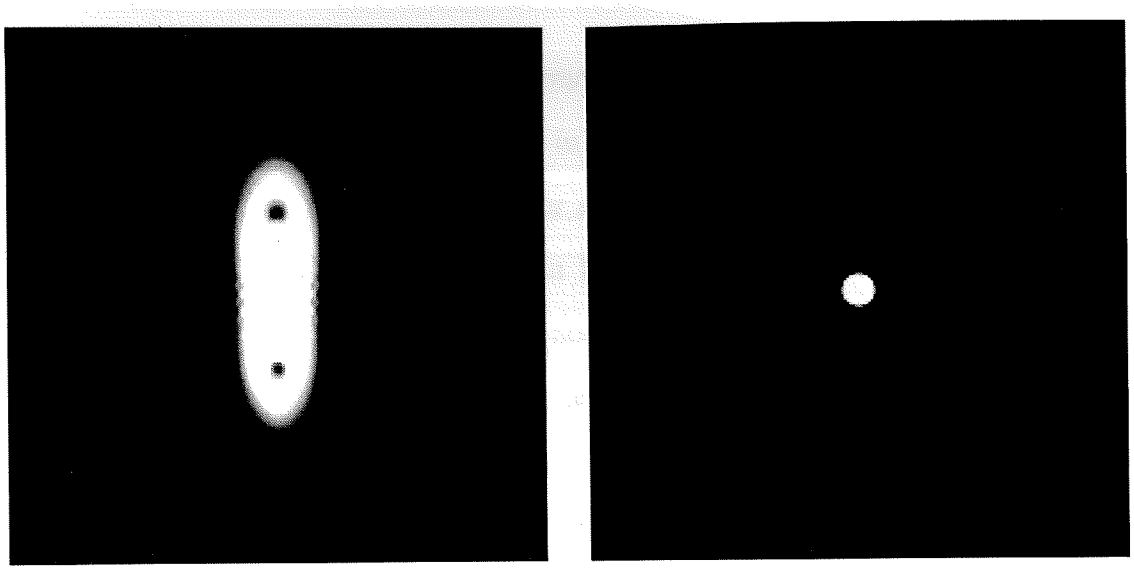

(a) (b)

Figure 7.9. (a) The far-field pattern of a gaussian beam for weak index perturbation $|\Delta n_e(\max)|\, L/\lambda \approx 3$. Diffraction within the crystal is neglected. Note a slight asymmetry in +/-*c* direction due to the diffusion field. (b) The far-field of unperturbed beam (same scale).

$$A(\tilde{x}, \tilde{y}, +0) = A(\tilde{x}, \tilde{y}, -0)\cdot\exp\left(i2\pi \frac{\Delta n_e(\tilde{x}, \tilde{y})\, L}{\lambda}\right), \qquad 7.23$$

where $A(\tilde{x}, \tilde{y}, -0)$ is the field amplitude just before the crystal and $A(\tilde{x}, \tilde{y}, +0)$ is the field amplitude right after the crystal. The intensity distribution in the far-field is then given by the magnitude squared of the appropriate Fourier transform of equation 7.23, given the amplitude distribution of the input beam. Figure 7.9 shows that even in the case of a round gaussian input beam its far-field is strongly and asymmetrically distorted along the *c*-axis direction. This is in good qualitative agreement with the experimental results described in Section 7.3.

7.5 Summary

Phase matching of the optical second harmonic generation can be achieved using natural birefringence, quasi-phase matching, or, in some special cases, the nonlinear index perturbation. We demonstrated the nonlinear self-phase matching of optical SHG due to strong photorefractive/photovoltaic effect in lithium niobate. In the presence of strong photovoltaic effect in $LiNbO_3$ the SHG nonlinear interaction manifests itself in two characteristic and very apparent manners: a large change in the conversion efficiency and strong self-phase modulation (defocusing) of the generated second harmonic. The spatial profile of the index of refraction perturbation arising from the photovoltaic effect is very asymmetric, leading to preferential scattering of the diffracted light in the plane of the optical *c*-axis. There is a good qualitative agreement between the experiments and the basic predictions of the two-dimensional theoretical model of the photorefractive effect.

References for Chapter Seven

[1] J. A. Giordmaine, Phys. Rev. Lett. **8**, 19 (1962).

[2] J. A. Armstrong, N. Bloembergen, J. Ducuing, and P. S. Pershan, Phys. Rev. **127**, 1918 (1962).

[3] S. Somekh and A. Yariv, Opt. Commun. **6**, 301 (1972).

[4] M. M. Fejer, G. A. Magel, D. H. Jundt, and R. L. Byer, IEEE J. Quantum Electron. **QE-28**, 2631 (1992).

[5] A. Ashkin, G. D. Boyd, J. M. Dziedzic, R. G. Smith, A. A. Ballman, J. J. Levinstein, and K. Nassau, Appl. Phys. Lett. **9**, 72 (1966).

[6] F. S. Chen, J. Appl. Phys. **40**, 3389 (1969).

[7] S. Orlov, A. Yariv, and M. Segev, in *Conference on Lasers and Electro-Optics'95*, Vol. 15 of 1995 OSA Technical Digest Series (Optical Society of America, Washington, D.C.), p. 243, paper CWK2, Baltimore, MD.

[8] A. Yariv, *Quantum Electronics*, (John Willey & Sons, New York, 1988), Chapter 16.

[9] D. S. Smith, H. D. Riccius, and R. P. Edmin, Opt. Commun. **17**, 332 (1976).

[10] U. Österberg and W. Margulis, Opt. Lett. **11**, 516 (1986).

[11] E. M. Dianov, P. G. Kazansky, and D. Yu. Stepanov, Sov. J. Quantum Electron. **19**, 575 (1989).

[12] S. D. Durbin, S. M. Arakelian, and Y. R. Shen, Opt. Lett. **9**, 411 (1981).

[13] M. Horowitz, R. Daisy, O. Werner, and B. Fischer, Opt. Lett. **17**, 475 (1992).

[14] I. F. Kanaev, V. K. Malinovsky, and A. M. Pugachev, Ferroelectrics **75**, 209 (1987).

[15] F. Jermann and J. Otten, J. Opt. Soc. Am. B **10**, 2085 (1993).

[16] P. K. Tien, R. Ulrich, and R. Martin, Appl. Phys. Lett. **17**, 447 (1970).

[17] N. V. Kukhtarev, V. B. Markov, S. G. Odoulov, M. S. Soskin, and V. L. Vinetskii, Ferroelectrics **22**, 949 (1979).

[18] A. A. Zozulya and D. Z. Anderson, Phys. Rev. A **51**, 1520 (1995).

[19] G. C. Valley, M. Segev, B. Crosignani, A. Yariv, M. M. Fejer, and M. C. Bashaw, Phys. Rev. A **50**, R4457 (1994).

Chapter Eight

Relevant Publications

Holographic Storage Dynamics in Lithium Niobate: Theory and Experiment, A. Yariv, S. S. Orlov, and G. A. Rakuljic, to be published in J. Opt. Soc. Am. B (November 1996).

Nonlinear Self-Phase-Matching of Optical Second Harmonic Generation in Lithium Niobate, S. Orlov, A. Yariv, and M. Segev, Appl. Phys. Lett. **68**, 1610 (1996).

Holographic Fixing, Readout, and Storage Dynamics in Photorefractive Materials, A. Yariv, S. Orlov, G. Rakuljic, and V. Leyva, Opt. Lett. **20**, 1334 (1995).

Order-Disorder Phase-Transition and Critical Slowing Down in Photorefractive Self-Oscillators, D. Engin, S. Orlov, M. Segev, G. C. Valley, and A. Yariv, Phys. Rev. Lett. **74**, 1743 (1995).

Double Phase Conjugation, D. Engin, M. Segev, S. Orlov, A. Yariv, and G. C. Valley, J. Opt. Soc. Am. B **11**, 1708 (1994).

Conjugation Fidelity and Reflectivity in Photorefractive Double Phase Conjugate Mirrors, S. Orlov, M. Segev, A. Yariv, and G. C. Valley, Opt. Lett. **19**, 578 (1994).

Light-induced Absorption in Photorefractive Strontium Barium Niobate, S. Orlov, M. Segev, A. Yariv, and R. R. Neurgaonkar, Opt. Lett. **19**, 1293 (1994).

Spatial and Temporal Characteristics of Electrically Fixed Holograms in Photorefractive Strontium Barium Niobate, S. Orlov, D. Psaltis, and R. R. Neurgaonkar, Appl. Phys. Lett. **64**, 824 (1994).

Dynamic Electronic Compensation of Fixed Gratings in Photorefractive Media, S. Orlov, D. Psaltis, and R. R. Neurgaonkar, Appl. Phys. Lett. **63**, 2466 (1993).

Electrical Fixing of Photorefractive Holograms in $Sr_{0.75}Ba_{0.25}Nb_2O_6$, Y. Qiao, S. Orlov, D. Psaltis, and R. R. Neurgaonkar, Opt. Lett. **18**, 1004 (1993).

Double Phase Conjugate Mirror - Experimental Investigation and Comparison with Theory, N. V. Bogodaev, V. V. Eliseev, L. I. Ivleva, A. S. Korshunov, S. S. Orlov, N. M. Polozkov, and A. A. Zozulya, J. Opt. Soc. Am. B **9**, 1493 (1992).